Synthesis and Physical Properties of Low Dimensional Quantum Magnets

Gøran Jan Nilsen

Supervisors:

Professor Henrik M. Rønnow (EPFL)

Professor Andrew Harrison (University of Edinburgh)

Doctor of Philosophy

School of Chemistry

University of Edinburgh

2010

Abstract

Strong electron correlation lies at the root of many quantum collective phenomena observed in solids, including high T_c superconductivity. Theoretically, the problem of many interacting electrons is difficult to treat, however, and a microscopic understanding of strongly correlated systems remains one of the foremost challenges in modern physics. A particularly clean realisation of this general problem is found in magnetic systems, where theory and experiment are both well developed and complementary. The role of the chemist in this endeavour is to provide model experimental systems to both inspire new developments in theory and to confirm existing predictions. This thesis aims to demonstrate aspects of both synthesis and physical characterisation of such model systems, with particular emphasis on materials which exhibit unusual quantum ground states due to a combination of reduced dimensionality, low spin, and geometric frustration. Four materials are considered: The first among these is a new material, $KTi(SO_4)_2 \cdot (H_2O)$, which was prepared using a hydrothermal route, and characterised by magnetic susceptibility, specific heat, and high field magnetisation measurements. Fitting exact diagonalisation and series expansion results to these data imply that $KTi(SO_4)_2 \cdot (H_2O)$ is a long-sought experimental realization of the $S = 1/2$ Heisenberg frustrated $(J_1 - J_2)$ chain model in the dimerised regime of the phase diagram. The anhydrous analogue of $KTi(SO_4)_2 \cdot (H_2O)$, $KTi(SO_4)_2$, was also investigated, and found by magnetic neutron scattering to exemplify the $S = 1/2$ Heisenberg anisotropic triangular lattice model in the $1D$ chain limit. The final two materials discussed are the naturally occurring minerals volborthite and herbertsmithite, both thought to realise the $S = 1/2$ Heisenberg kagome antiferromagnet model. Diffuse and inelastic magnetic neutron scattering experiments, however, indicate that the kagome physics are partially destroyed by defects in the former and lattice distortion in the latter.

Acknowledgements

As I begin this section at the end of a long and arduous writing process, it occurs to me that this will probably end up one of the most difficult parts to set down on (electronic) paper. I have a long, long list of people to thank, and doing them all justice with a few words is close to impossible. Nonetheless, I will do my best, and hope that everyone receives at least close to their fair dues.

A natural place to start is with my supervisors, Henrik Rønnow and Andrew Harrison. Henrik has been a constant source of inspiration and enthusiasm throughout the last three and a half years, providing a free, but still supportive environment to do my research in. He has demonstrated to me by his own example all the qualities which make a good scientist, and it is thanks to him that I can (tentatively) call myself one today. Andrew was the one who started me on the path which has culminated in the document you now hold in your (digital) hands, and his contribution during my BSc project, and much of my first year was crucial for the eventual success of the work detailed in the coming chapters. This thesis obviously would not exist if it were not for these two people.

I would also like to thank the many collaborators who at various stages of my thesis helped me with experiments, answered my sometimes naive questions, and provided me with much food for thought through inspiring discussions. Undoubtedly, the two I spent the most time at neutron scattering experiments with were Martin F. Mourigal and Niels B. Christensen, who not only taught me much about physics, but also filled the time between scans with much hilarity. Ross Stewart and Pascale Deen were more than just local contacts, and made a significant contribution to the work presented in Chapter 5. Ross' home recorded Sisters of Mercy covers were also much appreciated. Clemens Ritter kindly provided some of his internal beamtime on the D1B diffractometer to measure the yavapaiite samples discussed towards the end of Chapter 4, as well as helping with the Rietveld refinement of this data. Apropos yavapaiite samples, Archana Raja was a great help in producing the 10 or so grams needed for inelastic neutron scattering. On the theoretical side, I've benefitted from a now long-standing collaboration with Deepa Kasinathan, Oleg Janson, and Helge Rosner at the Institute for the Chemical Physics of Solids Dresden. Their *ab-initio* calculations have shed light on a number of difficult questions, particularly relating to $KTi(SO_4)_2 \cdot (H_2O)$, and their recent help (along with Alexander Tsirlin) in doing the high field magnetisation measurements on the same compound added a valuable piece of information to the puzzle.

The last few years wouldn't have been what they were without my group-mates, who

were not only a great help in the lab, but also delightful company during many coffee breaks shared together. Mark de Vries kindly invited me along to several experiments during my Bachelors project, and was also central to the work shown in the latter half of Chapter 5. Fiona Coomer got me started on the $KTi(SO_4)_2 \cdot (H_2O)$ project, as well as generously handing over volborthite when finishing her PhD. I hope I've been a worthy successor. Gaetan Giriat was the perfect officemate, and handy to have around when something went kaput in the lab. On the Swiss side, I would like to thank Julian Piatek, who's unique brand of humour I will miss. Bastien Dalla Piazza, for putting up with me for two semesters during TP4, and for being a well of theoretical knowledge. Neda Nikseresht, for smiles and kindness. Mohamed Zayed, for being inscrutable. Finally, Julio "Mr." Larrea, for coffee, carapulca, and (of course) company.

I've had the fortune of making more friends during my PhD years than I could have ever hoped for, and many, many more than can be listed in an acknowledgement of reasonable length (it's probably getting too long already). I extend my thanks to all of these good people (you know who you are), who have enriched my life enormously. Nevertheless, I can't resist to acknowledge a few in particular (though in no particular order): Balázs "Sipi" Sipos, for times spent together enjoying the finer things in life. Zlatko "Mic" Micković for the jokes, the pearls of Balkan wisdom, and of course for being a great friend. Tamás Tóth, for the surreal humour and the endless (in a good way) conversations – it has been a pleasure, Sir. Judit and Ági Romhányi, for providing me with a home away from home, and for understanding me better than most. Sascha "Ninja" Njaa and Eivind Lichtenberg, for all the good times – pretty sure we'll still be playing silly games on New Years eve 20 years from now. Finally, thanks to Jackie Birnie, who encouraged me to pursue this work from the outset, and who thinks much more highly of me than I deserve.

I feel I've seen far too little of my brothers, Bengt and Derek, in the last few years, but the times we have spent together have been precious. Though I'm going away to Japan for two years, I'll be looking forward to returning home to see them whenever I can. Last but not in any way, shape, or form least, I would like to thank my parents, Klazien and Dennis, to whom this thesis is dedicated. They encouraged me through the hard times, and shared my joy when things were looking up. I particularly appreciated the inspiring conversations on the phone, the packages waiting in the mailbox at the end of a long days work, and the hiking trips in the Alps. Tusen takk for alt!

Thanks also to the reader for their bravery in the face of what is to come.

Declaration

I declare that this thesis was composed by myself, that the work contained herein is my own except where explicitly stated otherwise in the text. This work has not been submitted for any other degree or professional qualification except as specified.

(*Gøran Jan Nilsen*)

Til mine foreldre.

Table of Contents

List of Abbreviations

AKAF	Anisotropic kagome antiferromagnet
AFM	Antiferromagnet(ic)
ATHA	Anisotropic triangular Heisenberg antiferromagnet
CKHAF	Classical kagome Heisenberg antiferromagnet
CAF	Collinear antiferromagnet
CMC	Classical Monte Carlo
CS	Chirality stripe
DM	Dzyaloshinskii-Moriya
DMRG	Density matrix renormalisation group
ED	Exact diagonalisation
ESR	Electron spin resonance
FCM	Frustrated chain model
FM	Ferromagnet(ic)
FWHM	Full width half maximum
HTSE	High temperature series expansion
ILL	Institut Lauge Langevin
LDA	Local density approximation
LSDA+U	Local spin density approximation with Hubbard U
LSWT	Linear spin wave theory
MG	Majumdar-Ghosh
NMR	Nuclear magnetic resonance
QDJS	Quasi-degenerate joint states
QHSA	Quantum ($S = 1/2$) Heisenberg square lattice antiferromagnet model
QHC	Quantum Heisenberg chain
QKHAF	Quantum kagome Heisenberg antiferromagnet
RVB	Resonating valence bond
SQUID	Superconducting quantum interference device
UUD	up-up-down state
VBC	Valence bond crystal
VBG	Valence bond glass
VBC	Valence bond solid
WZNW	Wess-Zumino-Novikov-Witten
XRD	X-ray diffraction
μSR	muon spin rotation

Chapter 1

Introduction

"But I think the Loadstone, is a mixture of stone and Iron, as an Iron stone, or a stone of Iron. Yet do not think the stone is so changed into Iron, as to lose its own nature, nor that the Iron is so drowned in the stone, but it preserves itself, and while one labors to get the victory of the other, the attraction is made by the combat between them. In that body, there is more of the stone, than of Iron, and therefore the Iron, that it may not be subdued by the stone, desires the force and company of Iron, that being not able to resist alone, it may be able by more help to defend itself. For all creatures defend their being."

The quote above, from the 7th volume of John Baptista Porta's "Natural Magick" [Porta (1658 edition)], illustrates just how much ground the field of magnetism has covered since the end of the 16th century. While the concept of inanimate matter having a "soul" is rather poetic, these days it has been replaced by the laws of quantum mechanics, which are able to efficiently explain the origin of a macroscopic magnetic moment in bulk material. Likewise, the "attraction" between two bulk magnets, rather than arising from an epic-sounding "war" between stone and iron, can be fully described by classical electromagnetism. Despite these considerable advances in theory, we do not have all the answers yet, something the huge current interest on the topic of magnetism [1], testifies to. In fact, the material which started it all, lodestone, or magnetite, as it is more commonly known in scientific literature, is ironically still not fully understood, and remains the subject of much work to this day.

While the mathematical framework to treat systems of interacting quantum mechanical particles has existed for a number of decades, the problem quickly becomes computationally intractable when more than a few such particles are involved. In fact, the largest object which can be calculated analytically remains the Hydrogen atom, which

---

[1](conservatively estimated at an impressive $50,000$ publications in the last year alone)
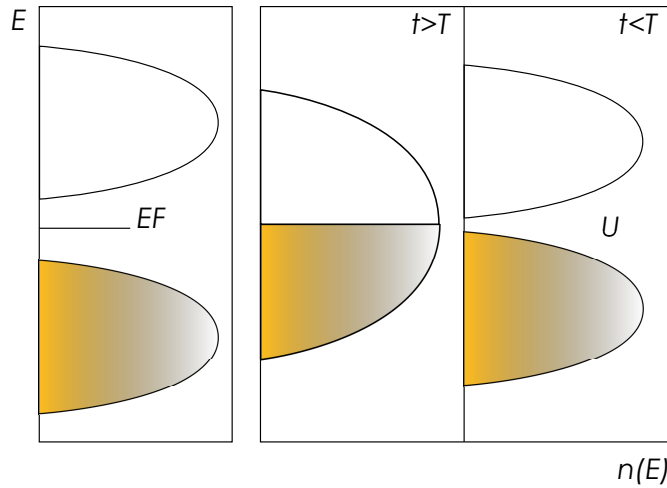
Figure 1.1: Schematic illustration of the density of states of respectively a.) a band insulator b.) a metal $(t > U)$ and c.) a Mott insulator $(t < U)$.

was first solved as long ago as 1914 [Bohr (1913)]. The main issue which renders treatment of larger systems currently impossible is the issue of electon correlation. If we wish to calculate the physical properties of bulk materials containing at the order of N_A particles, considerable simplifications, and particularly a solution to the problem of correlation, are therefore necessary. For example, to understand the electronic properties of a crystalline solid, it is a common first approximation to consider the motion of electrons as a hopping process between lattice sites, and interelectronic correlations are crudely assumed to be dominated by a simple potential which disfavours double occupation of an orbital. The result is the deceptively simple Hubbard Hamiltonian [2] [Hubbard (1963)]:

$$\mathcal{H} = t \sum_{\langle i,j \rangle} \sum_{\sigma = \uparrow, \downarrow} \left(\mathbf{c}_{i\sigma}^{\dagger} \mathbf{c}_{i\sigma} + H.c. \right) + U \sum_i \hat{\mathbf{n}}_{i\uparrow} \hat{\mathbf{n}}_{i\downarrow} \qquad (1.1)$$

where the first term represents hopping as creation and annihilation of uncharged particles with spin σ between a pair of sites i, j with an amplitude, t, proportional to the electron kinetic energy. The second term describes the on-site Coulomb repulsion of strength U. The most trivial solution to this problem is found if there are an even number of sites, n, per unit cell, with a single electron per site. In this case, diagonalisation yields $n/2$ filled and $n/2$ unfilled bands (figure 1.1). This is referred to as a band insulator. If n is odd, however, a rich phase diagram of possible states opens up, ranging from metallic behaviour to magnetic and charge order, and perhaps even superconductivity [Anderson (2002)] (figure 1.2).

---

[2]Named after Hubbard, but originally introduced by Gutzwiller [Gutzwiller (1963)].
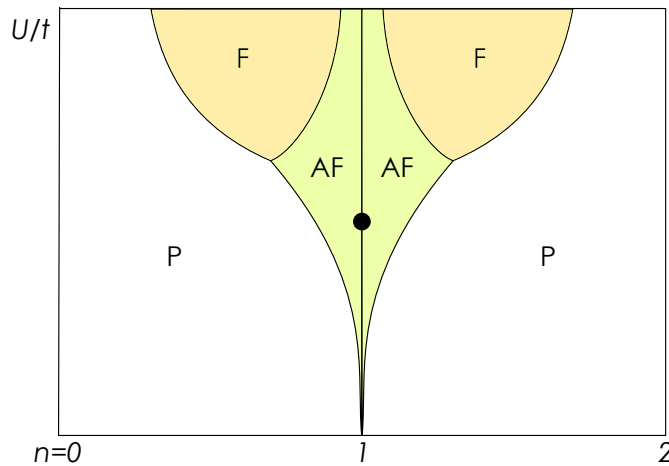
Figure 1.2: Mean field phase diagram of the infinite dimensional Hubbard model. Half filling is indicated by a vertical line, and the Mott transition at $t \sim U$ is represented by a black dot. Adapted from Fazekas [Fazekas (1999)].

The compounds we shall be concerned with for the duration of this thesis all fall into the class of materials referred to as Mott insulators [Mott (1990)]. These arise when the Hubbard model is in the vicinity of half filling, and when $U > t$ (see figure 1.2). In a Mott insulator, the charges become localised due to the on-site repulsion U, resulting in an electron "solid", where each site houses a single unpaired electron. In the insulating ground state, there remains an additional twofold degeneracy at each site related to the spin degree of freedom. By invoking processes involving a concerted hopping, or exchange, of electrons between sites[3], this degeneracy is lifted. Then, projecting onto the subspace of spin configurations, the following effective Hamiltonian is arrived at [Anderson (1959)]:

$$\mathcal{H} = -J \sum_{\langle i,j \rangle} \mathbf{S}_i \mathbf{S}_j \qquad (1.2)$$

where $J = 4t^2/U$ is the exchange integral (typically ranging in magnitude from $J/k_B = 1$ K to 1000+ K), and $\mathbf{S}$ are the spin operators at sites i and j, respectively. Depending on the spatial arrangment of orbitals connecting sites i and j, J can be either positive or negative, resulting in either coparallel (ferromagnetic) or antiparallel (antiferromagnetic) aligments of spins being favoured. The above Hamiltonian is widely known as the Heisenberg model , and will provide the foundation for much of the physics discussed in the remainder of this thesis.

Considering the number of simplifications, approximations, and assumptions made thus

---

[3]Single electron hopping processes result in double occupancy.

far, one would think that the Heisenberg model should be rather easily solvable. As it turns out, it is anything but. Assuming a single electron per site with $S = 1/2$, the size of the Hamiltonian matrix of the pure spin system scales with system size as $2^N \times 2^N$. Even using the symmetries of the problem to block diagonalise $\mathcal{H}$, it is thus only possible to reach $N = 40$ [4], with modern supercomputers. If Monte Carlo techniques are used, N may be increased to a few hundred sites, but this is only possible when circumstances are favourable. While many experimental observables can be accurately reproduced down to low temperatures at these system sizes, information on the ground state for the infinite lattice is limited.

In order to gain a more complete understanding of the ground state, an analytically solvable effective model is thus necessary. For the $S > 1$ Heisenberg model on most simple lattices, for example, simple classical mean field theory [Weiss (1906)] or semi-classical spin wave theory [Kubo (1952)] generally suffice to describe both the ground state and dynamics. In some circumstances, however, particularly when $S \leq 1$, the connectivity of the lattice small, the dimensionality low, and the topology frustrated [5], they do not, and the full quantum mechanical problem must be dealt with. Inconveniently, Monte Carlo techniques also generally break down in this limit [Foulkes *et al.* (2001)], leaving only exact diagonalisation as the generally applicable numerical method.

Solving the problem of the ground state in a frustrated, low dimensional quantum magnet is often a difficult enterprise, requiring a close interplay between cutting edge theory and advanced experiments. For the latter, access to materials which accurately capture the properties of theoretically interesting Hamiltonians is essential. This finally brings us to the issues which lie at the heart of this work: firstly, how do we realise new quantum magnets with unusual properties and, secondly, how can their physical properties be probed? Our attempt to answer these difficult questions will take us from chemical "design" of materials, to measurements using one of the leading techniques in solid state physics, neutron scattering.

The structure of this thesis will be as follows: Chapter 2 will describe the ingredients needed to promote quantum ground states, and some of their basic properties. Chapter 3 will then outline the chemical principles involved in designing a model magnet, before briefly discussing the primary experimental techniques used: polarised neutron scattering and inelastic time of flight neutron scattering. Chapters 4 and 5 constitute the

---

[4]Corresponding to $1,099,511,627,776$ basis states!

[5]This term will be explained in Chapter 2. Frustration can be induced by geometry, when the lattice is constructed of polygons with an odd number of sides, and the interactions are antiferromagnetic, or by competing interactions.

main body of experimental work undertaken during this thesis: Chapter 4 discusses the synthesis and properties of two novel Ti^{3+}-based quantum magnets, $KTi(SO_4)_2 \cdot (H_2O)$, and its anhydrous analogue, $KTi(SO_4)_2$. These respectively realise the $1D$ Heisenberg $J_1 - J_2$ chain model in the dimerised region of the phase diagram and the $1D$ Heisenberg chain model with frustrating interchain interactions, J'. Chapter 5 contains neutron scattering results on the (purportedly) $S = 1/2$ kagome compounds volborthite, $Cu_3V_2O_7(OH)_2 \cdot 2(H_2O)$, and herbertsmithite, $Cu_3Zn(OH)_6Cl_2$, showing that the former probably maps onto an entirely different model, whilst the physics of the latter is dominated by defects. Chapter 6 will attempt to sum up.

Chapter 2

The Ingredients of Quantum Magnetism

Having established a motivation for investigating quantum magnetism in antiferromagnetic Mott insulators in the previous chapter, it is now time to ask ourselves: what are the ingredients required to produce quantum ground states in such systems? Even limiting ourselves to this (relatively speaking) small class of models and materials, there is still an enormous phase space of parameters to explore, which includes: the properties of the individual spins, the type and sign of the couplings, and the connectivity and topology of the lattice, amongst others. Furthermore, most models which can be constructed from these parameters order classically. This chapter will show using some simple theoretical tools how new promising quantum magnets can be identified, and, more generally, what combinations of ingredients lead to interesting ground states. The essential requirements are shown to be small spin length, S, low connectivity, z, low dimensionality, D, and, crucially, frustration (geometric or otherwise). Two hallmarks of a quantum magnet are shown to be the presence of instabilities in the semi-classical spin-wave theory, as well as unusual behaviour in the spectrum of a finite size cluster. Finally, a few examples of what kinds of states result when Néel order breaks down are given.

2.1   Some Basic Results

2.1.1   Quantum and Classical Spins

Before beginning the discussion in earnest, it may be useful (at least it is for the author) to review a few basic properties of the electronic spin:

- The Stern-Gerlach experiment [Gerlach and Stern (1921)] shows that the electron has an intrinsic angular momentum in addition to that generated by its orbital motion. This "spin" angular momentum has a size $S = 1/2$, and its three Cartesian components (x, y, z) may take on values $\pm 1/2$. Furthermore, only one such component of the spin may be measured simultaneously, implying that their respective operators do not commute.

- The spin angular momentum operator is thus defined as a three-component vector $\mathbf{S} = (S_x, S_y, S_z)$, with each component in the case of $S = 1/2$ corresponding to a Pauli matrix of dimension $2S + 1$. In the case of $S = 1/2$, these are:

$$S^x = \frac{\hbar}{2}\sigma^x; \sigma^x = \begin{pmatrix} 0 & 1 \\ 1 & 0 \end{pmatrix} \quad S^y = \frac{\hbar}{2}\sigma^y; \sigma^y = \begin{pmatrix} 0 & -i \\ i & 0 \end{pmatrix} \quad S^z = \frac{\hbar}{2}\sigma^z; \sigma^z = \begin{pmatrix} 1 & 0 \\ 0 & -1 \end{pmatrix}$$

- The eigenstates of these matrixes are typically written as $|\uparrow\rangle_{x,y,z}$ and $|\downarrow\rangle_{x,y,z}$. The eigenstates of the only diagonal matrix among them, S^z, represented as $|\downarrow\rangle_z$ and $|\uparrow\rangle_z$ (or simply $|\downarrow\rangle$ and $|\uparrow\rangle$), are chosen as a convenient basis. The Pauli matrixes form an $SU(2)$ algebra, describing the rotational symmetry of the quantum mechanical spin.

- The operation of either S^x or S^y on an S^z state $|\uparrow\rangle_z$ flips the spin from up to down, and vice versa for $|\downarrow\rangle_z$. Hence, S^x and S^y are often referred to as spin flip operators.

- It is often useful to reformulate the S_x and S_y operators as raising and lowering operators S^+ and S^{-1}, defined as: $S^+ = S^x + iS^y$, $S^- = S^x - iS^y$. Applying these to any state $|m_S\rangle$ yields $S^+ |m_S\rangle = \sqrt{S(S+1) - m_S(m_S+1)}\,|m_S + 1\rangle$ and $S^- |m_S\rangle = \sqrt{S(S+1) - m_S(m_S-1)}\,|m_S - 1\rangle$, respectively.

- As S is increased to ∞, the spin is able to point in any direction, and may hence be represented as a Cartesian vector $S = (\hat{x}, \hat{y}, \hat{z})$. If each component is finally normalised such that $S_x^2 + S_y^2 + S_z^2 = 1$, the resulting object is known as a **classical**

---

[1]Analogously with the quantum harmonic oscillator.

spin. In practical terms, we can get away with this much simpler representation of the spin when $S \geq 3/2$.

- When $S < 3/2$, however, the quantum mechanical nature of the spin is often highly relevant to the physics, as we will see in the coming chapters. At the root of this behaviour lies in the action of the spin flip terms S^x and S^y, or the so-called **quantum fluctuations**. Hence, $S = 1/2$ and $S = 1$ are called **quantum spins**.

2.1.2 The Heisenberg Dimer

The simplest realisation of the Heisenberg model we hand-wavingly derived in the previous chapter is the $S = 1/2$ antiferromagnetic spin pair, described by the following Hamiltonian:

$$\mathcal{H} = J_{12}\mathbf{S}_1 \cdot \mathbf{S}_2 \tag{2.1}$$

where J_{12} is positive, thus favouring antiferromagnetic (antiparallel) alignment of spins. This can be rewritten in matrix representation as:

$$\mathcal{H} = \begin{pmatrix} \langle\uparrow\uparrow|\mathcal{H}|\uparrow\uparrow\rangle & \langle\uparrow\uparrow|\mathcal{H}|\downarrow\uparrow\rangle & \langle\uparrow\uparrow|\mathcal{H}|\uparrow\downarrow\rangle & \langle\uparrow\uparrow|\mathcal{H}|\downarrow\downarrow\rangle \\ \langle\uparrow\downarrow|\mathcal{H}|\uparrow\uparrow\rangle & \langle\uparrow\downarrow|\mathcal{H}|\downarrow\uparrow\rangle & \langle\uparrow\downarrow|\mathcal{H}|\uparrow\downarrow\rangle & \langle\uparrow\downarrow|\mathcal{H}|\downarrow\downarrow\rangle \\ \langle\downarrow\uparrow|\mathcal{H}|\uparrow\uparrow\rangle & \langle\downarrow\uparrow|\mathcal{H}|\downarrow\uparrow\rangle & \langle\downarrow\uparrow|\mathcal{H}|\uparrow\downarrow\rangle & \langle\downarrow\uparrow|\mathcal{H}|\downarrow\downarrow\rangle \\ \langle\downarrow\downarrow|\mathcal{H}|\uparrow\uparrow\rangle & \langle\downarrow\downarrow|\mathcal{H}|\downarrow\uparrow\rangle & \langle\downarrow\downarrow|\mathcal{H}|\uparrow\downarrow\rangle & \langle\downarrow\downarrow|\mathcal{H}|\downarrow\downarrow\rangle \end{pmatrix} = \frac{J}{4}\begin{pmatrix} 1 & 0 & 0 & 0 \\ 0 & -1 & 2 & 0 \\ 0 & 2 & -1 & 0 \\ 0 & 0 & 0 & 1 \end{pmatrix}$$

Diagonalisation yields the following eigenvalues and eigenvectors:

$|\Psi\rangle$	S	E	$\langle S_z \rangle$
$\dfrac{|\uparrow\downarrow\rangle - |\downarrow\uparrow\rangle}{\sqrt{2}}$	0	$-3/4 J_{12}$	0
$|\uparrow\uparrow\rangle$	1	$1/4 J_{12}$	1
$|\downarrow\downarrow\rangle$	1	$1/4 J_{12}$	-1
$\dfrac{|\uparrow\downarrow\rangle + |\downarrow\uparrow\rangle}{\sqrt{2}}$	1	$1/4 J_{12}$	0

The ground state of the $S = 1/2$ Heisenberg dimer is the so-called **singlet** state, an antisymmetric superposition of the $|\uparrow\downarrow\rangle$ and $|\downarrow\uparrow\rangle$ states. This unit is considered one of the basic building blocks of quantum magnetism, and is an archetypal example of

an entangled state [2]. The excited state, separated from the ground state by a gap $\Delta = J_{12}$ is a **triplet** level with $S = 1$. At this point, we note that the classical ground state $|\uparrow\downarrow\rangle_z$ is not even an eigenstate of the Hamiltonian, and furthermore has energy $E_N = -J_{12}/4$, considerably higher than that of the actual ground state.

As S is increased, the basis consists of $(2S+1)^2$ states, resulting in a Hamiltonian matrix of dimension $(2S + 1)^2 \times (2S + 1)^2$. This becomes a considerable task to diagonalise (at least by hand) for $S > 1$. Using the fact that the Hamiltonian commutes with $\mathbf{S}_{tot} = \mathbf{S}_1 + \mathbf{S}_2$, however, it is still easy to find the eigenvalues:

$$\mathcal{H} = J_{12}\mathbf{S}_1 \cdot \mathbf{S}_2 = \frac{J_{12}}{2}[(\mathbf{S}_1 + \mathbf{S}_2)^2 - \mathbf{S}_1^2 - \mathbf{S}_2^2] = J_{12}[\mathbf{S}_{tot}^2 - \mathbf{S}_1^2 - \mathbf{S}_2^2] \qquad (2.2)$$

The ground state of the spin S Heisenberg dimer is thus an $S = 0$ singlet with $E_0 = -JS(S + 1)$. The first of the $2S_{tot} + 1$ excited states occurs at $E_1 = E_0 + J$. The ground state energy of the classical state, on the other hand, scales as $E_N = -JS^2$, meaning that the quantum correction to the classical energy is of the order $E_N/E_0 = -JS^2/[JS(S + 1)] = 1/S$.

2.1.3   Towards Extended Systems

Having established that the ground state of the antiferromagnetic Heisenberg dimer is a singlet (an entirely quantum mechanical object), we now wish to understand the observation that most extended lattice antiferromagnets order classically at relatively high temperatures. To achieve this, the ground state energy in the thermodynamic limit must be calculated and compared to the classical value. It quickly becomes apparent that this is no small matter: the dimension of the Hamiltonian matrix for a system containing N spins of size S grows as $(2S+1)^N \times (2S+1)^N$. Although the commutation of S^z with the total spin S allows for block diagonalisation of $\mathcal{H}$, the largest sector still has dimension:

$$\frac{N!}{n_\uparrow!(N - n_\uparrow)!} \times \frac{N!}{n_\uparrow!(N - n_\uparrow)!} \qquad (2.3)$$

where $n_\uparrow$ is $N/2$ for even N and $N/2 + 1$ for odd N. Even for $S = 1/2$, this matrix quickly becomes too large to diagonalise on all but the most powerful supercomputers – in fact, the current world record for an $S = 1/2$ system is a mere 40 spins! While

---

[2]Entanglement is a property of a quantum mechanical system of two objects or more, whereby the state of one constituent cannot be described without also considering the state of the other [Einstein *et al.* (1935)].
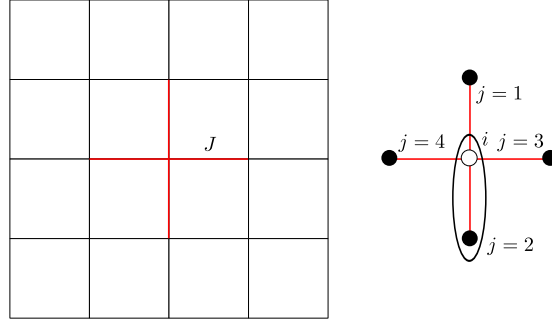
Figure 2.1: Decomposition of the square lattice into independent clusters.

it is obviously impossible to calculate the ground state energy in the thermodynamic limit exactly, its lower bound can be estimated by decomposing the lattice into N independent clusters, then summing up the energy of these clusters. Taking the example of the square lattice, the cluster chosen is a cross of 5 spins. The cluster Hamiltonian is written [Fazekas (1999)]:

$$\mathcal{H} = \sum_{i=1}^{N} \mathcal{H}_i \qquad (2.4)$$

where:

$$\mathcal{H}_i = \frac{J}{2} \mathbf{S}_i \cdot \sum_{j=1}^{z} \mathbf{S}_j = \frac{1}{2} \left[\left(\mathbf{S}_i + \sum_{j}^{z} \mathbf{S}_j \right)^2 - S(S+1) - \left(\sum_{j}^{z} \mathbf{S}_j \right)^2 \right] \qquad (2.5)$$

H_i (2.5) is minimised by making the total spin of the z nearest neighbours as large as possible, due to the last term $(-\sum_{j}^{z} \mathbf{S}_j{}^2)$, and then minimising the first term $(\left(\mathbf{S}_i + \sum_{j}^{z} \mathbf{S}_j \right)^2)$ by creating one singlet (see figure 2.1). The lowest energy level is thus found to be:

$$E_{i,0} = -zS^2 \left(1 + \frac{1}{zS} \right) \qquad (2.6)$$

$\mathcal{H}$ can no longer be minimised locally once the number of clusters is increased beyond one, as the clusters overlap. Nevertheless, a lower bound for the energy can be found by performing the summation in (2.4) assuming N independent clusters:

$$E_0 > -\frac{JNzS}{2} \left(S + \frac{1}{z} \right) \qquad (2.7)$$

This can be compared to the classical ground state energy, $E_N = J \sum_{i,j}^{N} \vec{S}_i \cdot \vec{S}_j$, where i and j are neighbouring spins, and $\vec{S}$ are classical vectors. Assuming each spin is able

to arrange itself such that it is antiparallel with respect to all its nearest neighbours, the resulting energy is:

$$E_N = -\frac{JNzS^2}{2} \tag{2.8}$$

which, as expected, is higher than E_0. The true ground state energy of the extended lattice Heisenberg antiferromagnet thus lies in the range $E_0 < E_{gs} < E_N$. The gap between the upper and lower bounds is proportional to $1/(zS)$, implying that the quantum and classical ground states become identical for large z and S (figure 2.2). Conversely, when z and S are small, the quantum corrections should be large – but are they are large enough to destroy classical order completely?
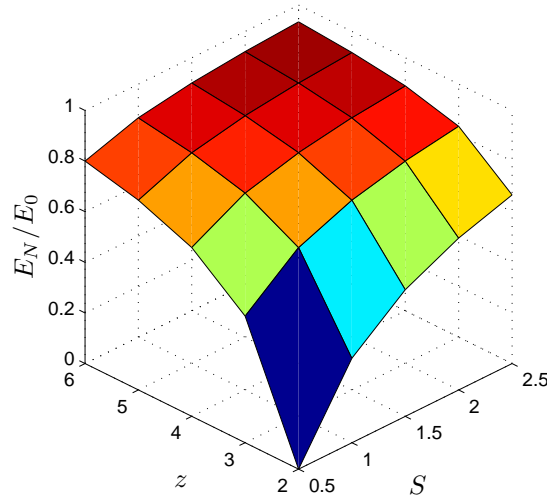
Figure 2.2: Scaling of E_0/E_N with respect to S and z. The colourscale indicates the magnitude of the quantum correction to the classical energy, running from large (blue) to small (red).

2.1.4   Spin Wave Theory

One way to test the stability of the classical ground state is to assume long range order, then introduce quantum fluctuations to the system by some means. A particularly elegant way to implement these is by representing the action of the spin operators as creations and annihilations of bosons through a Holstein-Primakoff transformation [Holstein and Primakoff (1940)],[Kubo (1952)]:

$$
\begin{aligned}
S_i^z &= S - a_i^\dagger a_i \\
S_i^+ &= \sqrt{2S}\sqrt{1 - \frac{a_i^\dagger a_i}{2S}}\, a_i \\
S_i^- &= \sqrt{2S}\, a_i^\dagger \sqrt{1 - \frac{a_i^\dagger a_i}{2S}}
\end{aligned}
\tag{2.9}
$$

where the spin is assumed to lie along the local S^z direction, a_i and $a_i^\dagger$ create and annihilate $S = 1$ bosons, whilst $a_i^\dagger a_i$ counts the total number of bosons. The term inside the square root limits the boson population number to the physical subspace of the $2S + 1$ eigenstates of the spin operators. This term has the side effect of rendering the Hamiltonian impossible to write in diagonal form, however, and is therefore dealt with by expanding the square root as its Taylor series $\sqrt{1 - x} = 1 - x/2 - x^2/8...$ and keeping only the leading constant. This corresponds to assuming $2S >> a_i^\dagger a_i$ (the number of bosons is small versus S), a reasonable assumption to make for classical spins.

One of the simplest examples of linear spin wave theory is found for the $S = 1/2$ square lattice antiferromagnet (QHSA). Due to the small spin and small coordination number ($z = 4$), strong quantum effects resulting from the spin flip terms, and perhaps even a breakdown of long range order are expected. The classical ground state of the QHSA is a simple arrangement whereby each spin lies antiparallel with respect to its nearest neighbour. As such, it is natural to break the lattice into two sublattices, A and B, where the spins on each sublattice point in the same direction. Another useful trick is then to rewrite the Hamiltonian as a sum over nearest neighbours:

$$
\mathcal{H} = \sum_i \sum_\delta \mathbf{S}_i \cdot \mathbf{S}_i + \delta
\tag{2.10}
$$

where δ are a set of vectors coupling the A and B sublattices – in the case of the square lattice $\delta = \{\hat{e}_x, -\hat{e}_x, \hat{e}_y, -\hat{e}_y\}$. Thus, the operators residing on the A and B sublattices may be Fourier transformed as follows:

$$
\begin{aligned}
a_i &= \sqrt{\frac{2}{L}} \sum_{\mathbf{k}\in BZ} e^{i\mathbf{k}\vec{R}_i} a_\mathbf{k} & a_i^\dagger &= \sqrt{\frac{2}{L}} \sum_{\mathbf{k}\in BZ} e^{i\mathbf{k}\vec{R}_i} a_\mathbf{k} \\
b_j &= \sqrt{\frac{2}{L}} \sum_{\mathbf{k}\in BZ} e^{i\mathbf{k}\vec{R}_i} b_\mathbf{k} & b_j^\dagger &= \sqrt{\frac{2}{L}} \sum_{\mathbf{k}\in BZ} e^{i\mathbf{k}\vec{R}_j} b_\mathbf{k}
\end{aligned}
\tag{2.11}
$$

where L is the occurence of a given boson in the unit cell, and $\mathbf{k}$ is a wavevector in the reduced Brillouin zone of the square lattice. The spin wave Hamiltonian which results is:

$$\mathcal{H}_{SW} = -\frac{zNJS^2}{2} + zJS\sum_{\mathbf{k}}\left[a_{\mathbf{k}}^{\dagger}a_{\mathbf{k}} + b_{\mathbf{k}}^{\dagger}b_{\mathbf{k}} + \gamma_{\mathbf{k}}\left(a_{\mathbf{k}}^{\dagger}b_{\mathbf{k}}^{\dagger} + a_{\mathbf{k}}b_{\mathbf{k}}\right)\right] \tag{2.12}$$

where the first term is recognizable as the classical ground state energy and the second represents the lowering of ground state energy due to quantum fluctuations. The $\gamma = \sum_{\delta} e^{i\mathbf{k}\cdot\delta}$ term encapsulates the geometry of the lattice. While not diagonal yet [3], $\mathcal{H}_{SW}$ can be easily diagonalised by a Bogoliubov transformation:

$$\alpha_{\mathbf{k}} = u_{\mathbf{k}}a_{\mathbf{k}} - v_{\mathbf{k}}b_{-\mathbf{k}}^{\dagger} \qquad\qquad \alpha_{\mathbf{k}}^{\dagger} = u_{\mathbf{k}}a_{\mathbf{k}}^{\dagger} - v_{\mathbf{k}}b_{-\mathbf{k}}$$

$$\beta_{\mathbf{k}} = u_{\mathbf{k}}b_{\mathbf{k}} - v_{\mathbf{k}}a_{-\mathbf{k}}^{\dagger} \qquad\qquad \beta_{\mathbf{k}}^{\dagger} = -v_{\mathbf{k}}a_{-\mathbf{k}} + u_{\mathbf{k}}b_{\mathbf{k}}^{\dagger} \tag{2.13}$$

The bosonic commutation relations $\left[\alpha_{\mathbf{k}}^{\dagger}, \alpha_{\mathbf{k}}\right] = \left[\beta_{\mathbf{k}}^{\dagger}, \beta_{\mathbf{k}}\right] = 0$ require the coefficients u and v to satisfy the condition $|u|^2 - |v|^2 = 1$. $\mathcal{H}_{SW}$ can thus finally be written in diagonal form as:

$$\begin{aligned}\mathcal{H}_{SW} &= E_N + zJS\sum_{\mathbf{k}}\sqrt{1-\gamma_{\mathbf{k}}^2}\left[\left(\alpha_{\mathbf{k}}^{\dagger}\alpha_{\mathbf{k}} + \frac{1}{2}\right) + \left(\beta_{\mathbf{k}}^{\dagger}\beta_{\mathbf{k}} + \frac{1}{2}\right)\right] & (2.14)\\ &= E_N + \sum_{\mathbf{k}}\omega_{\mathbf{k}}\left(\alpha_{\mathbf{k}}^{\dagger}\alpha_{\mathbf{k}} + \beta_{\mathbf{k}}^{\dagger}\beta_{\mathbf{k}}\right) & (2.15)\end{aligned}$$

where $\omega_{\mathbf{k}} = zJS\sqrt{1-\gamma^2}$ is the spin wave dispersion, and is degenerate for α and β bosons (figure 2.3). Spin wave dispersions can be measured experimentally with great precision using neutron scattering.

With the spin wave Hamiltonian finally diagonal, it is now also possible to evaluate the quantum correction to the classical ground state energy as follows:

$$\begin{aligned}\mathcal{E}_{gs} &= -\frac{zNJS^2}{2} + zJS\sum_{\mathbf{k}}\sqrt{1-\gamma_{\mathbf{k}}^2} - 1 & (2.16)\\ &= -\frac{zNJS}{2}\left[S + \frac{2}{N}\sum_{\mathbf{k}}\left(1 - \sqrt{1-\gamma_{\mathbf{k}}}\right)\right] & (2.17)\end{aligned}$$

In the case of the $S = 1/2$ Heisenberg square lattice antiferromagnet (QHSA), the lowering in energy versus the classical ground state $\delta E = 0.158$, with $E_N = 1$. The

---

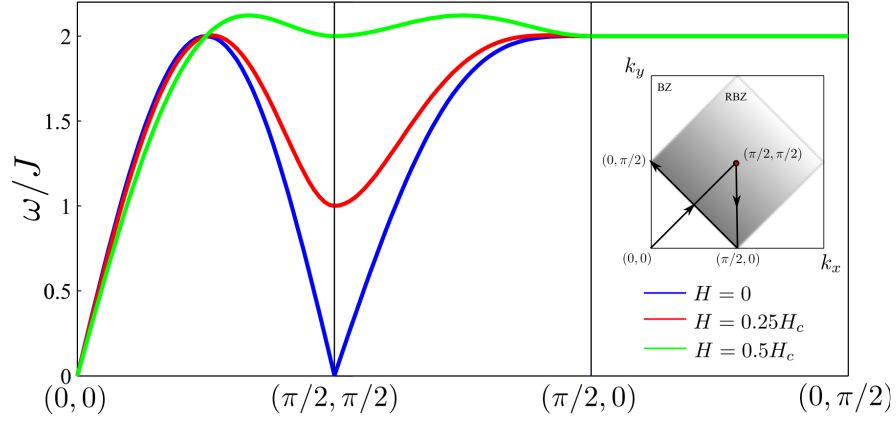[3] After all, the ground state is not the vacuum of bosons.

Figure 2.3: The dispersion relation $\omega_{\mathbf{k}}$ of the square lattice Heisenberg antiferromagnet along the high symmetry directions of the Brillouin zone in several different magnetic fields. H_c is the saturation magnetization.

amount of energy by which the quantum ground state is reduced versus the classical again depends inversely on the size both S and z, as expected.

While the ground state of the spin wave Hamiltonian contains no Bogoliubov bosons $\alpha_{\mathbf{k}}$ and $\beta_{\mathbf{k}}$, the true ground state will contain a finite number of $a_{\mathbf{k}}$ and $b_{\mathbf{k}}$ due to quantum fluctuations. These reduce the magnetization on a given sublattice by the expectation value of the boson number on that sublattice:

$$
\begin{aligned}
m = S - \delta S &= S - \frac{1}{N} \sum_{\mathbf{k}} \left(\left\langle a_{\mathbf{k}}^{\dagger} a_{\mathbf{k}} \right\rangle + \left\langle b_{\mathbf{k}}^{\dagger} b_{\mathbf{k}} \right\rangle \right) \\
&= S - \frac{1}{N} \left(\sum_{\mathbf{k}} \frac{1}{\sqrt{1 - \gamma_{\mathbf{k}}^2}} - 1 \right)
\end{aligned}
\tag{2.18}
$$

Substituting the sum for an integral, the reduction of the sublattice magnetisation, δS, becomes:

$$
\delta S = \frac{1}{2} \left(\int \frac{d^D \mathbf{k}}{(2\pi)^D} \frac{1}{\sqrt{1 - \gamma_{\mathbf{k}}^2}} - 1 \right)
\tag{2.19}
$$

For the square lattice, $\delta S = 0.175$, which corresponds to 35% of the spin length, a rather large reduction; the earlier supposition that low z favours quantum fluctuations thus appears to be correct. One important consideration which has not been made yet is for dimensionality. In the above expression, the dimensionality of the lattice, D, enters through the sum over $\mathbf{k}$, which in the integral representation becomes a D

Model	LRO	E_q	δS
3D Cubic	Yes	0.097	0.078
2D Triangular	Yes	0.220	0.39
2D Square	Yes	0.158	0.65
1D Chain	No	$\frac{2}{\pi}$	0

Table 2.1: The spin wave values the quantum correction to the classical ground state energy, E_q. and sublattice magnetization for some simple lattices in one, two, and three dimensions.

dimensional integral. In one dimension, this integral diverges entirely, meaning that the sublattice magnetisation vanishes – in other words, quantum fluctuations destroy classical order in one dimension. Thus, one dimensional systems are a natural place to look for exotic quantum ground states. In two dimensions and above, the integral generally remains finite, though in some special cases, it diverges. The spin reduction is the smallest for $3D$ lattices. In the case of the $S = 1/2$ cubic lattice, δS becomes only 15% of the spin length, a fact that is verified by neutron scattering [de Jongh and Miedema (2001)]. The ground state energies and spin reductions for a variety of lattices are given in table 2.1.

2.1.5   Finite Clusters

Spin wave theory allows for solution of the Heisenberg Hamiltonian in the thermodynamic limit, giving access to quantities such as the sublattice magnetisation, an important indicator of the stability of classical order. It is, however, not the only way to identify a potential quantum magnet – the low energy spectrum of an exactly diagonalisable cluster for a given model also contains many clues as to the behaviour of the system in the thermodynamic limit. For a two dimensional bipartite system with two sublattice order (such as the QHSA), the lowest set of eigenvalues (up to $S \sim \sqrt{N}$) can be described with the Hamiltonian of a quantum rotor (like a diatomic molecule) [Fisher (1989)],[Neuberger and Ziman (1989)]:

$$\mathcal{H}_{eff} = E_0 + \frac{\mathbf{S}^2}{2N\chi_0} \tag{2.20}$$

$$E(S) = E_0 + \frac{S(S+1)}{2N\chi_0} \tag{2.21}$$

where E_0 is the ground state energy, and $1/N\chi_0$ is the inverse susceptibility. In the thermodynamic limit, the latter term vanishes, resulting in the lowest energy level in each S sector becoming degenerate. It is this collapse of the so-called quasi-degenerate

joint states (QDJS) which mark the rotational symmetry breaking characteristic of long range order. The nature of the order may be surmised from the symmetry of the $E(S)$ states, which possess the symmetry of the ordering wavevector. In the case of the triangular lattice antiferromagnet, for example, the QDJS correspond to wavevectors of $\mathbf{k}_1 = (0,0)$ and $\mathbf{k}_2 = (\pm 4\pi/3, 0)$.

Returning to the finite size sample, the next set of energy levels above the QDJS are the magnon bands, which develop into the spin waves discussed in the previous section in the thermodynamic limit. As system size increases, the lowest energy levels of the magnons tend towards E_0 as $1/\sqrt{L}$, revealing the ungapped spectrum characteristic of a long range ordered antiferromagnet.
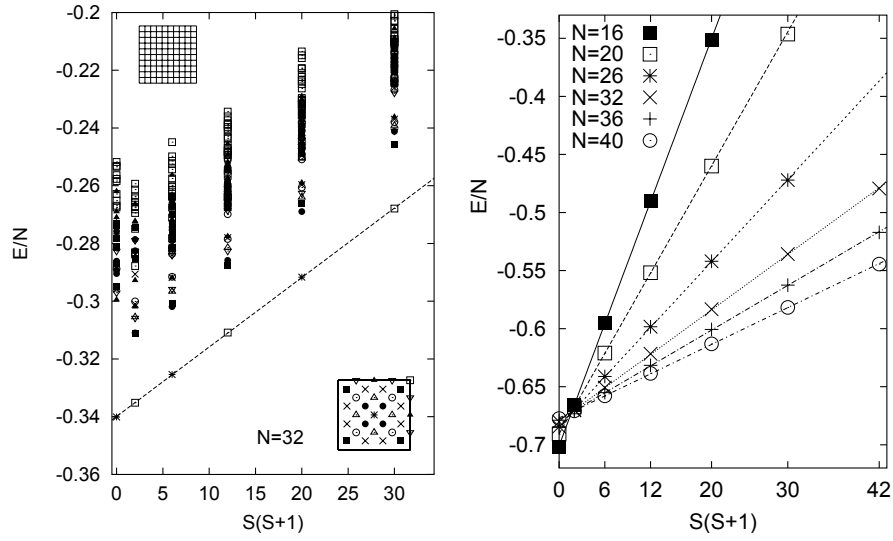

Figure 2.4: (left) The low energy spectrum versus $S(S+1)$ for the $S = 1/2$ Heisenberg square lattice antiferromagnet (right) The scaling of the lowest energy eigenstates for a range of different system sizes. The spectrum collapses towards E_0 linearly with N, as expected for a set of QDJS. Also, the ground state energy per bond converges to approximately -0.355 [Richter *et al.* (2004)], which is practically identical to the spin wave estimate of -0.3552 [Zheng and Hamer (1993)]. Figure adapted from J. Richter. *et. al.* [Richter *et al.* (2004)]

Taking the QHSA as an example again, it is possible to access lattice sizes up to 40 numerically due to the small spin and high symmetry. The resulting spectrum, as calculated by Richter and Honecker [Richter *et al.* (2004)], is shown in figure 2.4. As expected, the lowest energy eigenvalues in each spin sector obey equation 2.21. Furthermore, by considering the scaling of $E_{min}(S)$ with system size N, it can be deduced that $E_{min}(S) \to E_0$ as $N \to \infty$. In other words, the QDJS show that $S = 1/2$ square lattice antiferromagnet does order in the thermodynamic limit. A similar

analysis can be performed for more complicated topologies than the square lattice –
here, the number of QDJS scales as the number of sublattices, or, in the case of helical
orders, as twice the number of sublattices.

Signs of exotic magnetic behaviour may be observed in the absence of a clear set of
QDJS, or, more subtly, in unusual scaling of these. If the gap between the lowest lying
singlet state and the lowest states in other spin sectors does not close as $N \to \infty$, a
gapped ground state, usually composed of singlets or some other localised object, is
implied. More exotic finite size spectra, for instance, when the gap between the lowest
$S = 0$ and $S = 1$ levels is filled with singlets, can imply even more unusual orders (see
figure 2.5).

Figure 2.5: The low energy spectra of (left) a classically ordered magnet (centre) a gapped
system and (right) an exotic quantum ground state. After F. Mila. [Mila (2000)].

2.1.6   Frustration

Except for the particular case of one dimension, it appears from the discussion so far
that classical order is rather persistent with respect to quantum fluctuations. There
are however other means of destabilising long range order beyond small D, small S,
and small z. This becomes apparent if Ising spins [4] are placed on each corner of
an equilateral triangle, then coupled antiferromagnetically – the resulting situation,
where it is impossible to satisfy all interactions simultaneously, is called frustrated
[Toulouse (1977)], and is shown in figure 2.6. Frustration can be realised in a number
of other ways, such as through competing nearest neighbour interactions, next-nearest-
neighbour interactions (figure 2.6) or spatial disorder.

Returning to the case of the isolated triangle, and geometric frustration: if the Ising
spins are replaced by classical Heisenberg spins, the frustration is partly relieved by
the adoption of a compromise ground state with the spins coplanar and oriented at

---

[4]Spins with only one component. The spins lie along an axis and may point only up or down with
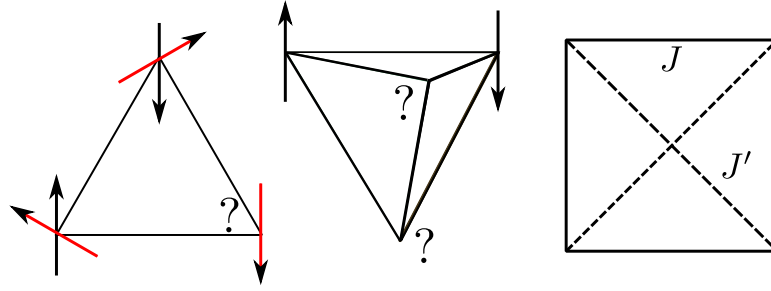respect to this axis.

Figure 2.6: (left) A single triangle with Ising (black) and Heisenberg (red) spins. The Ising spins are unable to satisfy all nearest neighbour couplings simultaneously, resulting in a ground state degeneracy. In the case of Heisenberg spins, the frustration is relieved by adoption of a coplanar $120°$ state. A twofold degeneracy associated with the chiraliy κ remains, however (see figure 2.7). (centre) Another frustrated unit, a tetrahedron. When populated with Ising spins, the ground state is again degenerate. (right) An example of frustration on a square plaquette with next nearest neighbour couplings. If both J and J' are antiferromagnetic, it is impossible to satisfy all interactions simultaneously. If many such plaquettes are assembled in an edge-sharing manner, the so called frustrated square lattice results. The Heisenberg model on this lattice exhibits a breakdown of classical order at the point $J = 2J'$. As will be seen later in this chapter, this is a consequence of being able to rewrite the classical ground state as a local constraint.

$120°$ with respect to each other. The energy per site of this state is only $-JS^2/4$, versus $-JS^2/2$ for fully antiparallel spins – from this fact alone, one might expect an enhancement of quantum effects. Furthermore, there are two degenerate ways to realise the $120°$ degree state, which are not connected by a simple global rotation of the spins: to describe these, a so-called scalar chirality, κ, may be defined as follows:

$$\kappa = \left(\frac{2}{3\sqrt{3}}\right)\left(\vec{S}_1 \times \vec{S}_2 + \vec{S}_2 \times \vec{S}_3 + \vec{S}_3 \times \vec{S}_1\right) \tag{2.22}$$

where the sites are indexed in the clockwise direction and κ may take on values of ± 1. When many triangles are put together, the intriguing possibility of a disordered, enormously degenerate ground state arising from this degree of freedom arises, providing it survives in the thermodynamic limit. This does not happen in the case of the triangular lattice ($z = 4, D = 2$), where the edge sharing of the triangular building blocks destroys the twofold degeneracy, but is a possibility for corner sharing geometries.

Even though the classical ground state of the triangular lattice is (dissapointingly) ordered, the effect of frustration again becomes apparent when the spherical symmetry of the Heisenberg model is reduced to axial by application of a magnetic field $\mathbf{H}$.

Returning to the case of the isolated triangle, the classical ground state becomes any of an infinite number of configurations which fulfill the condition $\vec{S}_1 + \vec{S}_2 + \vec{S}_3 = \mathbf{H}/2J$ (figure 2.7). In the thermodynamic limit, this infinite degeneracy is reduced to 2 possible long range ordered ground states: either a coplanar up-up-down (UUD) state, or an umbrella state.

Reducing the spin length from ∞ to the quantum limit $S = 1/2$, the first question which arises is whether the zero field classical ground state survives in the presence of quantum fluctuations. While this was a hotly debated topic for a number of decades, it is now well established that the $S = 1/2$ triangular lattice antiferromagnet indeed orders at $T = 0$ [Huse and Elser (1988)]. The frustration strongly reduces the sublattice magnetization to only 40% of its classical value, however, considerably smaller than the value calculated for the QHSA of 65%.

Having established that the ordered ground state persists at $H = 0$, it is time to return to the finite field ground state. In the quantum limit, the degeneracy between the classically degenerate UUD and umbrella states is destroyed by a somewhat counterintuitive phenomenon known as order by disorder [Villain *et al.* (1980)],[Chubukov and Golosov (1991)]. As demonstrated in the previous section on spin wave theory, quantum fluctuations lower the classical ground state energy through a term containing the integral of the spin wave dispersion. In the case of the quantum triangular antiferromagnet in a magnetic field, it turns out that the UUD state is favoured over the umbrella by this term. Thus, quantum fluctuations play a dual role in frustrated spin systems - while destabilising the ground state, they may simultaneously select a long range order from the degenerate manifold of classical states. Similar arguments to the above can be made for ground state selection at finite temperatures by thermal fluctuations.

As hinted at earlier, the connectivity between the triangles is another way to induce degeneracies in the classical ground state. This can be illustrated by considering the simple example of two triangles sharing a single vertex: the ground state allows for free rotation of the four non-shared spins about the axis of the shared spin. Even when the spin directions are fixed on one triangle, the twofold chiral degree of freedom remains for the other, unlike in the edge sharing geometry (figure 2.7).

Extending from two triangles to an infinite number, the local rotational degree of freedom results in a macroscopic degeneracy within ground state manifold, with the only constraint being that on a single triangle $\vec{S}_1 + \vec{S}_2 + \vec{S}_3 = 0$. Thus, a criterion for breakdown of classical order in frustrated systems is that the Hamiltonian is expressable as a sum over the basic building blocks of the lattice [Chalker (2009)], be they triangles,
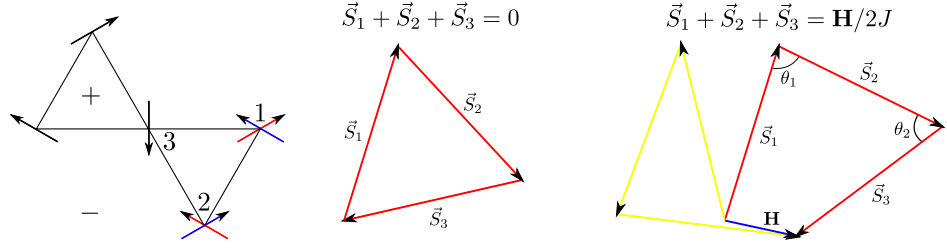
Figure 2.7: (left) Two triangles arranged in a corner sharing geometry. Even when the chirality is fixed on one triangle (left), there remains a twofold degeneracy associated with the choice of chirality on the adjacent triangle, represented by the red and blue arrows. In the edge sharing geometry this additional degeneracy is suppressed, as is the case for the triangular lattice. (centre) A graphical representation of the condition which defines the ground state of a single triangular plaquette. (right) Ground state degeneracy may be restored by applying a magnetic field, $\mathbf{H}$, perpendicular to the plane of the plaquette. The new ground state condition allows for an infinite number of possible spin arrangements. One ground state is shown in red, another possibility in yellow.

tetrahedra, or more exotic units. That is:

$$\mathcal{H} = \sum_{\langle i,j \rangle} \vec{S}_i \cdot \vec{S}_i = \frac{J}{2} \sum_z |\vec{L}|^2 + c \tag{2.23}$$

where $\vec{L} = \vec{S}_1 + \vec{S}_2 + \vec{S}_3$, the sum over z is a, and c is a constant.

Are order from disorder mechanisms again able to select a unique ground state from the degenerate ground state manifold, as they did for the triangular lattice? As it turns out, not quite: to demonstrate this, consider the example of the kagome lattice ($z = 4, D = 2$) [5], a $2D$ lattice composed of triangles arranged in a traditional pattern of Japanese basketweaving [Syozi (1951)]. As for the triangular lattice, order by disorder [6] enforces a coplanar ground state. The chiral degree of freedom remains in the reduced ground state manifold, however, suppressing long range order. In Monte Carlo simulations on the classical kagome antiferromagnet, it is found that correlations tend towards a motif with staggered chirality known as $\sqrt{3} \times \sqrt{3}$ order [Reimers and Berlinsky (1993)] [7], but this order is only short ranged. Going from the $S = \infty$ case to finite spin, spin wave theory on the $\sqrt{3} \times \sqrt{3}$ state shows a completely flat mode at $\omega_0 = 0$, indicative of its instability with respect to quantum fluctuations [Yildirim and Harris (2006)].

---

[5] This lattice will be discussed extensively in chapter 5.
[6] this time through thermal fluctuations, as we are discussing a classical model
[7] The unit cell increases in size by $\sqrt{3}a$ along both dimensions, where a is the nuclear lattice parameter.

Reducing the number of shared spins between two triangles from two (edge sharing) to one (corner sharing) has seemingly done the trick – the classical ground state in the thermodynamic limit will retain the degeneracy of the isolated units which compose the lattice. This thesis will consider several systems where frustration is an important ingredient in leading to exotic physics.

2.2   The "Zoo" of Quantum Ground States

Now that the ingredients which lead to breakdown of classical order in magnetic systems have been identified as small S, low D, low z, and frustration (geometric or otherwise), it is time to investigate what kind of states may replace the classical long range ordered state, and what their characteristics are. In this discussion, only states arising at the quantum limit of the Heisenberg model on ordered lattices will be considered – that is, states like disorder induced spin glasses and classical cooperative paramagnets will be ignored.

An oft used umbrella term to describe states with an absence of classical long range order is spin liquid. This does not necessarily mean that the correlation functions and dynamics of the state in question correspond to those of actual liquids, but rather that the state does not break the symmetry of the lattice and/or the spin despite strong correlations. There are a vast multitude of states which fulfill either one or both of these conditions, some of which are be briefly summarised below:

2.2.1   Algebraic Spin Liquids

Earlier in this chapter, it was shown that classical order in the $1D$ Heisenberg chain model is destroyed by quantum fluctuations. One question which naturally arises from this observation is; what replaces classical order as the ground state? While answering this is generally not trivial, an exact solution fortunately exists in the case of the $S = 1/2$ Heisenberg chain. Furthermore, it is amenable to a number of other approaches, including conformal field theory and bosonization, and powerful numerical methods such as density matrix renormalization group (DMRG). This renders the $S = 1/2$ Heisenberg chain one of the best understood models in quantum magnetism.

Even though the ground state has zero sublattice magnetization, it is surprisingly found to be Néel ordered on a rather large length-scale. Indeed, the correlation function

$\langle S_i S_{i+r} \rangle$ decays with distance r as:

$$\langle S_i S_{i+r} \rangle \sim \frac{(-1)^{|r|}}{|r|} S^2 \qquad (2.24)$$

An algebraic decay of $\langle S_i S_{i+r} \rangle$ is a characteristic feature of a system close to a phase transition, where correlations diverge before long range order sets in. As a result, the ground state is often called a critical spin liquid. Also in common with long range ordered systems is the presence of gapless excitations. One crucial difference between these and their long range order analogues is that while the latter are $S = 1$ magnons, the excitations in the ground state of the $1D$ chain are spinons, gapless $S = 1/2$ quasiparticles. In a cartoon picture of the ground state, these may be regarded domain walls which can move at no energy cost.

The existence of algebraic liquid states in two dimensions is still a point of contention, though the $S = 1/2$ kagome antiferromagnet is one model for which such a state has been found to be a possibility [Hermele *et al.* (2008)].

2.2.2 Valence Bond Crystals and Solids

One of the simplest solutions for the ground state of a frustrated lattice model is the valence bond solid (VBS), an ordered covering of the lattice by singlets. Depending on the details of the lattice and interactions, these may be dimers, tetramers or even larger objects. Generally, in VBS type ground states, the correlation function decays exponentially with distance:

$$\langle S_i S_{i+r} \rangle \sim S^2 e^{-\frac{r}{\zeta}} \qquad (2.25)$$

where ζ is the correlation length. In an ideal VBS, the correlations are limited in extent to the singlet unit, but usually fluctuations render ζ slightly longer in distance. Although the $SU(2)$ rotational symmetry of the spins is preserved in such a ground state, this is not necessarily true of the translational symmetry. Depending on whether or not this is broken, two classes of VBS arise: spontaneous VBS, where the translational symmetry is destroyed by singlet formation, and explicit VBS, which are translationally invariant (see figure 2.8). The former is typically encountered when the Hamiltonian contains competing interactions, such as next nearest neighbour (nnn) couplings, whilst the latter occurs when an alternation of exchanges isolate a structural unit capable of singlet formation. Another universal feature of a VBS ground state is a gap to the lowest lying magnetic excitation. This gap is connected with the breaking of the singlet objects making up the ground state. The excitations above the gap are not universal, however.

One famous example of a spontaneous VBS state is the ground state of the $S = 1/2$ chain with antiferromagnetic nnn couplings, J_2, topologically equivalent to an edge sharing ladder of triangles [8]. In a broad region of the phase diagram with respect to the frustration parameter $\alpha = J_2/J_1$, the frustrating interaction J_2 induces a dimerisation of neighbouring spins into localised singlets residing on the J_1 bonds. The resulting ground state is doubly degenerate, as the singlets may cover either right or left leaning diagonals along the chain. Spin excitations are, as in the uniform chain, $S = 1/2$ spinons, although the excitation spectrum has now acquired a gap connected to the breaking of a nearest neighbour singlet. Spontaneous VBS are also observed in two dimensional models where the unit cell of the lattice contains an even number of spins, such as the square lattice with 3rd nearest neighbour couplings. In this case, the ground state is singly degenerate, and the excitations are $S = 1$ magnons.

A typical case of an explicit VBS is encountered on the so-called Shastry-Sutherland lattice, a square lattice where every second triangle is decorated by a diagonal bond. The ground state in the limit of the diagonal bonds, J, being stronger than the square bonds, J', consists of singlets on the diagonal bonds. Frustration is thus relieved by effectively "switching off" the frustrating coupling, J. In this state, the ground state remains both translationally and spin rotationally invariant. Excitations are gapped, and confined even at rather large J' due to frustration, which results in a rather flat dispersion.

Returning to the Heisenberg chain model, the ground state takes on radically different character if S is increased from $1/2$ to 1 (or more generally, for any integer S). In this case, rather than possesing algebraic correlations and gapless spinon excitations, the ground state exhibits extremely short range correlations, consistent with condensation of nearest neighbour singlets, as well as gapped $S = 1$ magnons in the excitation spectrum. The origin of these singlets is initially puzzling, as the lattice translational symmetry apparently remains unbroken. To explain this apparent paradox, Haldane made the observation that the $S = 1$ spins can be broken into two $S = 1/2$ "virtual" spins, each of which may form a singlet with a similar object on a neighbouring site. As such, the $S = 1$ chain is often called the Haldane chain, with the resulting gap between the ground state and first excited triplet referred to as the Haldane gap. A powerful proof of the validity of this interpretation are the presence of end of chain defects with $S = 1/2$, observable in NMR experiments on doped samples.

While the spin correlations decay exponentially in both VBS and VBC states, they do possess a long range order of sorts in the singlet-singlet correlations. Thus, the order

---

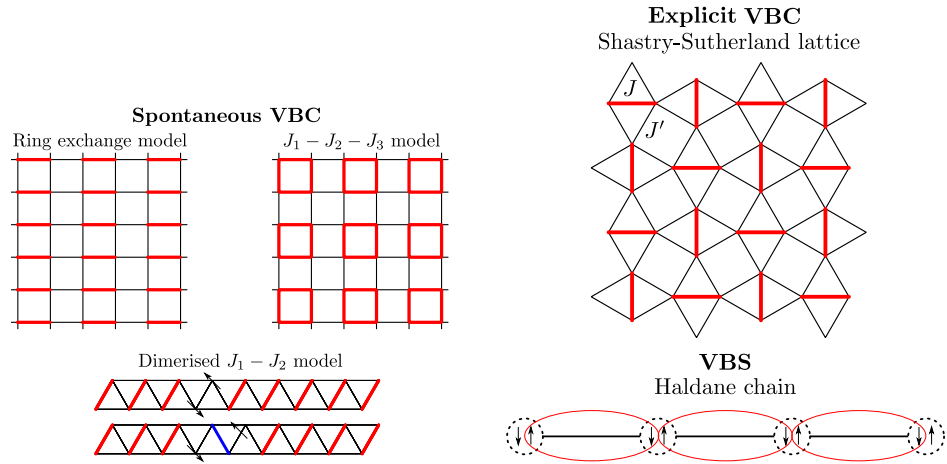[8]Again, this model will be covered in greater detail in Chapter 4.

Figure 2.8: (left) Some examples of spontaneous VBS, including the ring exchange and $J_1 - J_2 - J_3$ models on the square lattice, and the $S = 1/2$ $J_1 - J_2$ chain. The lattice symmetry is broken by singlet formation. (right) An explicit VBS on the Shastry-Sutherland lattice (above) and VBC on the Haldane chain (below). For the latter, the dotted circles denote a single site, with the red ellipses indicating singlets.

parameters of these states are typically formulated in terms of such objects.

2.2.3 RVB Liquid

Originally proposed by Anderson and Fazekas for the triangular lattice in 1973 [Anderson (1973)], the resonating valence bond, or RVB, state may be considered a fluctuating analogue of the VBS and VBC states. Its wavefunction is expressed as a superposition of dimer coverings over the entire lattice as follows:

$$|\psi_{RVB}\rangle = \sum_{\mathcal{C}_i} A(\mathcal{C}_i) |\mathcal{C}_i\rangle \tag{2.26}$$

where $\mathcal{C}_i$ is a dimer configuration, usually expressed as a product of singlet states, $A(\mathcal{C}_i)$ is an amplitude, and the sum runs over all such possible configurations. There are two flavours of RVB liquid, depending on the nature of the dimer wavefunctions used: a short range liquid, where the amplitude of a dimer configuration $a(h, k)$ decays exponentially with distance, and a long range liquid, where $a(h, k)$ falls off algebraically. Generally, the former has been considered in the greatest detail so far, as it is possible to treat the problem in a nearest neighbour singlet basis known as the quantum dimer model.

Thus far, the RVB state has mainly been found to arise for rather artificial models, like the quantum dimer model on the square and triangular lattices [Rokhsar and Kivelson

State	Spatial Symmetry	Spin Symmetry
Néel	✓	✓
VBS (Spontaneous)	✓	✗
VBS (Explicit)	✓	✓
RVB	✗	✗
Critical/algebraic SL	✗	✓
Nematic	✗	✓

Table 2.2: Some magnetic ground states and their broken symmetries.

(1988)]. An experimental realisation in a condensed matter system thus remains on the distant horizon.

2.2.4   Nematic Phases

The spin liquid states discussed so far have all retained the $SU(2)$ spin rotational symmetry of the Heisenberg model. It is also possible for a spin liquid state to break this symmetry, but leave the translational symmetry of the lattice untouched. Broadly speaking, such states are called nematic, as they (like liquid crystals) are disordered in the spin correlations, but nonetheless show an ordering in the spin fluctuations. Such order can often be captured in the higher powers (quadrupolar, octupolar etc.) of the spin operators. One example of a nematic phase is encountered on the square lattice when S is increased to 1 and a biquadratic exchange $(\mathbf{S}_i \cdot \mathbf{S}_j)^2$ is added to the Heisenberg Hamiltonian [Tóth (2010)].

2.3   Anisotropies: Switching Quantum Mechanics Off Again

The discussion so far has assumed perfect isotropy of the Heisenberg spins, only bilinear $(\mathbf{S}_i \cdot \mathbf{S}_j)$ interactions between them, and in the case of low dimensional models, no $3D$ couplings between the structural elements (*i.e.* chains, planes, etc.). As we know, however, things are very rarely so simple in nature. This section will address some of the perturbations which arise in real systems, in particular anitrosopies of both the single ion and exchange variety.
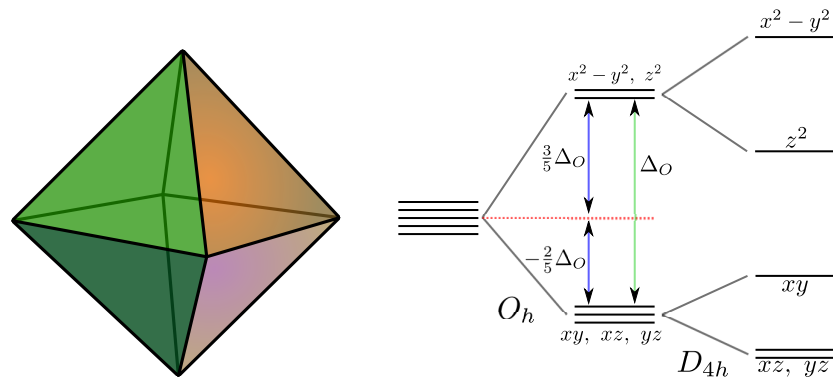
Figure 2.9: (left) The octahedral coordination and (right) its level splitting scheme. Additional splitting due to a tetragonal Jahn-Teller distortion is also shown.

2.3.1 Crystal Fields, Spin Orbit Coupling and Resulting Anisotropies

Because the rich physics described so far occurs within the bounds of the Heisenberg model, it is natural to look to first row transition metal ions as sources of spin for experimental realisations. In these ions, the orbital moment is often considered quenched (though this is not always the case), which means that spin-orbit coupling to crystal field split levels is at first order excluded as a source of spin anisotropy. In order to understand why this is the case and under what circumstances it is not, it is necessary to consider in a little more detail the behaviour of d-orbitals in both symmetric and asymmetric crystal fields. We will concentrate on two electronic configurations: d^1 and d^9, as these not only correspond to the configurations of the Cu^{2+} and Ti^{3+} ions which form the basis of the experimental part of this work, but also because they are instructive in illuminating the physics of individual $3d$ metal ions.

In the free ion case, the five $3d$ levels are degenerate, and the ground state term symbol is ^2D for both the d^1 and d^9 configurations. When an octahedral crystal field is applied to these states, they are split into a lower triplet of t_{2g} symmetry, and an upper doublet of e_g symmetry (see figure 2.9). As the $3d$ orbitals are quite extended in space, they interact strongly with the crystal field, and the splitting between the t_{2g} and e_g levels is typically on the order of 1 eV, which is far greater than both the spin orbit (LS) coupling and Hund's third rule. An important consequence of this is that Hund's third rule breaks down - that is, J is no longer a good quantum number (though L and S so far remain unaffected). Therefore, in determining the magnetic properties of a single ion the ground state resulting from the crystal field must be considered.

The basis functions for the t_{2g} and e_g levels may be constructed from linear combina-

tions of the spherical harmonics $\mathcal{Y}_l^m$ as follows:

$$
\left.\begin{array}{r}
\dfrac{ir^2}{m}[\mathcal{Y}_2^2 - \mathcal{Y}_2^{-2}] \sim xy \\[2mm]
r^2[\mathcal{Y}_2^1 - \mathcal{Y}_2^-1] \sim xz \\[2mm]
r^2[\mathcal{Y}_2^1 + \mathcal{Y}_2^-1] \sim yz
\end{array}\right\} t_{2g}
\qquad
\left.\begin{array}{r}
r^2[\mathcal{Y}_2^2 + \mathcal{Y}_2^{-2}] \sim x^2 - y^2 \\[2mm]
r^2 \mathcal{Y}_2^0 \sim 3z^2 - r^2
\end{array}\right\} e_g
$$

An important observation about these functions, called tesseral harmonics, is that they are all real functions. Therefore, acting on them with the purely imaginary angular momentum operator $\mathbf{L}$, will only yield a real eigenvalue if $\langle L \rangle = 0$. The orbital moment is thus (apparently) quenched. This is not necessarily true in all cases, however – the above choice of basis is not unique, and the complex basis $\{\mathcal{Y}_2^{-1}, \mathcal{Y}_2^2 - \mathcal{Y}_2^{-2}, -\mathcal{Y}_2^1, -\mathcal{Y}_2^1, \mathcal{Y}_2^0, \mathcal{Y}_2^2 + \mathcal{Y}_2^{-2}\}$ (in that order) may instead be chosen. The angular momentum operators can thus be rewritten:

$$
L_x = -\frac{1}{\sqrt{2}}
\left(\begin{array}{ccc|cc}
0 & 1 & 0 & -\sqrt{3} & -1 \\
1 & 0 & 1 & 0 & 0 \\
0 & 1 & 0 & \sqrt{3} & 1 \\ \hline
-\sqrt{3} & 0 & \sqrt{3} & 0 & 0 \\
1 & 0 & 1 & 0 & 0
\end{array}\right)
\tag{2.27}
$$

$$
L_y = \frac{i}{\sqrt{2}}
\left(\begin{array}{ccc|cc}
0 & 1 & 0 & \sqrt{3} & -1 \\
-1 & 0 & 1 & 0 & 0 \\
0 & -1 & 0 & \sqrt{3} & -1 \\ \hline
-\sqrt{3} & 0 & -\sqrt{3} & 0 & 0 \\
1 & 0 & 1 & 0 & 0
\end{array}\right)
\tag{2.28}
$$

$$
L_z = -
\left(\begin{array}{ccc|cc}
1 & 0 & 0 & 0 & 0 \\
0 & 0 & 0 & 0 & -2 \\
0 & 0 & -1 & 0 & 0 \\ \hline
0 & 0 & 0 & 0 & 0 \\
0 & -2 & 0 & 0 & 0
\end{array}\right)
\tag{2.29}
$$

Looking closely at these matrices, it becomes apparent that the top left quadrant, corresponding to the t_{2g} subspace, has a rather similar form to the angular momentum operators for $L = 1$ (p) orbitals. In fact, the two are simply related by $\mathbf{L}_{t_{2g}} = -\mathbf{L}_p$. On the other hand, the bottom right quadrant, describing the e_g orbitals, shows complete quenching. What are the implications of this for, respectively, d^1 and d^9 electronic configurations when the crystal field is perfectly octahedral? Also, what happens when the octahedral symmetry is lifted, by for example a Jahn-Teller distortion?

- O_h **Symmetry**: When the t_{2g} level contains only one electron, as is the case for Ti^{3+}, the spin-orbit coupling to the effective $L = -1$ angular momentum lifts the threefold degeneracy of the ground state. The resulting spin-orbit ground state is a Kramers doublet with both $L = 0$ and $S = 0$. In the d^9 case, on the other hand, the orbital moment is completely quenched (as expected), and only the spin angular momentum contributes to the total moment[9].

- **Jahn-Teller Distorted**: In a real material, of course, the crystal field is rarely of perfect O_h symmetry. This is often a consequence of the Jahn-Teller distortion, which (at least partially) lifts the degeneracy of degenerate electronic configurations. If this results in a singly degenerate ground state, the orbital angular momentum is quenched again, and the magnetic moment is due to the spin only. Even in these circumstances, application of the spin orbit (LS) coupling may restore some orbital angular momentum by mixing higher lying orbital states (with $L \neq 0$) into the ground state. The magnitude of the restoration of the moment is proportional to λ^2/Δ, where Δ is the splitting between the ground and excited orbital states and λ is the spin-orbit coupling constant. The deviation from perfect Heisenberg spin symmetry, or single ion anisotropy, due to the LS coupling is written:

$$\mathcal{H} = DS_z^2 + E(S_x^2 - S_y^2) \tag{2.30}$$

  where the sign and magnitude of D and E depend on the details of the crystal field.

  The effect of a small single ion anisotropy on a quantum ground state is generally to favour long range order. For example, in the $1D$ spin chain, the sublattice magnetization in the presence of a small anisotropy along the z-direction is restored as $(1/\pi)\log\left[(1 + d)/d\right]$, where $d = D/(4|J|)$.

Additional anisotropies may arise when the magnetic exchange between ions is switched on. One example of particular importance is the Dzyaloshinskii-Moriya (DM) interaction, which results from a process whereby two neighbouring atoms are simultaneously excited by the exchange interaction, J, before being restored to their respective ground states by the LS coupling. This process has an amplitude $(\lambda t_{ij}^2/\Delta U)$.

The Dzyaloshinskii-Moriya Hamiltonian is written:

---

[9]In fact, this is not always true when the exchange interaction, J, between ions is switched on. If the spin orbit (LS) coupling excites an ion to an orbital state with nonzero L, the exchange interaction will acquire an anisotropic component. This is called exchange anisotropy, and can be responsible for shifts in the g-value of up to 10%.

$$\mathcal{H}_{DM} = \mathbf{D}_{ij}\mathbf{S}_i \times \mathbf{S}_j \qquad (2.31)$$

where $\mathbf{D}_{ij}$ is the DM vector, and has components given according to Moriya's rules [Moriya (1960)]. The first, and most important, of these is that $\mathbf{D}_{ij} = 0$ if the bond between the neighbouring atoms has inversion symmetry. The DM interaction has been found responsible for the small canting of the ordered moment in materials like La_2CuO_4[10] – this effect is called DM ferromagnetism. The influence of the DM interaction on quantum ground states will be discussed in more detail in Chapter 5. Generally, however, they lead to magnetic order.

2.3.2   Interchain and Interplane Couplings

The most common experimental testing grounds for the physics discussed so far are crystalline solids. In order to realise a $1D$ or $2D$ model as a 3-dimensional crystal, the magnetically interesting structural elements (be they chains, planes etc.) must be separated in space. If this separation is imperfect, a residual interchain or interplane interaction, usually denoted J', may be present.

Just like the aforementioned anisotropies, interchain/plane couplings also tend to increase the tendency for long range order [11]. Taking the example of the square lattice antiferromagnet, the ordering temperature increases logarithmically as $T_N = (2.3J)/[2.43 - \ln J'/J]$ when an interplane coupling is introduced.

2.3.3   Summing it all up

This chapter has hopefully provided an overview of the interesting physics which can arise when ingredients like small S, small z, low dimensionality, and geometric frustration are combined within the confines of the Heisenberg model. The materials which will be studied in this thesis all manifest some configuration of these variables, resulting in a range of novel physical properties. Chapter 4 will deal with two $1D$ titanate systems, where one, $KTi(SO_4)_2 \cdot (H_2O)$, provides a rare example of a spontaneous VBS on the frustrated chain lattice, and the other is described as a $1D$ algebraic liquid with spinon excitations. Chapter 5 will mainly concern the kagome lattice antiferromagnets volborthite and herbertsmithite, though mainly focussing on why these compounds do not realise the exotic quantum ground states one expects. As a fitting coda to

---

[10]The end member of the famous $La_{2-x}SrxCuO_4$ family of supercondutors.

[11]One exception being when these are frustrated.

this Chapter, these models are placed on a "master" phase diagram for the $S = 1/2$ Heisenberg model, shown below.
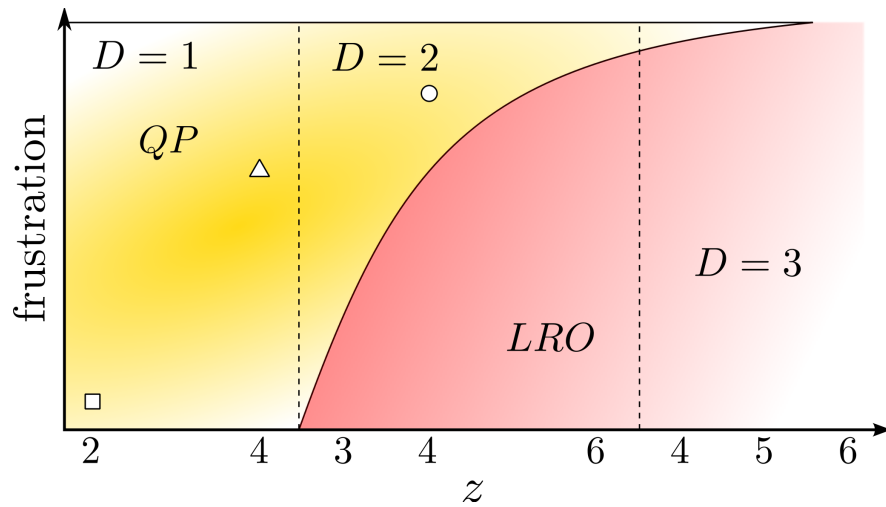

Figure 2.10: Schematic phase diagram for an $S = 1/2$ antiferromagnetic Heisenberg model with respect to frustration, z, and D. The yellow region indicates where long range order breaks down and is replaced by a quantum ground state. The shade of red roughly reflects the size of δS, the reduction in the sublattice magnetization. The triangle represents the frustrated chain lattice model manifested experimentally in the material $KTi(SO_4)_2 \cdot (H_2O)$, while the circle and square indicate the kagome $[Cu_3V_2O_7(OH)_2 \cdot 2(H_2O)$ and $Cu_3Zn(OH)_6Cl_2]$ and chain lattices $[KTi(SO_4)_2]$, respectively.

Chapter 3

Experimental Methods: From Design to Synthesis to Measurements

In the last chapter, the ingredients which lead to novel quantum ground states in spin models were identified. This chapter will focus on how to realise these models experimentally, and how to measure the properties of the resulting materials.

3.1 Sources of Model Magnets

"What would the properties of materials be if we could really arrange the atoms the way we want them?"
– Richard Feynman [Feynman (1960)]

A major obstacle to advancing our understanding of quantum phenomena in the solid state is a dearth of suitable model materials. This lack may be easily understood if one reflects on the long list of conditions which must be fulfilled for such phenomena to occur. First, a suitable source of spin, in terms of both correct value of S and spin symmetry (Ising, XY, or Heisenberg), must be identified – this is typically a transition metal ion or organic radical. Second, these must be arranged into secondary units, like chains or planes, of the desired geometry and connectivity (*e.g.* kagome, square lattice). Third, a three-dimensional structure must be constructed from these units, minimising unwanted interactions between them. Additional considerations such as disorder and anisotropies are also to be accounted for. Creating a new quantum magnet,

in other words, is far from an easy taskF Fortunately, this process may sometimes be circumvented, as the work of preceding chemists and nature have proven rich sources of model magnets.

- **Previously Synthesised Structures** – The scientific literature contains countless examples of magnetic materials, many of which were not necessarily synthesised from the perspective of realising a magnetic model. These form a vast source of potential realisations, which until now has been far from exhausted. Examples of materials originally discovered in this way are shown in chapters 5 and 6.

  If a realisation cannot be directly found in the literature, it is often possible to modify an existing structure to achieve the desired result. For example, a common approach for synthesising transition metal oxide or halide based magnets is substitution of ions in an existing structure (such as pyrochlore, perovskite etc.), since these are often robust and behave predictably, and because the synthesis is relatively straightforward. This approach, while having yielded dozens of much studied magnetic compounds, will not be discussed here, as it is not of direct relevance to the forthcoming chapters.

- **Minerals** – Some more exotic geometries, such as the kagome lattice, have thus far proven elusive to the efforts of synthetic chemists. Interestingly, an especially rich vein of frustrated magnets has been found among minerals, and "data mining" of mineral databases has yielded many much studied materials, such as jarosites, herbertsmithite, volborthite, vesignieite, tapiolite, yavapaiite, and beyond magnetism, the skutterudites. Such materials are often synthesised hydrothermally, as these reaction conditions closely emulate those in the upper crust of the earth, where most minerals are formed.

3.2   Crystal Engineering

Should neither nature or literature yield the desired realisation, an *a priori* approach to synthesising new model magnets must be used. While exact prediction of the final crystal structure of a material from the chemical constituents present in the reaction mixture is currently impossible (if not, there would be a lot of unemployed chemists), there nonetheless exist several means by which the general architecture of a material can be influenced: these strategies are often referred to as crystal engineering, after Schmidt [Schmidt (1971)].

In organic chemistry, the revolution brought about by retrosynthetic analysis in the

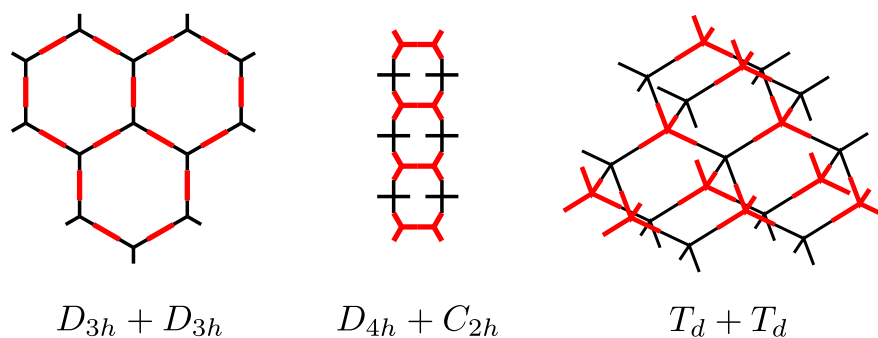$$D_{3h} + D_{3h} \qquad D_{4h} + C_{2h} \qquad T_d + T_d$$

Figure 3.1: Examples of combinations of spin source (black) with bridging ligand (red).

1980's allowed for the synthesis of a number of complex molecules which until then were inaccessible by less rational routes [Corey and Cheng (1995)]. Retrosynthetic analysis involves sequentially breaking the desired molecule into small virtual building blocks called synthons. These virtual objects are then converted into commercially available synthetic equivalents by considering the polarisation at the site of connection with respect to the closest polar functional group. Using this strategy, complex compounds such as natural products may be prepared with relative ease. The concept of retrosynthetic analysis can be borrowed for the purposes of crystal engineering, where the final crystal structure substitutes for the target molecule, and the synthons can be ions, molecules, or even supramolecular objects [Moulton and Zaworotko (2001)]. In the case of the type of magnetic materials we are concerned with, the synthons may be grouped into three categories:

- **Sources of spin** – Usually, charged first row transition metal ions are used as the source of spin, though organic radicals can also fulfill this role. Examples of the latter include the TTF (TTF = tetrathiafulvalene) molecule in the famous Bechgaard salts [Jerome *et al.* (1980)] and the family of $\kappa-$BEDT-TTF$_2$X (BEDT-TTF = bis(ethylenedithio)tetrathiafulvalene, X is a monovalent anion, typically a Cu complex) [Taniguchi *et al.* (2003)], materials. In the present work, the sources of spin used will be the metal ions Ti^{3+} and Cu^{2+}, both which provide $S = 1/2$.

- **Bridging groups** – In order to generate a magnetic lattice, the metal ions must be connected to each other by a bridging group capable of mediating superexchange. This role can be fulfilled by anything from an oxygen atom (Chapter 5) to sulfate ions (Chapter 4) to organic molecules.

- **Spacers** – As established in the previous chapter, quantum phenomena are enhanced in low dimensions. As a result, it is desirable to separate the $1D$ or $2D$ magnetic networks with spacers in a $3D$ crystal. Counterions or solvent may

fulfill this role (for instance, K^+ in Chapter 4), as may neutral co-ligands.

Whereas only polarisation at the site of connection needs to be considered for organic synthons, the "supramolecular" synthons are considerably more complex:

- **Charge** – As the spin source is usually a charged species, charged bridging groups and spacers must also be used. The charge degree of freedom can thus be exploited in the design of a material - for example, if a ligand which does not fully compensate the charge of the spin source is selected, counter ions can be included to play the role of spacers between the structural elements.

- **Symmetry** – The preferred local symmetry of the transition metal ion combined with the symmetry and possible binding modes of the ligand will give all the possibilities for the networks which can be formed from these two species. For example, if the spin source is a transition metal ion favouring octahedral coordination, and the ligand is effectively linear, with a binding site at each end, structures such as chains, square lattices, and cubic lattices are favoured. Figure 3.1 summarises some lattices which can be formed from combinations of transition metal ions and bridging ligands.

- **Noncovalent Bonding** – When the ligand or spacer is organic, or contains hydrogen, it is able to participate in forms of bonding that purely ionic synthons cannot. Two particularly useful types of interaction that can be exploited in crystal engineering are π-stacking and H-bonding.

It is clear that when dealing with such complex objects, structure prediction is unrealistic. Nevertheless, by a combination of luck, trial and error, and a bit of design, new and interesting structures may be realised. In this work, one such structure, $KTi(SO_4)_2 \cdot (H_2O)$, is reported in Chapter 4.

3.2.1   Hydrothermal Inorganic Synthesis

The types of material we would like to apply the above principles to are generally inorganic metal hydrates, and our preferred method is hydrothermal synthesis. This method involves heating the reagents in aqueous solution to temperatures between $100°C$ to $250°C$ inside a teflon-lined steel vessel. The combination of high temperature and high pressure with the aqueous environment emulate the conditions encountered in the upper crust of the earth. Thus, hydrothermal synthesis has proven a particularly successful route to synthesising minerals, and indeed, all the materials studied in this thesis have naturally occuring analogues.

Due to the high temperature and pressures generated, and because the reaction is performed in one step in a sealed vessel, there are not many junctures at which the outcome of the reaction can be controlled. The most important element of design in hydrothermal syntheses is thus the choice of the spin source, bridging groups, and spacers. In Chapter 4, the combination of the T_d symmetric SO_4^{2-} group, the octahedral Ti^{3+} ion, and the K^+ spacer yields a low dimensional frustrated structure. Slight tweaking of the conditions gives the anhydrous analogue, which consists of $2D$ triangular planes (although the physics turn out to be one dimensional).

3.3 Experimental Techniques

Measuring classical long range order is usually rather straightforward – the order parameter, sublattice magnetization, is directly proportional to several experimentally measurable quantities. For example, ordering in a simple antiferromagnet is detectable by a kink in the magnetization at T_N, appearance of Bragg peaks at positions corresponding to the ordering wavevector in magnetic neutron scattering, and oscillations in muon spin relaxation (μSR). The order parameters of the quantum ground states discussed in Chapter 2 are more complicated, however, and often several experimental techniques must be applied to unambiguously assign a ground state. Some of the techniques in the toolbox of the experimental physicist and the pieces of the puzzle they can contribute are summarised in table 3.1.

Detailed discussion of experimental techniques in this work will be limited to neutron scattering techniques.

3.3.1 Neutron Scattering

One of the most powerful experimental techniques in modern solid state physics is neutron scattering, due to its exceptional [1] sensitivity to both atomic and magnetic structure and dynamics. While the formalism of neutron scattering is relatively straightforward, it is nonetheless somewhat lengthy to derive (and is besides well covered in [Squires (1978)], [Furrer *et al.* (2009)]). Therefore, only the basic results of the types of cross section which result, respectively, from nuclear, magnetic, spin incoherent, and isotope incoherent scattering from a crystalline solid will be given. The starting

---

[1]Though new X-ray techniques such as magnetic resonant X-ray scattering (MRXS) and resonant inelastic X-ray scattering (RIXS) are challenging this monopoly.

Technique	Measured Quantity	Extent	Timescale
Magnetization	$\langle M \rangle$	bulk	large
d.c. Susceptibility	χ	bulk	large
a.c. Susceptibility	$\chi'(\nu), \chi''(\nu)$	bulk	$\sim \nu$
Specific heat	$n(E)_{mag}$	bulk	large
NMR	χ_{loc}	local	$\mathcal{O}(10^{-6})$s
ESR	χ_{loc}	local	$\mathcal{O}(10^{-6})$s
μSR	M_{loc}	local	$\mathcal{O}(10^{-9})$s
Elastic neutron scatt.	$F(Q)$	bulk	$\mathcal{O}(10^{-12})$s
Inelastic neutron scatt.	$\chi''(Q)$	bulk	$\mathcal{O}(10^{-12})$s
MXRS	$F(Q)$	bulk	10^{-15} s
RIXS	Complex	bulk	10^{-15} s

Table 3.1: Some common modern measurement techniques. Only scattering techniques are able to yield spatially resolved quantities.

point, as usual, is Fermi's golden rule, which can be re-expressed as a neutron partial differential cross section as follows:

$$\frac{d^2\sigma}{d\Omega dE_f} = \frac{k_f}{k_i}\left(\frac{m}{2\pi\hbar^2}\right)^2 \sum_{\lambda_f,\sigma_f}\sum_{\lambda_i,\sigma_i} p_{\lambda_i}p_{\sigma_i} \left|\langle \mathbf{k}_f,\sigma_f,\lambda_f|\hat{U}(\mathbf{R})|\mathbf{k}_i,\sigma_i,\lambda_i\rangle\right|^2$$
$$\times \delta(\hbar\omega + E_{\lambda_i} - E_{\lambda_f}) \tag{3.1}$$

where $\mathbf{k}_i$ and $\mathbf{k}_f$ are the wavevectors of the incoming and outgoing neutron, respectively, σ_i and σ_f are the corresponding neutron spin states, and $\lambda_{i,f}$ represent the initial and final state of the system. $\hat{U}$ is the operator which describes the interaction between the neutron and the system. $\frac{d^2\sigma}{d\Omega dE_f}$ is the probability of scattering a neutron into a solid angle element Ω with an energy E_f. By replacing the δ-function with its integral form, and simplifying the matrix element, the above expression can be rewritten in a more convenient form:

$$\frac{d^2\sigma}{d\Omega d\omega} = \frac{k_f}{k_i}\left(\frac{m}{2\pi\hbar^2}\right)^2 \frac{1}{2\pi\hbar}\int dt\; e^{-i\omega t}\left\langle \hat{U}(\mathbf{k},0)\hat{U}(\mathbf{k},t)\right\rangle \tag{3.2}$$

We will now consider the types of cross section which result for the processes listed above.

3.3.1.1   Nuclear Scattering

Of the two types of scattering event commonly encountered in condensed matter, the first we will discuss is nuclear scattering. As this interaction is mediated by the weak nuclear force, which is much shorter in range than the neutron wavelength, the scattering potential may be approximated as originating from a point object:

$$\hat{U}(\mathbf{r}) = \frac{2\pi\hbar^2}{m} \sum_R b_R \delta(\mathbf{r} - \mathbf{R}_R) \tag{3.3}$$

where b_R is the nuclear scattering length (equivalent to the scattering power) and $\mathbf{R}_R$ is the position of the Rth atom. Rewriting this potential in Fourier space gives:

$$\hat{U}(\mathbf{q}) = \frac{2\pi\hbar^2}{m} \sum R b_R e^{-i\mathbf{q}\cdot\mathbf{R}} \tag{3.4}$$

Evaluating the matrix element then yields:

$$\left\langle \hat{U}(\mathbf{k},0)\hat{U}(\mathbf{k},t) \right\rangle = \left(\frac{2\pi\hbar^2}{m}\right)^2 \sum_{R,R'} b_R b_{R'} \left\langle e^{i\mathbf{k}\cdot(\mathbf{R}(t)-\mathbf{R}'(0))} \right\rangle \tag{3.5}$$

The amplitude of b_R is determined by both the internal structure of the nucleus and the orientation of the nuclear spin, and as a result varies greatly across the periodic table. Assuming a scattering system containing a large number of atoms of type β, the global variation of b_R can be expressed as a distribution $\sum f(b_R) = 1$, which reflects both the possible orientations of the nuclear spin and random population of isotopes of β. The mean of the distribution is then $\bar{b}_R = \sum b_R f(b_R)$. Recalling that the equation 3.5 applies to pairs of atoms, the scattering lengths $b_R b_{R'}$ are replaced with the mean $\overline{b_R b_{R'}}$ which is $(\bar{b})^2$ when $R \neq R'$ and $\overline{b^2}$ when $R = R'$. The sum may thus be broken into two components:

$$\sum_{R,R'} \overline{b_R b_{R'}} A_{R,R'} = \sum_{R\neq R'} (\bar{b})^2 A_{R,R'} + \sum_{R=R'} \overline{b^2} A_{R,R'}$$
$$= \sum_{R,R'} (\bar{b})^2 A_{R,R'} + \sum_R \overline{b^2} - (\bar{b})^2 A_{R,R'} \tag{3.6}$$

where $A_{R,R'} = \left\langle e^{i\mathbf{k}\cdot(\mathbf{R}(t)-\mathbf{R}'(0))} \right\rangle$. The first term in this equation, corresponding to scattering from different (and same) atoms at different times, is the **coherent** contribution to the cross section. It is this part which gives rise to interference effects which

can yield structural information. The second term, corresponding to scattering from the same atom at different times, is called the **incoherent** part, and does not contain any structural information. The coherent and incoherent cross sections are written out explicitly as follows:

$$\left(\frac{d\sigma}{d\Omega dE_f}\right)_{coh} = \frac{k_f}{k_i}\frac{1}{2\pi\hbar}\int dt\ e^{-i\omega t}\sum_{\mathbf{R},\mathbf{R}'}(\bar{b})^2\left\langle e^{i\mathbf{k}\cdot(\mathbf{R}(t)-\mathbf{R}'(0))}\right\rangle \qquad (3.7)$$

$$\left(\frac{d\sigma}{d\Omega dE_f}\right)_{inc} = \frac{k_f}{k_i}\frac{1}{2\pi\hbar}\int dt\ e^{-i\omega t}\sum_{\mathbf{R}}\left(\overline{b^2}-(\bar{b})^2\right)\left\langle e^{i\mathbf{k}\cdot(\mathbf{R}(t)-\mathbf{R}'(0))}\right\rangle \qquad (3.8)$$

3.3.1.2   Magnetic Scattering

The operator describing the interaction between a neutron and a magnetic field **H** is written:

$$\hat{U} = -\gamma\mu_N\hat{\sigma}\cdot\mathbf{H} \qquad (3.9)$$

where $\hat{\sigma}$ are the Pauli matrixes. In the case where the field is generated by an unpaired electron, **H** is written:

$$\mathbf{H} = \nabla\times\left(\frac{\mu_e\times\mathbf{R}}{|\mathbf{R}|^3}\right) - \frac{e\mathbf{v}_e\times\mathbf{R}}{c|\mathbf{R}|^3} \qquad (3.10)$$

where **R** is the distance between the electron and the point at which **H** is measured, and $\mu_e = 2\mu_B S$ is the electron spin operator. The two terms in the expression above represent the fields due to the spin and orbital angular momenta, respectively. Substituting this potential into the master equation for the partial differential scattering cross section, and assuming a spin-only contribution to **H**, the expression which results is:

$$\frac{d^2\sigma}{d\Omega dE'} = \frac{k_f}{k_i}N(\gamma r_0)^2\left|\frac{g}{2}f(\mathbf{Q})\right|^2\sum_{\alpha,\beta}(\delta_{\alpha\beta}-\hat{\mathbf{Q}}_\alpha\hat{\mathbf{Q}}_\beta)S^{\alpha\beta}(\mathbf{Q},\omega) \qquad (3.11)$$

where **Q** is the scattering vector, defined as the difference between the incoming and outgoing neutron wavevectors $\mathbf{k}_i - \mathbf{k}_f$. $f(Q)$ is the so-called form factor, and results from the Fourier transform of the real space spin-density distribution: the larger the spatial extent of the electron cloud, the more sharply $f(Q)$ drops off. For a d-block ion like Cu^{2+}, the scattering cross section is reduced to 50% of its $Q = 0$ value within $Q = 4$ Å^{-1}, whereas for a $4f$ element, where the orbitals are rather contracted, the form factor falls off more slowly, and the scattering is only halved at $Q \sim 8$ Å^{-1}. $\delta_{\alpha\beta}-\hat{\mathbf{Q}}_\alpha\hat{\mathbf{Q}}_\beta$ is the polarisation factor, which implies that neutrons can only couple to

the magnetization perpendicular to the the scattering vector $\mathbf{Q}$. Multiplying out the leading constants in the expressions for nuclear and magnetic scattering, it turns out that both are of the order r_0, implying that neutrons are approximately equally likely to scatter from a nucleus as from an electron. This highlights one advantage of neutron scattering over X-ray techniques, where the magnetic cross section is dwarfed by the structural by almost 5 orders of magnitude.

The physics of the system is contained within the scattering function (often also called the dynamical structure factor), $S(\mathbf{Q}, \omega)$, which contains the Fourier transform of the space and time dependent spin-spin correlation function:

$$S^{\alpha\beta}(\mathbf{Q}, \omega) = \frac{1}{2\pi\hbar} \int \sum_{\mathbf{R}, \mathbf{R}'} e^{i\omega t - i\mathbf{Q}\cdot(\mathbf{R} - \mathbf{R}')} \langle \mathbf{S}_{\mathbf{R}}^{\alpha}(t)\mathbf{S}_{\mathbf{R}'}^{\beta}(0) \rangle \qquad (3.12)$$

where $\mathbf{S}^{\alpha,\beta}$ are the $\alpha, \beta = x, y, z$ components of the spin operators at the positions $\mathbf{R}_{j,j'}$. Considering only the elastic scattering, that is, scattering arising at infinite time, the correlation function above reduces to the expectation values of the spin operators, $\langle S^{\alpha} \rangle$ and $\langle S^{\beta} \rangle$. For elastic scattering from a magnetically ordered system, the above expression is replaced by the elastic (sometimes also referred to as static) structure factor:

$$S^{z}(\tau) = \langle S^{z} \rangle f(\tau) \sum_{\mathbf{d}} \sigma_{\mathbf{d}} e^{i\tau \cdot \mathbf{d}} \qquad (3.13)$$

where $\mathbf{d}$ is a vector specifying the position of an atom in the unit cell and τ is a magnetic Bragg vector.

3.3.1.3 Powder Averaging

For many materials, it is impractical to grow crystals of a sufficient size for single crystal experiments. As a result, powder samples are often measured instead: the resulting powder averaged cross section is proportional to the spherical integral of $S(\mathbf{Q}, \omega)$, defined as follows:

$$S(Q, \omega) = \frac{1}{4\pi} \int d\psi \sin\theta d\theta S([Q\sin\theta\cos\psi, Q\sin\theta\sin\psi, Q\cos\theta], \omega) \qquad (3.14)$$

The above operation is not reversible (except in specific circumstances), and therefore usually entails a significant loss of information, particularly in the case of inelastic data, where scattering is distributed over a broad range of Q and ω.

3.3.2   Neutron Polarisation and xyz Polarisation Analysis

The presence of a polarisation dependent term in the magnetic cross section hints that the spin of the neutron can be used as yet another probe of the system under study, in addition to the neutron momentum and energy. To see what information can be extracted from it, it is necessary to revisit the polarisation dependence of the various cross sections shown above.

As the neutron is an $S = 1/2$ particle, its eigenstates may be represented in the usual manner: $|\uparrow\rangle$ and $|\downarrow\rangle$. Considering all the scattering processes discussed previously (nuclear, isotope incoherent, spin incoherent, and magnetic), and recalling the rule that the neutron is only sensitive to components of the magnetization, M, perpendicular to $\mathbf{Q}$, the matrix elements for spin flip and non-spin flip scattering events may be written down as follows:

$$\langle\uparrow|\hat{U}|\downarrow\rangle = B(I_x + iI_y) - \frac{\gamma_n r_0}{2\mu_B}(M_x + iM_y)$$

$$\langle\downarrow|\hat{U}|\uparrow\rangle = B(I_x - iI_y) - \frac{\gamma_n r_0}{2\mu_B}(M_x - iM_y) \tag{3.15}$$

$$\langle\uparrow|\hat{U}|\uparrow\rangle = \bar{b} + \frac{\gamma_n r_0}{2\mu_B}M_z - BI_z$$

$$\langle\downarrow|\hat{U}|\downarrow\rangle = \bar{b} - \frac{\gamma_n r_0}{2\mu_B}M_z + BI_z \tag{3.16}$$

where $B = \frac{b^\uparrow + b^\downarrow}{2I+1}$, $b^\uparrow$ and $b^\downarrow$ are the cross sections for scattering events when the neutron spin is respectively parallel or antiparallel to the nuclear spin, I is the nuclear spin, and $\bar{b}$ is the average nuclear scattering length. $M_{x,y}$ and M_z are the components of the magnetization perpendicular and parallel to the neutron spin direction, respectively [Stewart *et al.* (2009)],[Moon *et al.* (1969)].

Given a polarised beam and some means by which the spin flip and non spin flip contributions to the cross section can be analysed, the neutron spin can thus be used as a tool to separately probe different parts of the cross section. In the simple case of purely magnetic scattering, for example, analysis of the polarisation allows for separation of the scattering function, $S(\mathbf{Q}, \omega)$, into its longitudinal $[S^{zz}(\mathbf{Q}, \omega)]$ and transverse $[S^{xx}(\mathbf{Q}, \omega)$ and $S^{yy}(\mathbf{Q}, \omega)]$ components.

In the more complicated situation where scattering from more than one process enters the cross section, one way to completely separate all the contributions is three-directional (xyz) polarisation [Scharpf and Capellman (1993)] analysis. The experimental geometry required for application of this technique is shown in figure 3.2: the

incoming beam is polarised in three orthogonal directions, x, y and z, and scattered from the sample into a $2D$ detector lying in the xy plane. The angle formed between $\mathbf{Q}$ and the direction of the polarisation is called α, the Schärpf angle. Finally, for each polarisation, both spin-flip and non spin-flip cross sections are measured. The resulting 6 cross sections are written down as follows:

$$
\begin{aligned}
\left(\frac{d\sigma}{d\Omega}\right)_x^{nsf} &= \frac{1}{2}\sin^2\alpha\left(\frac{d\sigma}{d\Omega}\right)_{mag} + \frac{1}{3}\left(\frac{d\sigma}{d\Omega}\right)_{si} + \left(\frac{d\sigma}{d\Omega}\right)_{nuc} \\
\left(\frac{d\sigma}{d\Omega}\right)_x^{sf} &= (\cos^2\alpha+1)\left(\frac{d\sigma}{d\Omega}\right)_{mag} + \frac{2}{3}\left(\frac{d\sigma}{d\Omega}\right)_{si} \\
\left(\frac{d\sigma}{d\Omega}\right)_y^{nsf} &= \frac{1}{2}\cos^2\alpha\left(\frac{d\sigma}{d\Omega}\right)_{mag} + \frac{1}{3}\left(\frac{d\sigma}{d\Omega}\right)_{si} + \left(\frac{d\sigma}{d\Omega}\right)_{nuc} \\
\left(\frac{d\sigma}{d\Omega}\right)_y^{sf} &= (\sin^2\alpha+1)\left(\frac{d\sigma}{d\Omega}\right)_{mag} + \frac{2}{3}\left(\frac{d\sigma}{d\Omega}\right)_{si} \\
\left(\frac{d\sigma}{d\Omega}\right)_z^{nsf} &= \frac{1}{2}\left(\frac{d\sigma}{d\Omega}\right)_{mag} + \frac{1}{3}\left(\frac{d\sigma}{d\Omega}\right)_{si} + \left(\frac{d\sigma}{d\Omega}\right)_{nuc} \\
\left(\frac{d\sigma}{d\Omega}\right)_z^{sf} &= \frac{1}{2}\left(\frac{d\sigma}{d\Omega}\right)_{mag} + \frac{2}{3}\left(\frac{d\sigma}{d\Omega}\right)_{si}
\end{aligned} \tag{3.17}
$$

The magnetic, nuclear, and isotope/spin incoherent cross sections can thus be separated by rearranging the above system of equations. The magnetic cross section is written:

$$
\left(\frac{d\sigma}{d\Omega}\right)_{mag} = 2\left[\left(\frac{d\sigma}{d\Omega}\right)_x^{sf} + \left(\frac{d\sigma}{d\Omega}\right)_y^{sf} - 2\left(\frac{d\sigma}{d\Omega}\right)_z^{sf}\right] \tag{3.18}
$$

$$
\left(\frac{d\sigma}{d\Omega}\right)_{mag} = 2\left[\left(\frac{d\sigma}{d\Omega}\right)_x^{nsf} - \left(\frac{d\sigma}{d\Omega}\right)_y^{nsf} - 2\left(\frac{d\sigma}{d\Omega}\right)_z^{nsf}\right] \tag{3.19}
$$

The details of how to put this method into practice are given in the next section.

3.3.3 Neutron Instrumentation

An ideal neutron instrument would be able to probe both the atomic and magnetic statics and dynamics of a sample (whether powder or single crystal), over a large range in both Q and ω. In reality, of course, this is impossible, and therefore neutron instruments are usually specialised for a narrower range of applications. In condensed matter physics, the types of instruments used range from powder diffractometers and single crystal diffractometers for elastic scattering, to triple axis spectrometers and time of flight spectrometers for inelastic experiments.
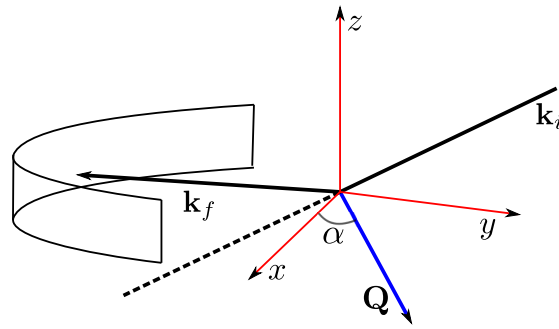
Figure 3.2: Scattering geometry for an xyz polarised experiment with a $2D$ detector array. The three orthogonal polarisations of the neutron beam used are indicated by the red arrows, α is the Schärpf angle.
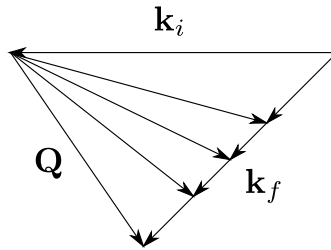

Figure 3.3: Scattering geometry for a direct geometry time of flight spectrometer.

The main techniques used in this thesis are inelastic time of flight spectroscopy and polarised diffuse scattering.

3.3.3.1   Inelastic Time of Flight Spectroscopy

Neutrons typically travel at velocities ranging between a few hundred to a few thousand ms^{-1}. Thus, given a flight path between the sample and the detector, L, on the order of a few meters, the energy of neutrons scattered from the sample can be resolved by counting the time they take to traverse L. Accomplishing this experimentally is far from trivial, however, for one simple reason: as neutrons are typically detected by an absorption process, they can not be detected both before and after they scatter from the sample. How then do we count their flight time? The solution is to pulse the beam, which fixes a well defined starting time for all the neutrons. This is achieved using a chopper, a rapidly rotating disc with small slots to periodically allow the passage of neutrons. Placing several choppers in series also allows for monochromatisation of the beam (although this can also be achieved by a conventional monochromator).

If a monochromatic (constant $\mathbf{k}_i$) beam is used, the time of flight experiment must be able to measure a broad range of wavevectors, $\mathbf{k}_f$, of the scattered neutrons (figure
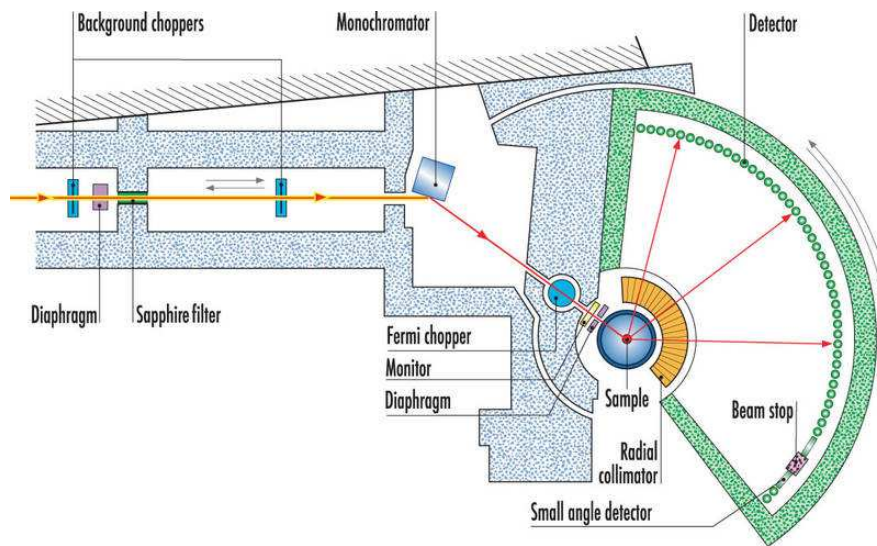
(a) An illustration of the IN4 spectrometer at the Institut Laue Langevin (ILL), Grenoble, France. The beam first passes through two background choppers, which eliminate fast neutrons and gamma rays. It is then monochromated by a crystal monochromator consisting of 55 pyrolitic graphite (PG) pieces, which also focus the beam on a spot of dimension 2×4 cm^2. Pulses of 10 μs to 50 μs are finally achieved using a Fermi chopper, rotating at up to 40000 rpm. The secondary spectrometer consists of a radial collimator to reduce background from the sample environment, and a detector array of ^{3}He tubes, covering scattering angles from $-6°$ to $120°$. There is an additional small angle position sensitive detector, not used for the experiment detailed in Chapter 5. Figure taken from http://www.ill.eu.
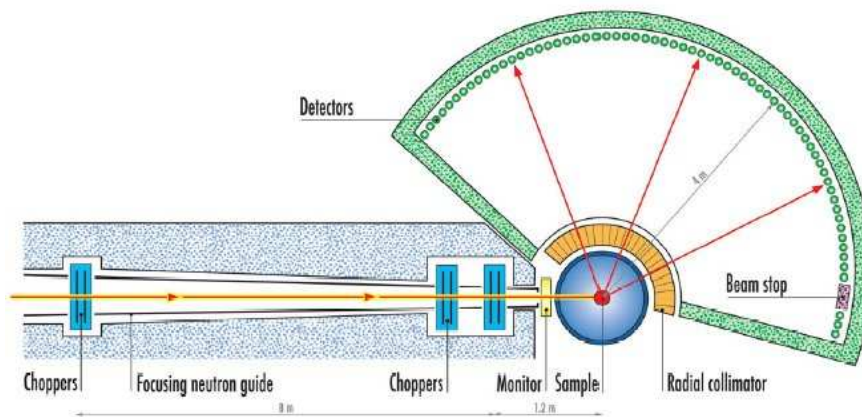
(b) The IN5 spectrometer at the ILL. The beam is pulsed and monochromated by a series of choppers. These also eliminate frame overlap, which occurs when two pulses are detected in the same timeframe. Beyond the sample position is a large evacuated box containing collimation and detectors. IN5 has one of the largest detector arrays among modern time of flight spectrometers, with 30 m^2 of ^{3}He filled position sensitive detectors (PSDs). Figure taken from http://www.ill.eu.

Figure 3.4

3.3). To this end, a large area detector array is thus usually employed. Combining the monochromator/choppers with such an array, and placing the sample in between, the result is a so-called direct geometry time of flight spectrometer. The three realizations of such an instrument used in this thesis are the IN4 and IN5 spectrometers at the ILL reactor source, and the MARI spectrometer on the ISIS pulsed source, the former two of which are shown in figure 3.4. Their main characteristics are summarised in table 3.2.

	IN4	IN5	MARI
Wavelength Range λ, [Å^{-1}]	2.2 Å- 3.6 Å PG(002) 1.1 Å- 1.8 Å PG(004) 0.85 Å- 1.5 Å Cu(220) (thermal)	1.8 Å- 20 Å (cold)	0.3 Å- 3 Å (thermal)
ω **Resolution** $\delta E_i/E_i$	$3-6\%$	$1-2\%$	$1-2\%$
Flux on Sample n cm^{-2} s^{-1}	$\sim 5 \times 10^5$	$\sim 1 \times 10^6$ (at 5 Å)	$\sim 2 \times 10^3$ (at 1 Å)
Detectors	$\sim -3° - 120°$ ^{3}He tubes PSD (small $\angle$)	$-12° - 135°$ ^{3}He PSD (30 m^2)	$3° - 134°$ ^{3}He tubes

Table 3.2: Main characteristics of the time of flight neutron scattering instruments used in this work. The ω resolution is given as the Gaussian FWHM versus incident energy, and is determined by the speed of the choppers, their precision, and the time resolution of the electronics.

3.3.3.2   Polarised Diffuse Scattering

In order to put the principles of xyz polarisation analysis into practice, several things are needed: a highly polarised neutron beam, a device capable of flipping its polarisation to an arbitrary direction, and, finally, a means by which the polarisation can be measured. The former is provided by either a polarising filter, such as a ^{3}He cell, a supermirror, or a polarising crystal, typically a Heusler alloy. The polarisation of the beam produced by these is typically in the range of 70% for ^{3}He spin filters to in excess of 90% for a supermirror. This is preserved by using a guide field throughout

The second component, the spin flipper, must be able to adiabatically flip the beam polarisation to an arbitrary direction with respect to the guide field. This can be
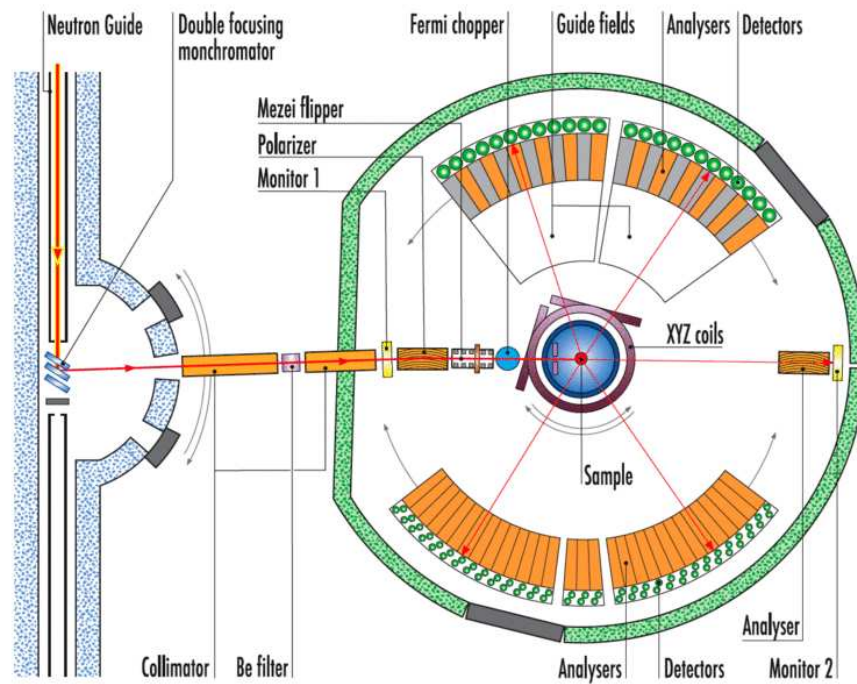
Figure 3.5: The D7 instrument at the ILL. The neutrons are monochromated by a double focusing graphite monochromator, then polarised by a Schärpf bender supermirror. The beam is flipped into the required polarisation by a Mezei flipper. After scattering from the sample, the neutrons are analysed using a set of supermirror analysers, and finally detected in the $2D$ detector array, which covers nearly $150°$ in scattering angle (though slightly less at the time of the experiments detailed in Chapter 5). Figure taken from http://www.ill.eu.

achieved using a so-called Mezei coil, a rectangular solenoid oriented at the desired angle with respect to the guide field. Finally, the analysis of the outgoing beam after scattering is performed by a supermirror, a multilayer of Ni and Co which reflects only neutrons of a single polarisation.

The particular realisation of the polarised scattering experiment used during this thesis is the $D7$ instrument operating on the high flux reactor at the Institut Laue Langevin in Grenoble, France. It is one of only two such instruments worldwide (the other being the DNS spectrometer located at FRMII in Germany). A schematic of its layout is given in figure 3.5.

Chapter 4

Frustrated Low-Dimensional Magnetism in Ti^{3+} Alums

In the quest for low dimensional, frustrated quantum magnets, the Ti^{3+} ion (d^1) has historically been somewhat overlooked as a source of $S = 1/2$ spins. This is partly due to its tendency to oxidise to Ti^{4+}, which is a complicating factor in synthesis. Under hydrothermal conditions, this issue can be dealt with by regulating the pH of the solution, which in this work has produced one new material, the potassium alum KTi(SO$_4$)$_2$·H$_2$O, and an improved synthesis of its anhydrous analogue KTi(SO$_4$)$_2$. This chapter will show that KTi(SO$_4$)$_2$·H$_2$O is a realisation of the famous $J_1 - J_2$ Heisenberg chain model, and fits to magnetic susceptibility and specific heat data reveal that it may be one of the first compounds in the dimerised regime of the phase diagram defined by $0.2411 < J_2/J_1 < 1.8$. Its anhydrous relative KTi(SO$_4$)$_2$, on the other hand, is shown to be well described by a Heisenberg chain model with frustrated interchain interactions. The details of the local crystal field are found to be crucial in determining the magnetic properties of both.

4.1   Ti^{3+} as a Source of $S = 1/2$

Browsing through the literature on $S = 1/2$ model magnets, it is impossible not to notice that by far the most common source of spin is the Cu^{2+} ion. The reasons for this are manyfold: the availability of a broad range of starting materials, the relative stability of Cu^{2+} in a variety of chemical environments, the quenched orbital moment in a cubic crystal field (resulting in Heisenberg spins), and finally the Jahn-Teller in-

stability, which can reduce the dimensionality of the magnetic lattice. In other words, Cu^{2+} based systems are both easy to make and relatively simple in terms of their single ion physics. As a result, however, other sources of $S = 1/2$ have remained rather underexplored. The Ti^{3+} ion is seemingly the simplest among these, possessing only 1 d electron, but yields surprisingly rich single ion physics (as we shall see).

In a cubic crystal field, the ^2D free ion term of the Ti^{3+} ion is split into a low lying triplet of t_{2g} states, consisting of the d_{xy}, d_{xz} and d_{yz} orbitals, separated from the upper e_g doublet ($d_{x^2-y^2}$ and d_{z^2}) by a gap Δ_o proportional to the magnitude of the crystal field. The lone d electron occupies the lower lying set of t_{2g} orbitals, resulting in a triply degenerate ^2T orbital ground state. One consequence of the remaining degeneracy in the ground state, as discussed in Chapter 2, is that the orbital angular momentum is not entirely quenched, and can be represented using a p orbital basis with the signs reversed. In the absence of any further perturbations, the ground state is thus a Kramers doublet with both $\langle L \rangle = 0$ and $\langle S \rangle = 0$.

This contradicts experimental observations, which indicate that the Ti^{3+} ion usually has a finite (albeit often strongly reduced and anisotropic) moment. To explain this, perturbations beyond the cubic crystal field must be considered. Some logical candidates for these include both lower symmetry crystal fields and Jahn Teller coupling.

Taking the simplest case and considering only the influence of a tetragonal field of magnitude Δ_{tet}, the single ion Hamiltonian can be diagonalised to yield the dependence of the $g-$tensor on Δ_{tet}. For positive sign of Δ_{tet}, that is, favouring a slight compression of the octahedron along a C_4 axis, the degeneracy of the t_{2g} levels is broken, and the ground state is an orbital singlet with $L = 0$. This is reflected in the powder averaged $g_{av} = (g_\perp + 2g_{||})/3$ increasing rapidly with increasing Δ_{tet} as the LS coupling becomes less efficient at mixing in higher lying orbital states. For the opposite sign, that is, when the octahedron is elongated along the C_4 axis, the orbital ground state is a nonmagnetic doublet, as in the unperturbed case (figure 4.2).

An early experimental example of the d^1 ion in the presence of low symmetry fields is the series of doped alums of formula $A[Al:Ti](SO_4)_2 \cdot 12H_2O$, where A is an alkali metal cation. These materials were widely studied from the early 1930's and onwards as models for the then fledgling crystal field theory, and were chosen due to their isolated metal polyhedra. A key finding of this work, represented in table 4.1, is the variation of the g-tensor with the magnitude of the small orthorhombic component (see figure 4.1) of the crystal field [Dionne and MacKinno (1968)] – the larger this component, the smaller the reduction of and asymmetry in g.
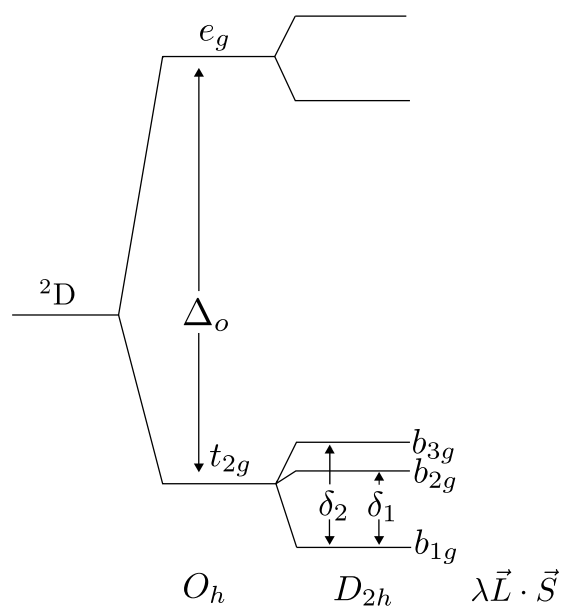
Figure 4.1: Energy level structure of Ti^{3+} in an orthorhombic crystal field.
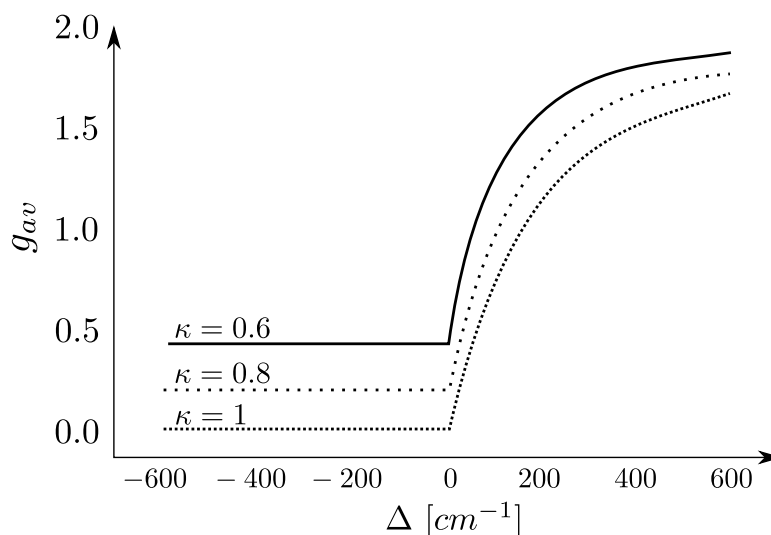
Figure 4.2: Variation of the $g-$factor with distortion in a trigonal field assuming $\lambda = 200$cm^{-1} (slightly greater than the experimentally measured $\lambda \sim 150$ cm^{-1} for Ti^{3+}).

Alum	g_x	g_y	g_z	δ_1 (cm^{-1})	δ_2 (cm^{-1})
CsTi(SO$_4$)$_2$ · 12H$_2$O	1.25	1.14	1.14	?	?
Cs[Al:Ti](SO$_4$)$_2$ · 12H$_2$O	1.241	0.931	0.931	-500	-500
Rb[Al:Ti](SO$_4$)$_2$ · 12H$_2$O	1.895	1.715	1.767	1070	1310
Tl[Al:Ti](SO$_4$)$_2$ · 12H$_2$O	1.938	1.790	1.834	1462	1483
K[Al:Ti](SO$_4$)$_2$ · 12H$_2$O	1.875	1.828	1.897	1780	2947

Table 4.1: g-tensor and crystal field splittings for a range of pure and doped Ti-based alums.

In the following two sections of this chapter, we will discuss two materials, which belong to the more general family of alums, of general formula $AB(SO_4)_2.xH_2O$. The first, $KTi(SO_4)_2.H_2O$ ($x = 1$) has been prepared for the first time using a hydrothermal method, and characterised by a variety of techniques which show it to be a new realisation of the frustrated Heisenberg chain model in the dimerised regime of the phase diagram [Nilsen *et al.* (2008)]. Its anhydrous analogue, $KTi(SO_4)_2$ ($x = 0$), is the subject of the second part of the chapter. Despite initial expectations that $KTi(SO_4)_2$ was a realisation of the $S = 1/2$ anisotropic triangular lattice antiferromagnet, neutron scattering and other studies shows the physics to be describable as quasi one dimensional.

4.2 $KTi(SO_4)_2(H_2O)$, a New Realisation of the Frustrated Chain Model

4.2.1   Synthesis and Crystal Structure

The combination of a monovalent cation, A, a trivalent d-block ion, B, and the tetrahedral SO_4^{2-} ion in hydrothermal conditions has produced a range of frustrated materials in the past, including the jarosite family $AB_3(SO_4)_2(OH)_6$ of kagome antiferromagnets [Wills (1996)]. The T_d symmetry of the SO_4^{2-} group naturally leads to frustrated connectivities, and the presence of a counterion in the form of A^+ often leads to reduced dimensionality.

$KTi(SO_4)_2 \cdot (H_2O)$ was first prepared in an exploration of the A=K, B=Ti system. K_2SO_4, $Ti_2(SO_4)_3$, and H_2SO_4 were combined in the molar ratio 2 : 7 : 15 under stirring in aqueous solution. The mixture was placed inside a PTFE lined bomb, which was then heated to 155°C for 48 hours. It was then cooled slowly (10 K h^{-1}) to room temperature, yielding small (~ 0.1mm^3) bluish purple crystals of average size 0.1 mm^3, in addition to large quantities of amorphous impurity. Subsequent optimisation of the synthesis identified glass as a superior surface for crystal nucleation, resulting in less of the impurity phase, and higher reliability of product formation. Despite these attempts, the synthesis remains unpredictable, with a total number of only 7 successes in approximately 140 attempts, suggesting that $KTi(SO_4)_2 \cdot (H_2O)$may be a metastable phase. Further details on the synthesis are given in Appendix A.

A crystal of dimensions $0.19 \times 0.15 \times 0.08$ mm^3 was selected for single-crystal diffraction (details of the refinement and crystal structure are also found in Appendix A). $KTi(SO_4)_2 \cdot (H_2O)$ was thus found to crystallize in the monoclinic P2$_1$/m space group,

Atoms	Length	Atoms	Angle
Ti–O(1)	2.051(4) Å	O(1)-Ti-O(2)	175.3(1)°
Ti–O(2)	2.029(5) Å	O(2)-Ti-O(3)	91.9(1)°
Ti–O(3)	1.999(3) Å	O(3)-Ti-O(3)	88.0(1)°
Ti–O(4)	2.054(3) Å	O(4)-Ti-O(4)	90.5(1)°
Ti–Ti(H)	5.256(4) Å		
Ti–Ti(D)	4.928(2) Å		

Table 4.2: Selected bond lengths and angles for $KTi(SO_4)_2 \cdot (H_2O)$. H and D indicate horizontal (along the b direction) and diagonal distances within the frustrated ladders, respectively (see also figure 4.3).

with lattice parameters $a = 7.6492(3)$ Å, $b = 5.2580(2)$ Å, $c = 9.0485(3)$ Å, and $\beta = 101.742(2)°$. The structure is isomorphous with that of the naturally occurring mineral Krausite ($KFe(SO_4)_2 \cdot H_2O$) [Graeber *et al.* (1965)] and consists of double chains of Ti octahedra, connected by SO_4^{2-} groups along the b axis (figure 4.3). The pairs of chains are separated in the a direction by K^+ ions and in the c direction by interpenetrating H_2O molecules bound to apices of the octahedra (figure 4.4). The magnetic ions are connected in an edge sharing triangular motif, with diagonal separations of 4.93Å and horizontal separations of 5.26Å. Superexchange is expected to be mediated by the SO_4^{2-} groups, which doubly bridge both nearest and next-nearest neighbor pairs of magnetic ions. The distances between the chains in the a and c directions are 7.60Å and 5.87Å, respectively, suggesting that any magnetic exchange in $KTi(SO_4)_2 \cdot (H_2O)$ should be essentially confined to the chains.

Locally, the TiO_6 octahedra are slightly triclinically distorted, with bond lengths and angles as shown in table 4.2 and figure 4.5. Assignment of the magnetically active orbital is not straightforward from geometrical considerations.

4.2.2   Magnetic Susceptibility

Magnetic susceptibility measurements were carried out on $KTi(SO_4)_2 \cdot (H_2O)$down to 1.8K in fields ranging from 0.01 T to 5 T on a polycrystalline sample of $KTi(SO_4)_2 \cdot (H_2O)$ using a Quantum Design MPMS$_2$ SQUID magnetometer. As there was no strong field dependence in the range measured, only the 0.01 T data are shown in figure 4.6.

At high temperature ($> 50K$), the curve is well described by the usual Curie-Weiss expression $\chi = C/(T - \theta)$, where C is the Curie constant, $\sim \mu_{eff}^2/8$ in *c.g.s.* units, and θ is the Weiss constant. Values of $\mu_{eff} = 1.557(3)\mu_B$ (i.e. $g_{eff} = 1.80$) and
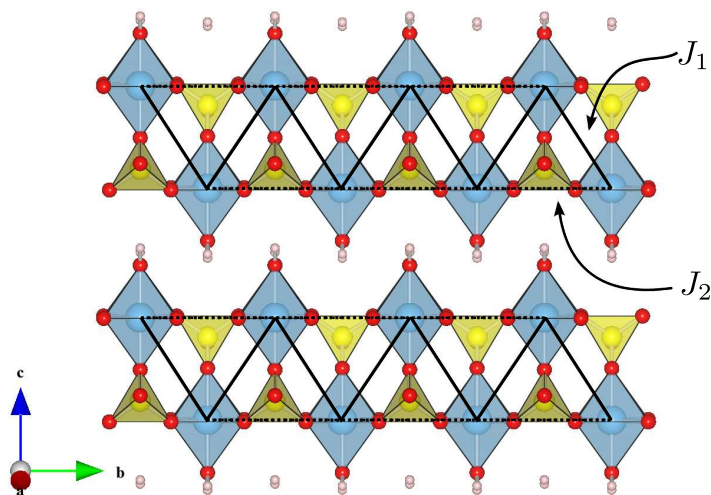
Figure 4.3: The crystal structure of $KTi(SO_4)_2 \cdot (H_2O)$ viewed approximately along the a direction. The TiO_6 octahedra are indicated in blue, SO_4 tetrahedra in yellow, and O^{2-} and H atoms in red and pink, respectively. K^+ ions have been left out for clarity. The double chains of SO_4-bridged TiO_6 octahedra described in the text run along the b direction, and are separated along the c direction by the apical water molecules of the TiO_6 octahedra. The frustrated chain lattice is superimposed on the crystal structure, with J_1 and J_2 represented by solid and dotted lines, respectively.
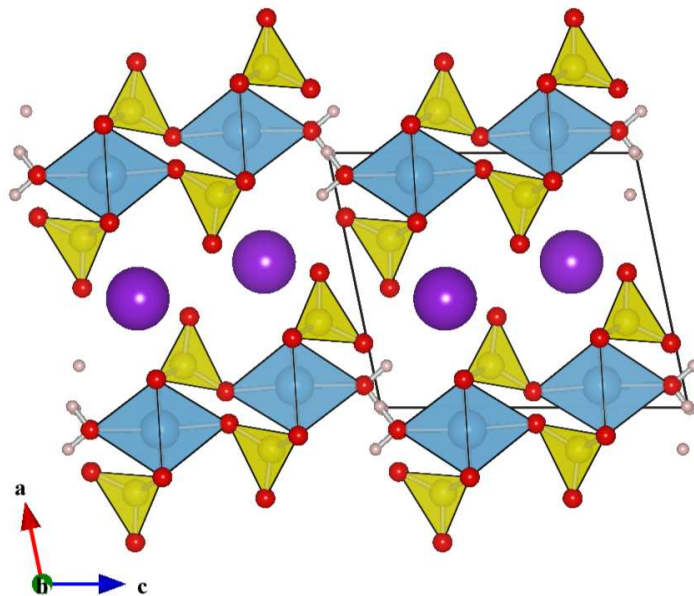
Figure 4.4: The crystal structure of $KTi(SO_4)_2 \cdot (H_2O)$ viewed along the $b-$axis. The chains are separated by K+ along the a direction.
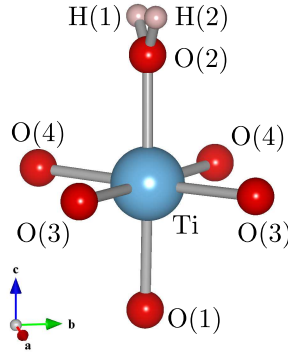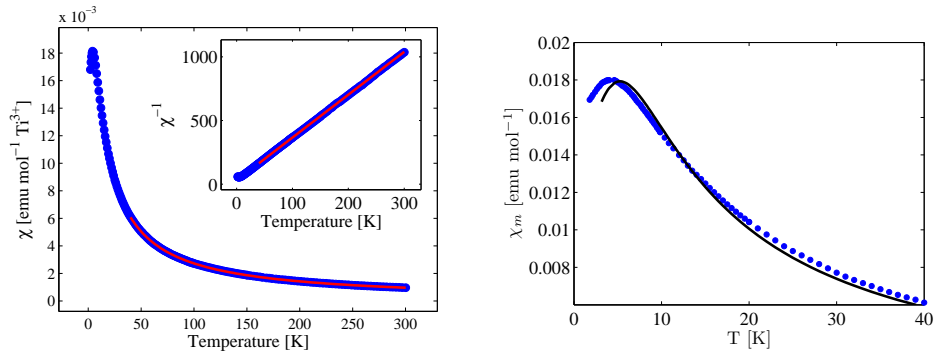
Figure 4.5: The TiO$_6$ octahedron.

Figure 4.6: (left) The molar magnetic susceptibility of KTi(SO$_4$)$_2$·(H$_2$O) with Curie-Weiss fit indicated in red. (right) The low temperature part of χ_m, showing the broad bump at 4.5 K. An attempted fit to the $S = 1/2$ Heisenberg chain model shows that the peak can not be described within the confines of this model.

$\theta = -9.8(7)$K, (i.e. weak antiferromagnetic coupling) were found. The presence of amorphous impurity, which contains diamagnetic Ti^{4+}, means that the value for μ_{eff} should be treated as a lower bound.

When the temperature is lowered, a broad maximum in the susceptibility characteristic of short-range correlations along the magnetic chains is observed around $T = 4.5$K. No signs of long-range ordering are observed down to the lowest temperature, confirming that the interchain coupling is weak. Assuming either the horizontal or diagonal coupling (see figure 4.3) is dominant, the simplest possible microscopic model to describe the system is the antiferromagnetic $S = 1/2$ Heisenberg chain (QHC), given by the Hamiltonian:

$$\mathcal{H} = J \sum_{i,i+1} \mathbf{S}_i \cdot \mathbf{S}_{i+1} \tag{4.1}$$

Clearly, from the fit (figure 4.6), the $1D$ chain cannot reproduce either the peak position or shape, highlighting the probable influence of the other exchange. The Hamiltonian which results upon its inclusion is:

$$\mathcal{H} = J_1 \sum_n^N \mathbf{S}_n \cdot \mathbf{S}_{n+1} + J_2 \sum_n^N \mathbf{S}_n \cdot \mathbf{S}_{n+2} \qquad (4.2)$$

where J_1 and J_2 are the antiferromagnetic nearest neighbour and next-nearest neighbour exchange parameters (see figure 4.3), respectively, and $\alpha = J_2/J_1$ may be defined as a measure of the frustration. This model is known by a number of names, including the zigzag chain model, the nearest neighbour chain model, and the frustrated chain model (FCM). Henceforth, we shall use the last convention.

4.2.3   Phase Diagram of the Frustrated Chain Model

$$\boxed{D = 1,\ z = 4,\ S = 1/2,\ \text{frustrated}}$$

One of the few Heisenberg models for which an exact solution exists is the Majumdar-Ghosh chain [Majumdar and Ghosh (1969a)],[Majumdar and Ghosh (1969b)]. This is a special case of the FCM with frustration parameter $\alpha = J_2/J_1 = 1/2$. The two degenerate VBC ground states of this model correspond to dimer coverings of the lattice, and can be represented as follows:

$$|\Psi\rangle_1 = \ldots \otimes |2,3\rangle \otimes |4,5\rangle \ldots \otimes |n, n+1\rangle \qquad (4.3)$$

$$|\Psi\rangle_2 = \ldots \otimes |1,2\rangle \otimes |3,4\rangle \ldots \otimes |n-1, n\rangle \qquad (4.4)$$

where $|n, n+1\rangle$ denotes a dimer on a nearest neighbour bond. The correlation function in this state is extremely short ranged, with $\langle S_i \cdot S_j \rangle = 0$ for $j > i+1$, and the gap from the ground state to the first excited triplet is $\Delta = J/10$ [White and Affleck (1996)].

When α is reduced from $\alpha_{MG} = 1/2$, the system remains spontaneously dimerised down to a critical $\alpha_c = 0.2411$ [Haldane (1982)],[Okamoto and Nomura (1992)], with the gap decreasing exponentially before vanishing at α_c. The ground state is no longer exact, however, and the ζ increases rapidly. Below α_c the ground state is an algebraic spin liquid, as for the unfrustrated $1D$ chain.

If α is increased beyond α_{MG}, the gap first reaches a maximum at $\alpha \sim 0.6$ [White and Affleck (1996)], before slowly decreasing and vanishing at $\alpha \sim 4$ [Kumar *et al.* (2010)]. Simultaneously, the correlation length increases from $\zeta \sim r_{nn}$ and the correlations
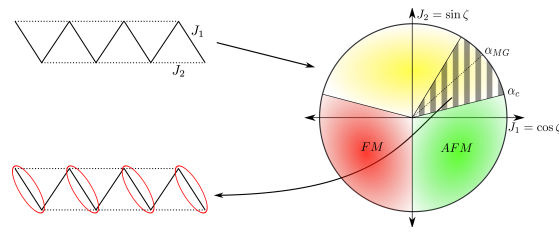
Figure 4.7: The zero temperature phase diagram of the FCM using the angular parametrisation indicated on the axis labels. $\alpha = \tan\zeta$. The yellow region indicates the frustrated part of the phase diagram, which has the substructure described in the text.

become incommensurate [Somma and Aligia (2001)], as expected from the classical model, which posesses a spiral ground state in this region of the phase diagram. The incommensurate spiral state persists as the sign of J_1 is changed from AFM to FM. A number of experimental realisations exist in this quadrant of the phase diagram, compared to only two, CuGeO$_3$, with $\alpha = 0.4$ [Hase *et al.* (1993)], and (N$_2$H$_5$)CuCl$_3$, with $\alpha = 0.25$ [Hagiwara *et al.* (2001)],[Maeshima *et al.* (2003)], in the AFM-AFM quadrant of the zero temperature phase diagram 4.7.

4.2.4 Specific Heat and Numerics

To complement the magnetic susceptibility data, specific heat was measured in the temperature range 480mK to 300K. The data again show a broad feature at around $T = 3$K (figure 4.8) corresponding to the point at which the maximum overlap between buildup of short-range correlations (and hence the magnetic density of states) and thermal population of available states is achieved. Also, as in the magnetic susceptibility, no anomalies or other indications of long-range order are observed down to the lowest measured temperature. The full curve was fitted for $T < 50$K using the expression $C_{p,tot} = C_{p,mag} + C_{p,phonon}$, where $C_{p,mag}$ is the magnetic specific heat of the chains, and $C_{p,phonon}$ was approximated using a power series in odd powers of T up to order T^7. Again, the $S = 1/2$ Heisenberg chain curve fails to capture the main features of the peak.

Because no analytical expression exists for the thermodynamic quantities of the FCM, numerical approaches must be called on to fit the experimental curves. Two approaches were chosen: a 10th order high temperature series expansion (HTSE) supplemented by Padé approximants [Buhler *et al.* (2000)], and exact diagonalisations (ED) of finite

chains. For the former approach, the themodynamic quantities are written as follows:

$$\chi = \frac{1}{T}\sum_{n,k} a_{n,k}\alpha^k(\beta J)^n \qquad (4.5)$$

$$C_{p,mag} = \sum_{n,k} a_{n,k}\alpha^k(\beta J)^n \qquad (4.6)$$

where $\beta = 1/T$ and the expansion coefficients $a_{n,k}$ are summarised in [Buhler *et al.* (2000)],[Buhler *et al.* (2001)]. The region of validity of the expansion was extended in T to approximately $J/5$ by calculation of the Padé approximants up to the $[5,5]$ approximant using a numerical quotient-difference algorithm continued fraction method [McCabe (1983)]. Exact diagonalisation was performed for chain lengths up to $N = 18$ with periodic boundary conditions using the ALPS libraries [Albuquerque *et al.* (2007)]. Thermodynamic quantities were obtained from the *fulldiag_evaluate* program. The fits of the experimental data to the calculated χ and C_p curves are shown in figure 4.8. Excellent correspondence between experiment and calculation is found for two sets of parameters, summarised in the following tables:

Small α				
	α	J_1 [K]	J_2 [K]	g_{av}
ED	0.29(2)	9.5(1)	2.8(1)	1.80(1)
HTSE+[5,5] Padé	0.29(2)	9.5(1)	2.8(1)	1.80(1)

Large α				
	α	J_1 [K]	J_2 [K]	g_{av}
ED	1.48(2)	5.4(2)	8.0(2)	1.80(1)
HTSE+[5,5] Padé	1.46(2)	5.4(2)	7.9(2)	1.80(1)

Both of the above solutions imply that J_1 and J_2 are antiferromagnetic, and furthermore that the system is to be found in the gapped, dimerised region of the phase diagram. While the behaviour at $T \sim \mathcal{O}(J)$ for the two models are similar, the gaps of the two states, as implied above, differ. Based on density matrix renormalisation group (DMRG) calculations by White *et. al.* [White and Affleck (1996)], a vanishing gap $< J/20$ is implied for the former, whilst the latter possesses a large gap of approximate magnitude $J_1/5 \sim 1$ K. In the T range measured, it is however difficult to distinguish between the two, as $\Delta < T_{min} = 1.8$ K for both scenarios. No clear anomalies are seen in the C_p measurements, which extend to lower temperatures $T_{min} = 0.35$ K, implying a gap, but this should not be taken as conclusive evidence of $\alpha < 1$.
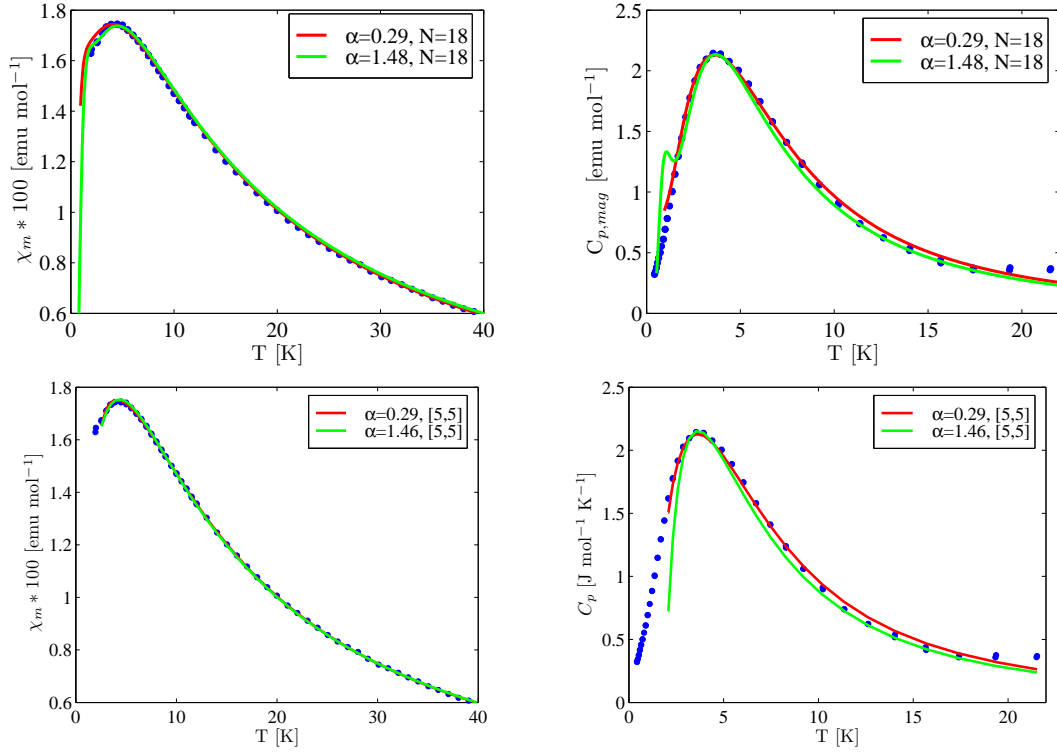
Figure 4.8: (top) The magnetic susceptibility (left) and magnetic specific heat (right) of $KTi(SO_4)_2 \cdot (H_2O)$, measured down to 1.8 K and 350 mK, respectively. The ED results for large and small α solutions are indicated by solid lines. The maximum temperatures shown for χ and C_p correspond to approximately 4θ and 2θ, respectively. The small bump observed at ~ 1 K in the C_p data for large α is a finite size effect. (below) HTSE+Padé approximant results, as above. The rapid drop at low T in the large α fit to C_p, indicates an overestimation of the spin gap, Δ, in the HTSE.

4.2.5 Electronic Structure

In order to help distinguish between the two scenarios proposed above, as well as to gain insight into the mechanism involved in the selection of the active orbital, $ab-initio$ calculations using the local density approximation (LDA), LDA with an on-site repulsion term, U, (L(S)DA+U), and tight binding models were performed by D. Kasinathan and H. Rosner.

The non-magnetic part of the band structure for $U = 0$ (i.e. neglecting correlations) is shown in figure 4.9: the lowest lying band belongs to the d_{xz} orbital, and is separated from the d_{xy} and d_{yz} bands by gaps of approximately 0.15 eV and 0.25 eV, respectively. Due to the small size of the gap, it is not straightforward to unambiguously determine the magnetically active orbital without also considering the effect of correlations.
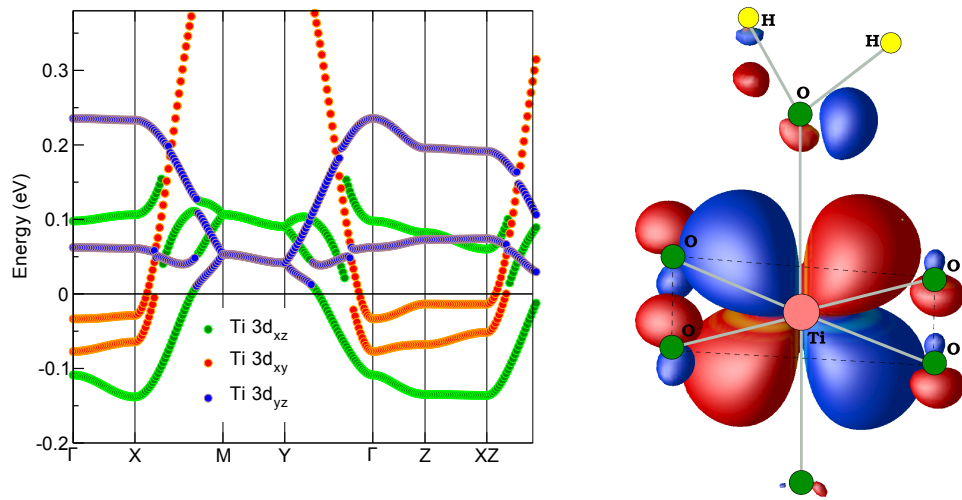
Figure 4.9: (left) The electronic band structure states of KTi(SO$_4$)$_2$·(H$_2$O) calculated in the local density approximation. The bands disperse along the $\Gamma - Y$ and $X - M$ directions in the Brillouin zone, corresponding to the direction of the chains in the crystal structure. The gaps between the centre of lowest lying d_{xz} band and the centers of the d_{xy} and d_{yz} bands are about 0.15 eV and 0.25 eV. The double lines represent the upper and lower bounds of the band. The metallic solution is an artefact of the LDA method. Figure courtesy of D. Kasinathan. (right) The Wannier function of the ground state d_{xz} orbital. The ab plane is highlighted by a dotted grey line, whilst the TiO$_6$ octahedron is indicated by solid lines. When the hopping integrals resulting from this orbital arrangement are mapped onto a Heisenberg model, $J_2 > J_1$, thus apparently favouring the large α scenario.

The $U > 0$ problem was treated by two different methods: In the first, a tight binding model was constructed for each t_{2g} orbital using the bands calculated in LDA. Solving this model for the hopping integrals t, and effective on-site repulsions, U_{eff}, then mapping onto a Heisenberg model using $J^{TB} = 4t^2/U_{eff}$, it was found that an occupied d_{xy} orbital would give an $\alpha = 2.78$, far greater than either of the scenarios proposed in the previous section. Furthermore, the calculated J's are almost two orders of magnitude larger than the experimental values. The same calculation for the d_{xz} and d_{yz} orbital yields more reasonable α values of 0.38 and 0.57, roughly consistent with the low α scenario, as well as plausible J values of $J_1 = 31$ K, $J_2 = 11.8$ K, and $J_1 = 19$ K, $J_2 = 11$ K, respectively.

The second approach, involving an extension of the LDA calculation to include U and spin, also point towards d_{xz} being the magnetically active orbital. Populating each band with only up spins, the energy cost is 350 meV higher for the d_{yz} orbital versus the d_{xz} and much higher for the d_{yz}, implying that the that d_{xz} has the lowest magnetic energy in the ground state. The calculated value of α for d_{xz} is found to be greater than one for all physically plausible values of U, supporting the large α scenario.

4.2.6 What is the Gap?

The electronic structure calculations appear to favour the large α solution of the two possibilities proposed above. To confirm this, we performed additional ac susceptibility measurements on KTi(SO$_4$)$_2$·(H$_2$O) in the temperature range 100 mK to 1.5 K, with the aim of observing gap, Δ. All measurements were carried out with an excitation field of 1000 Hz. In the absence of an applied magnetic field, the real component of the susceptibility, χ', is found to almost vanish as T approaches zero, with only a small upturn from $S = 1/2$ paramagnetic defects remaining (figure 4.10).

This component complicates the analysis of the data, and thus the $H = 0.3$ T temperature scan, where the paramagnetic component is saturated, is selected for further analysis. Below a kink at $T_k = 0.65$ K, the curve is found to follow an exponential decay, consistent with the opening of a gap of magnitude $\Delta = 1.05(5)K$. The magnetic field dependence of $M = \int \chi' dH$ at 90 mK tells a similar story (4.10): as field is applied, there is a small initial rise which can be ascribed to saturation of the defect contribution. This is followed by a rapid increase of M at $H \sim 0.8$ T, caused by a crossover into a magnetic state. The gap obtained by linear extrapolation of the critical field, $H_c = 0.9$, is $\Delta = g\mu_B SH_c = 1.0(1)$ K, with $g = 1.9$. This is consistent with that determined from the temperature scans. Interestingly, T_k remains nearly constant
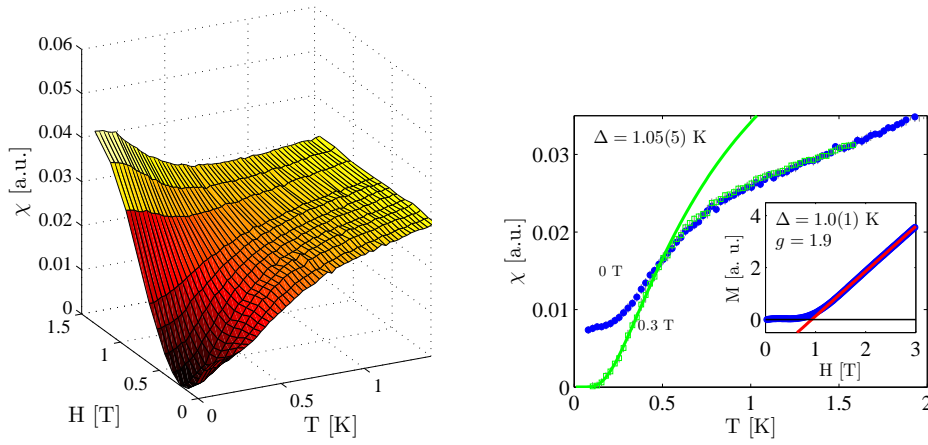
Figure 4.10: (left) Scans of the real component of the susceptibility, χ', versus T measured at multiple applied fields between $H = 0$ T and $H = 1.5$ T. (right) Scans of χ' versus T measured at fields of $H = 0$ T and $H = 0.3$ T. The curves exhibit a kink at approximately $T_k = 0.65$ K with a subsequent exponential decay of χ' as $T \to 0$. The higher value of χ' at low temperatures for the $H = 0$ T curve is due to the presence of paramagnetic defects, which are saturated at $H = 0.3$ T. The gap extracted from an exponential fit to the low T part of the curve is $\Delta = 1.05(5)$ K. (inset) An H scan of $M = \int \chi' dH$ measured at 90 mK. The gap is estimated to be approximately 1 K from a linear extrapolation of M at $H > g\mu_b SH_c s$.

until its disappearance at 0.8 T.

The gap value $\Delta \sim J_1/5 = 1.05(5)$ K almost exactly corresponds to the prediction from the DMRG results of White and Affleck [White and Affleck (1996)] for large α, namely $\Delta = J_1/5 = 1.1$ K. More recently, another suggestion on the size of Δ was produced by a modified DMRG approach [Kumar *et al.* (2010)]. An exponential fit to the α dependence of Δ yields the following:

$$\Delta/J_2 = 3e^{-2.94/\alpha^{-2/3}} \tag{4.7}$$

Entering $J_2 = 8.0$ K into this expression, an approximate $\Delta = 0.06J_2 = 0.5$ K is extracted. While too small by a factor of two compared with the experimentally measured Δ, agreement is nonetheless still better for the large α scenario.

A third independent verification of the validity of the large α solution was achieved by performing high field magnetisation measurements at the Dresden High Magnetic Field Laboratory – these experiments were carried out by A. Tsirlin and D. Kasinathan. The magnetisation isotherm measured at 1.8 K in pulsed fields up to 22 T is shown in figure 4.11. Again, comparison of ED results for the two with experiment yield excellent
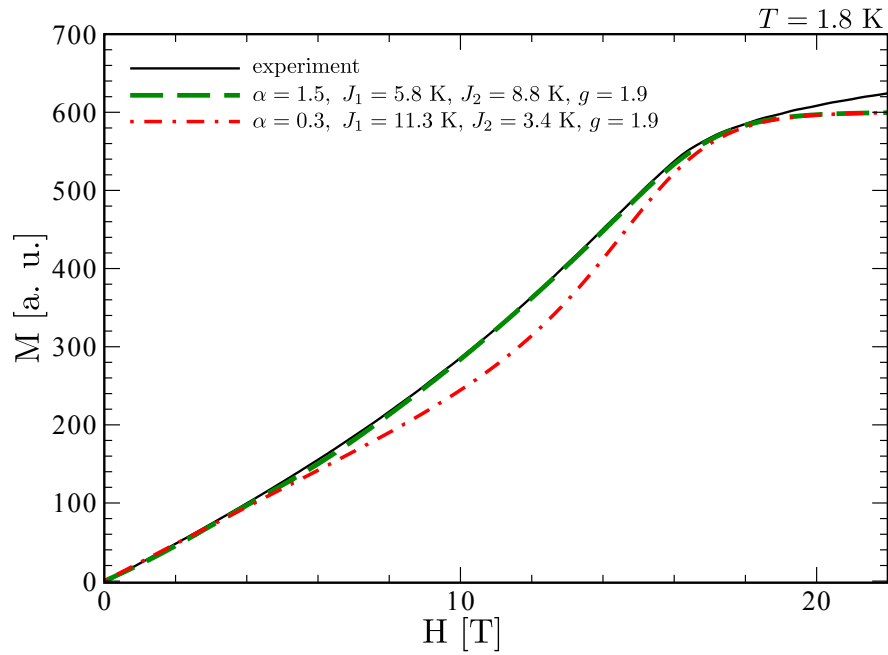
Figure 4.11: Magnetization of $KTi(SO_4)_2 \cdot (H_2O)$ measured at 1.8 K in fields up to 20 T. The dotted lines represent ED calculations for $N = 20$ performed by O. Janson.

agreement for $\alpha \sim 1.5$. The slight upturn at $H > 18$ T is an experimental artefact.

4.3 Quasi-$1D$ Magnetism in Titanium Yavapaiite

During the attempts to optimise the synthesis of $KTi(SO_4)_2 \cdot (H_2O)$, a light blue Ti-containing phase was often found to result instead of the target material. This mysterious phase was identified by X-ray diffraction to be the anhydrous end member of the titanium alum family, $KTi(SO_4)_2$ $(x = 0)$. Unlike $KTi(SO_4)_2 \cdot (H_2O)$, $KTi(SO_4)_2$ is not a new material – its structural and magnetic properties were first reported in 1996 by Bramwell *et. al.* [Bramwell *et al.* (1996)], who identified it as a possible realisation of the Ising model on an anisotropic triangular lattice. Our magnetic susceptibility and neutron scattering support a different interpretation, instead indicating that the system is best described as a one-dimensional Heisenberg chain. This difference is a consequence of the improved sample purity yielded by our preparation method.

4.3.1 Synthesis and Structure

The literature synthesis of $KTi(SO_4)_2$ requires vacuum dehydration of a stoichiometric solution of K_2SO_4 and $Ti_2(SO_4)_3$, then several cycles of regrinding and annealing at $350°$ C [Bramwell *et al.* (1996)]. Our method is radically different, rather resembling
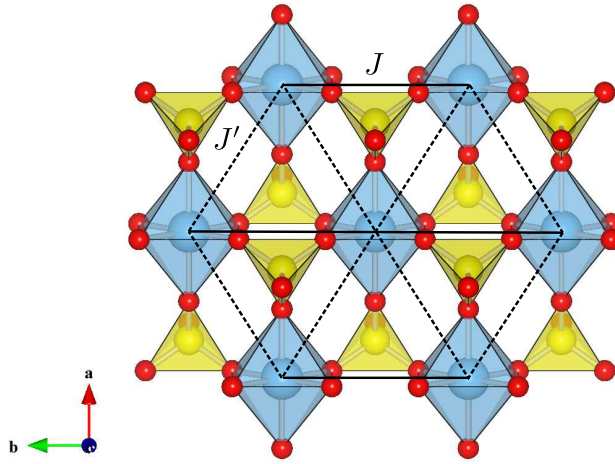
Figure 4.12: The structure of $KTi(SO_4)_2$ viewed along the c axis. Only the $Ti(SO_4)_2$ planes are shown, with the K^+ ions left out for clarity. The TiO_6 octahedra are coloured light blue, while SO_4 tetrahedra are yellow. Each Ti^{3+} ion is linked with its six neighbouring ions by two SO_4^{2-} bridges, a similar bridging motif as in $KTi(SO_4)_2 \cdot (H_2O)$. The anisotropic triangular lattice is superimposed on the structure, with the solid lines representing J, and dotted lines J'. The distances corresponding to these are 5.15 Å and 4.85 Å, respectively.

that used for $KTi(SO_4)_2 \cdot (H_2O)$: experimental details are given in Appendix A. The synthesis of $KTi(SO_4)_2$ is significantly more robust than that of $KTi(SO_4)_2 \cdot (H_2O)$, indicating that the latter is perhaps only a metastable state, with $KTi(SO_4)_2$ being the global thermodynamic minimum in much the region of phase space explored.

The crystal structure of $KTi(SO_4)_2$ is found by both powder and single crystal diffraction to be consistent with that reported by Bramwell *et. al.* [Bramwell *et al.* (1996)]. The space group is monoclinic $C2/m$, with lattice parameters $a = 8.28$ Å, $b = 5.22$ Å, $c = 7.84$ Å, and $\beta = 94°$ (further details are given in Appendix A). Structurally, $KTi(SO_4)_2$ consists of TiO_6 octahedra bridged by SO_4 groups to form slightly distorted $2D$ triangular layers (figure 4.12). These are separated along the c direction by K^+ ions, yielding an interplanar distance of 7.94 Å (figure 4.13). The bridging motif within the planes in $KTi(SO_4)_2$ is rather similar to that seen in $KTi(SO_4)_2 \cdot (H_2O)$, and indeed the structures can be related by a simple transformation: starting from the structure of $KTi(SO_4)_2 \cdot (H_2O)$, the hydrogen atoms are removed from the apical H_2O molecule. Then, the double chains are squeezed together along the c direction to form triangular planes. Crucially, the TiO_6 octahedra become tetragonally distorted during this transformation, with axial and equatorial Ti-O distances of 1.95 Å and 2.00 Å, respectively.
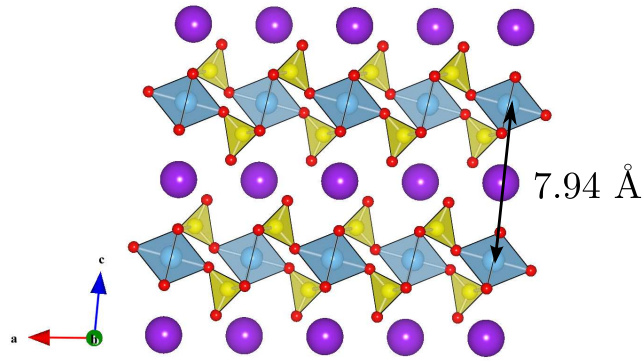
Figure 4.13: The stacking of the $Ti(SO_4)_2$ planes in $KTi(SO_4)_2$: the separation of two Ti^{3+} ions on adjacent planes is 7.94 Å. The colour scheme of the previous figure is adopted for the $Ti(SO_4)_2$ planes, with K^+ ions indicated in purple.

4.3.2 Magnetic Susceptibility

The magnetic susceptibility of $KTi(SO_4)_2$ was originally reported in the study of Bramwell *et. al.*. The temperature dependence of χ shows a shoulder around $7-9$ K, with a large Curie tail at lower temperatures (figure 4.14). The μ_{eff} and θ extracted from the high temperature region were found to be 1.39 μ_B and $-10.2(1)$ K, the former well short of the spin only value of 1.73 μ_B. This reduction was ascribed to coupling to an unquenched orbital moment of effective $l = -1$, yielding an Ising anisotropy in addition to the diminished moment. Magnetic data on samples synthesised by our method are found to tell a rather different story. A plot of χ versus T measured in a SQUID magnetometer at 100 Oe for a representative sample is shown in figure 4.14.

Fitting the high temperature part of the susceptibility to the Curie-Weiss law, $\chi = C/(T - \theta)$, yields parameters of $\mu_{eff} = 1.69\mu_B$ and $\theta = -20$ K. The former is rather close to the spin only value 1.73 μ_B, in contradiction with previous results. The latter is weakly antiferromagnetic, and roughly compatible with the values observed for $KTi(SO_4)_2 \cdot (H_2O)$. No order is observed down to the lowest T measured, 1.8 K.

The essentially spin-only moment extracted from the Curie-Weiss fit is easily explained by considering the influence of the crystal field on the orbital ground state of the Ti^{3+} ion. As shown at the beginning of this chapter, a tetragonal crystal field potential of positive sign (*i.e.* the octahedron is compressed along the unique axis) results in an orbital singlet ground state with $L = 0$ and $S = 1/2$. As the distortion is substantial, it is expected that the splitting between the ground state and the doubly degenerate excited state is likewise large, making the restoration of orbital moment due to LS coupling negligible.
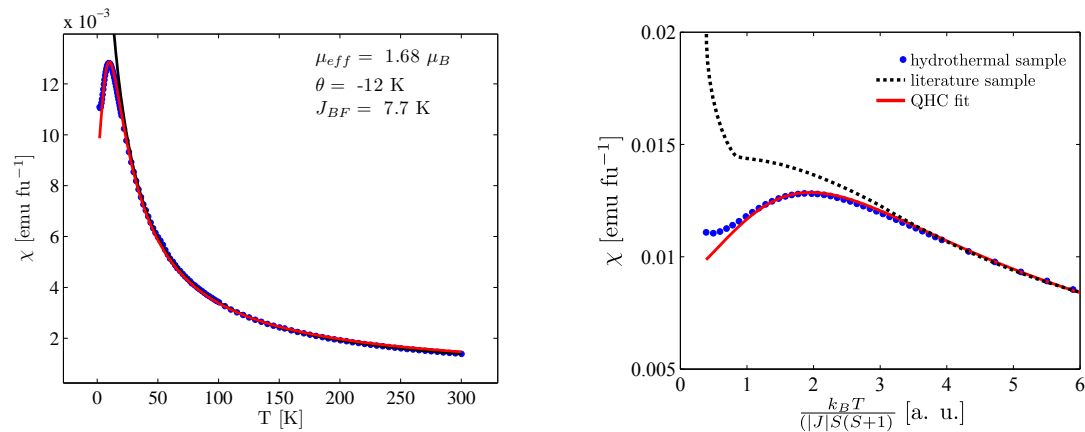
Figure 4.14: (left) Magnetic susceptibility of a sample prepared by the new hydrothermal method. The Curie tail has nearly been eliminated, and a clear peak is observed at 10 K. The Curie-Weiss fit is indicated by a solid black line, while the fit to the ED data for the QHC model is represented by a solid red line. (right) The magnetic susceptibility of a sample synthesised using the literature method and measured using the Faraday method compared with the magnetic susceptibility of a new sample prepared hydrothermally, plotted versus reduced temperature $T_r = Jk_B/[|J|S(S+1)]$. The large upturn at low temperature in the literature sample is a Curie tail associated with presence of paramagnetic defects. These are almost entirely absent in the sample prepared by the new hydrothermal method. The red curve again denotes the fit to ED data for the QHC model. Literature curve adapted from Bramwell *et. al.* [Bramwell *et al.* (1996)].
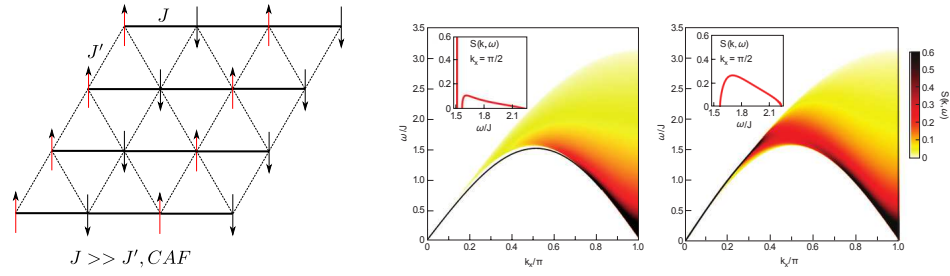
Figure 4.15: (left) The collinear antiferromagnetic (CAF) state predicted in the ATHA for $J >> J'$ by the renormalization group field theoretical approach of Starykh *et. al.* [Starykh and Balents (2007)]. (right) The calculated $S(\mathbf{Q}, \omega)$ within a slightly more general model where an additional interchain exchange is allowed. Deviations from the purely $1D$ spinon spectrum are seen due to interactions between spinons "living" on neighbouring chains: in the spectrum on the left, the δ function at $\omega = 0$ arises due to formation of triplon bound states, whereas the spectrum on the right shows redistribution of intensity to $\omega = \pi/2$ from repulsion of spinons [Kohno *et al.* (2007)].

The ground state wavefunction selected by the crystal field is of the d_{xy} type, resulting in the unpaired electron effectively lying in the bc plane. As such, the exchange is expected to be strongest along the b direction, where the overlap between the d_{xy} and O $2p$ orbitals is largest. Along the a direction, there is no direct overlap of these wavefunctions, and exchange along this direction can only occur assuming some mixing in of higher orbital states through the LS coupling.

Judging by the plausible orbital structure, the magnetic susceptibility may thus be described as arising due to $1D$ chains of $S = 1/2$ Heisenberg spins along the b direction, the Hamiltonian of which is:

$$\mathcal{H} = J \sum_{i,i+1} \mathbf{S}_i \cdot \mathbf{S}_{i+1} \tag{4.8}$$

Fits to exact diagonalisation results for this simple model indeed yield a good fit in the full temperature range measured, with fitted parameters of $J = 15.4$ K, and $g = 1.96$.

4.3.3 The Anisotropic Triangular Lattice Model

Even though the fit to χ versus T yielded by the simple quantum Heisenberg chain model (QHC) is almost perfect, it should not be taken for granted that the interchain coupling, J', is negligible. Indeed, the inclusion of such an interaction can subtly affect the ground state in ways which are not necessarily manifested in the thermo-

dynamic quantities. This was found to be the case for the distorted triangular lattice antiferromagnet Cs_2CuCl_4 [Coldea *et al.* (1997)], where neutron scattering indicated a considerable interchain exchange $J' = 0.34J$, despite an almost perfect correspondence between theoretical results for the QHC and thermodynamic data.

The Hamiltonian including the interchain interactions may be written as follows:

$$\mathcal{H} = J \sum_{i,i+1 \in n} \mathbf{S}_i \cdot \mathbf{S}_{i+1} + J' \sum_{\langle i \in n, j \in n \pm 1 \rangle}^{N} \mathbf{S}_i \cdot \mathbf{S}_j \tag{4.9}$$

where the former sum runs over the chains, whilst the latter describes the interchain interactions – this model is known as the anistropic triangular lattice Heisenberg antiferromagnet (ATHA). By varying the ratio of J'/J, the ATHA interpolates between the square lattice in the limit $J'/J \to \infty$, the triangular lattice for $J'/J = 1$, to the chain lattice for $J'/J \to 0$. Though J' may be non-negligible in $KTi(SO_4)_2$, it is still expected to be small. Thus, we find ourselves most interested in the chain limit of the ATHA.

Starting from isolated chains and switching on J' within the classical ATHA, the angle between nearest neighbouring spins along the chains begins to deviate from π, forming a spiral along the J direction. The relationship between the pitch angle of the spiral ϕ, and the relative magnitudes of J' and J is $\phi = 2 \arcsin\left[J'/(2J)\right]$ [Coldea *et al.* (2003)].

In the quantum ATHA model, the presence of a finite J' is much less efficient at inducing order than in the unfrustrated case. Indeed, the energy scale for ordering is $(J')^4/J^3$ [Starykh and Balents (2007)]. Neither does J' induce a canting of the spins, as expected from the classical result. This effect is due to the stabilisation of collinear structures (figure 4.15) by quantum fluctuations: A renormalisation group analysis of the perturbing J' interaction in the framework of the critical Wess-Zumino-Novikov-Witten (WZNW) conformal field theory shows that the collinear structure is stable up to a large critical $(J'/J)_c = 0.63$. While the quantum renormalization of pitch angle ensures that the dispersion remains identical at low J', the effect of the increasingly $2D$ nature of the system makes itself felt through the distribution of spectral weight in (Q,ω) space. For example, δ function anomalies are found to arise at $\omega = 0$ due to formation of a so-called triplon state from two spinons on adjacent chains [Kohno *et al.* (2007)] (figure 4.15).
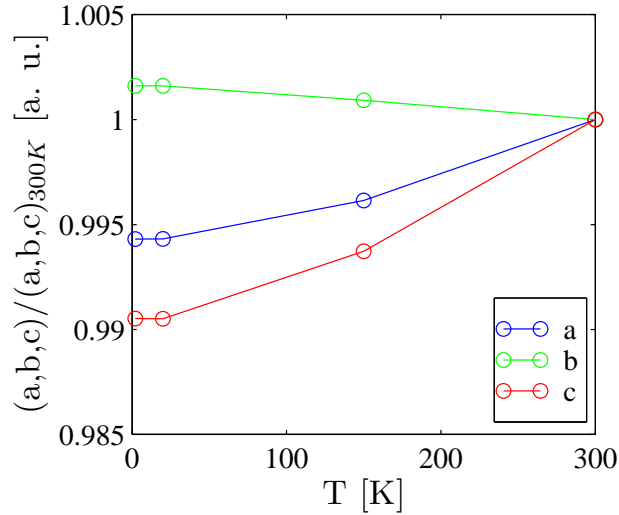
Figure 4.16: Temperature dependence of the lattice parameters a, b, c scaled to their room temperature values. A large contraction of a and c is observed cooling from room temperature to 1.8K.

4.3.4 Elastic and Inelastic Neutron Scattering

In order to gain a greater insight into the presumed microscopic model behind the magnetism of $KTi(SO_4)_2$, both elastic and inelastic neutron scattering investigations were performed.

4.3.4.1 Elastic Powder Diffraction

Neutron diffraction was performed on the D1B instrument at the Institut Laue Langevin with the kind assistance of C. Ritter. Spectra were measured at 4 temperatures: 1.8 K, 4.0 K, 150 K and 300 K. As expected from the magnetic susceptibility data, no magnetic order is found down to the lowest temperatures measured. Neither do any structural transitions occur. Rietveld refinement of the data reveals two features, however: the first is the presence of an impurity phase determined to be the rutile phase of TiO_2. This material, however, is diamagnetic, and does not affect either χ (beyond a small diamagnetic background), nor the later inelastic scattering experiments.

The second observation is that the refined lattice parameters exhibit a strong T-dependence, with the a and c parameters decreasing by respectively 0.5 and 1 percent versus the room temperature structure, and the b parameter (corresponding to the direction of the chains) slightly increasing (figure 4.16). The softness of the lattice in the a direction versus the b direction implies occupation of the d_{xy} orbital.

4.3.4.2   Inelastic Scattering: Temperature Dependence

The excitation spectrum of $KTi(SO_4)_2$ was measured using the inelastic time of flight method on the IN5 spectrometer at the Institut Laue Langevin. Approximately 12 g of powder from several batches, all of which had been characterised by XRD and magnetic susceptibility prior to combination, were loaded into a Cu can which was mounted on the end of a dilution refrigerator. Spectra were measured at several wavelengths and temperatures: 4.4 Å (0.05, 1.5, 3.0, 5.0, 7.0, 10.0K), 5 Å(0.05, 1.0, 1.8 K), 7 Å(0.05, 1.3, 1.8, 5.0 K), and 8.5 Å(0.05, 1.3 K).

First, we consider the temperature dependence of the background subtracted dynamical scattering function $S(Q, \omega)$ measured at the shortest wavelength, 4.4 Å(figure 4.17). $S(Q, \omega)$ at 10 K reveals two prominent branches of scattering, one strong, the other weaker, originating at $Q = 0.35\text{Å}^{-1}$. The weaker branch disperses linearly with ω, with an approximate slope of 6 meV/Å^{-1}. The stronger remains at low ω, with pronounced maxima at $Q = 0.5$ Å^{-1}, $\omega = 0.8$ meV and $Q = 0.65$ Å^{-1}, $\omega = 1$ meV. Investigation of background spectra and data taken at other wavelengths reveal these two to be artifacts due to scattering from the sample environment, enhanced by multiple scattering processes involving the sample and its surroundings. As a result, background subtraction does not yield a clean spectrum.

In addition to the spurious features, a broad continuum of magnetic scattering is visible between 0.4 $\text{Å}^{-1} < Q < 1.5$ Å^{-1} and from ~ 1 meV up to 2.5 meV. As T is reduced, the intensity of this continuum increases, particularly between 0.5 $\text{Å}^{-1} < Q < 0.8$ Å^{-1}, and it acquires a peak at a constant $\omega = 2.2$ meV for all Q. Below 5 K, spectral weight is observed to move from the continuum to the 2.2 meV peak. Simultaneously, the continuum takes on the approximate form of a sinusoidal dispersion emerging from $Q \sim 0.6$ Å^{-1}, with a bandwidth equal to the energy of the flat band.

Moving to longer wavelengths, the magnetic response of the system can be more clearly resolved from the background scattering, as the latter shifts to lower Q. At 0.05 K and 5 Å (figure 4.18), the dispersive feature is largely unaffected at $\omega > 0.2$ meV, whilst the peak only intersects the spurious scattering at $Q = 0.5$ Å^{-1}. The sinusoidal form of the dispersion is confirmed, and intensity is observed to be concentrated on the branch dispersing upwards in Q. Data taken at 7 Å (figure 4.18) and 8.5 Å finally reveal that the dispersion is gapless, and allow for a more accurate determination of the position at which is reaches zero energy as $Q = 0.6$ Å.
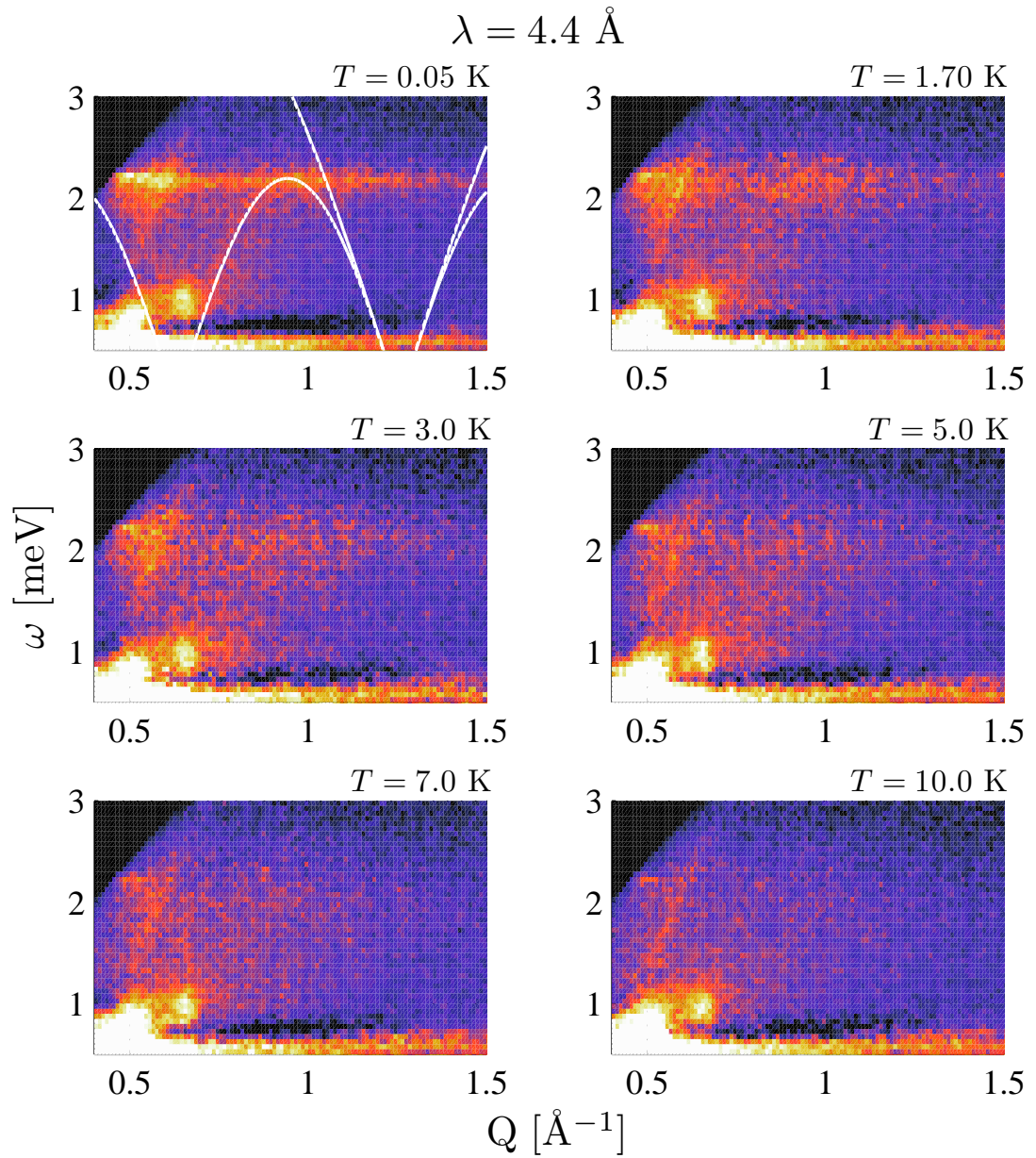
Figure 4.17: The temperature dependence of $S(Q,\omega)$ for KTi(SO$_4$)$_2$. The boundaries of the two-spinon continuum, $\omega_{2,l}$ and $\omega_{2,u}$ are indicated by white lines in the top left panel.
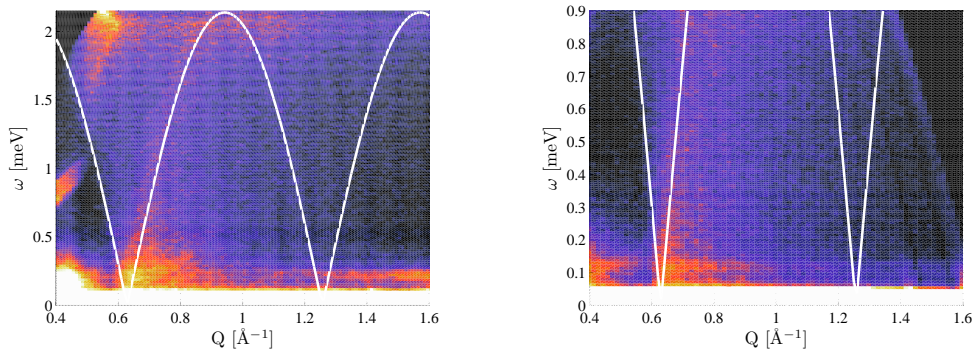
Figure 4.18: (left) $S(Q,\omega)$ at 5 Å^{-1} measured at 0.05 K. The solid line represents the lower bound of the two-spinon continuum, $\omega_{2,l}$, as discussed in the text. (right) As left, for 7 Å. The flat feature at approximately 0.12 meV is spurious.

4.3.4.3 Analysis of Inelastic Spectra

From the structure of the material, as well as the magnetic susceptibility, the $1D$ chain Heisenberg antiferromagnet is a logical starting point for the analysis. The earliest work on the excitation spectrum of $1D$ $S = 1/2$ Heisenberg antiferromagnet was perfomed by des Cloizeaux and Pearson [des Cloizeaux and Pearson (1962)], who found the spinon ($S = 1/2$) dispersion relation to be:

$$\omega = \frac{\pi J}{2}|\sin(Q)| \tag{4.10}$$

Of course, neutron scattering is only sensitive to processes with $\Delta S = \pm 1$ and it is thus the 2-spinon continuum which is the quantity of interest. This continuum has upper and lower bounds as follows:

$$\omega \geq \omega_{2,l} = \frac{\pi J}{2}|\sin(Q)| \tag{4.11}$$

$$\omega \leq \omega_{2,u} = \pi J|\sin\left(\frac{Q}{2}\right)| \tag{4.12}$$

where $\omega_{2,l}$ and $\omega_{2,u}$ are the upper and lower bounds, respectively.

Using the value of J extracted from the fit to the magnetic susceptibility, good agreement between the position of the two-spinon continuum and the experimental data is achieved assuming a two dimensional propagation vector $\mathbf{q} = (0, 1/2)$ (figure 4.18). Despite the two dimensionality, the incommensuration along b expected from semi-classical spin wave theory is not observed. This may be a result of the well known effect whereby quantum fluctuations select commensurate wavevectors in frustrated low dimensional
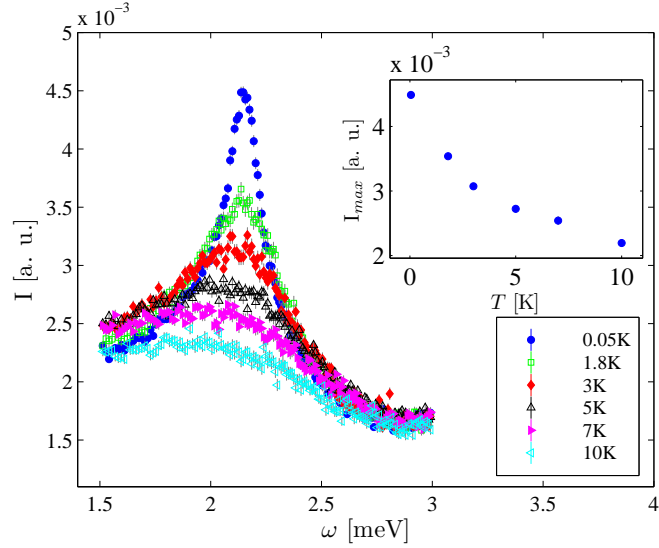
Figure 4.19: The T-dependence of the constant-ω anomaly at 2.2 meV. (inset) The T-dependence of the peak intensity. The apparent divergence of this quantity is interpreted as evidence for the $1D$ nature of the system.

systems. For example, in the $1D$ frustrated chain compound LiCuVO$_4$ [Enderle *et al.* (2005)], the experimentally observed helical order has a far greater pitch angle $\alpha \sim \pi/2$ than expected classically.

In order to extract more detailed information on the applicability of the $1D$ Heisenberg model to KTi(SO$_4$)$_2$, the dynamical structure factor must be considered in more depth. The two-spinon $S(Q, \omega)$ has recently been derived exactly from the XXZ limit by J.-S. Caux [Caux *et al.* (2008)], yielding the expression:

$$S(Q, \omega)_2 = \frac{1}{2} \frac{e^{-I(\rho(Q,\omega))}}{\sqrt{\omega_{2,u}^2(Q) - \omega^2}} \Theta(\omega_{2,u}(Q) - \omega)\Theta(\omega - \omega_{2,l}(Q)) \tag{4.13}$$

where Θ is the Heaviside step function, and $I(\rho)$ and ρ are given as follows:

$$\cosh(\pi\rho(Q, \omega)) = \sqrt{\frac{\omega_{2,u}^2 - \omega_{2,l}^2}{\omega^2 - \omega_{2,l}^2}} \tag{4.14}$$

$$I(\rho) = \int_0^\infty dt \frac{e^t}{t} \frac{\cosh(2t)\cos(4\rho t) - 1}{\cosh(t)\sinh(2t)} \tag{4.15}$$

Powder averaging of the result, usually a tedious and computationally demanding task for systems of $D \geq 2$, is greatly simplified in $D = 1$, reducing to a simple polar integral as follows:
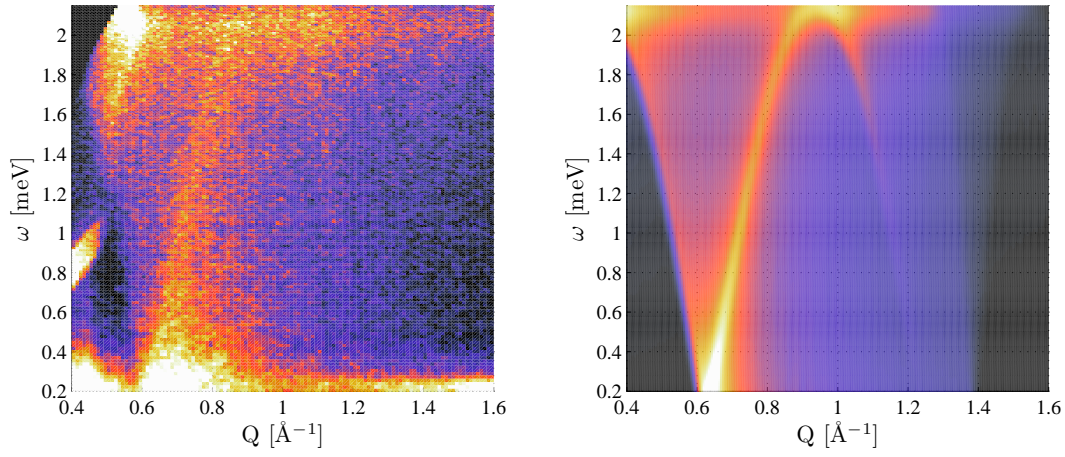
Figure 4.20: (left) The experimental $S(Q, \omega)$ measured at 5 Å. (right) The theoretical result as calculated in the text.
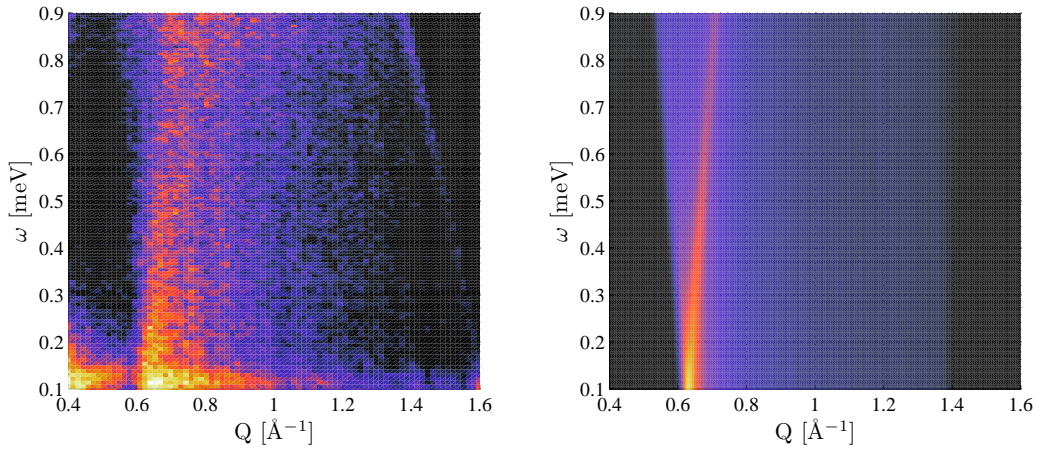

Figure 4.21: As above for 7 Å.

$$
\begin{aligned}
S(\mathbf{Q}, \omega)_p &= \frac{1}{Q} \int_{-1}^{1} d(\cos \theta) \int_{0}^{2\pi} d\psi \frac{S(q_x, \omega)}{4\pi} \\
&= \frac{1}{Q} \int_{0}^{1} d(\cos \theta) S(Q', \omega) \\
&= \frac{1}{Q} \int_{0}^{Q} dQ' S(Q', \omega)
\end{aligned}
\tag{4.16}
$$

where $Q' = Q \cos \theta$. Finally, the powder averaged cross section was convoluted with a Gaussian instrumental resolution determined by fitting the Q-width of several Bragg peaks, as well as the ω incoherent background for each wavelength. Qualitative agreement between calculation and experimental is at first sight very good (figures 4.20 and 4.21). The sharp, flat feature at $\omega_p = 2.2$ meV seems to be an artefact of powder averaging a one dimensional dispersion. It is in this respect similar to the van Hove
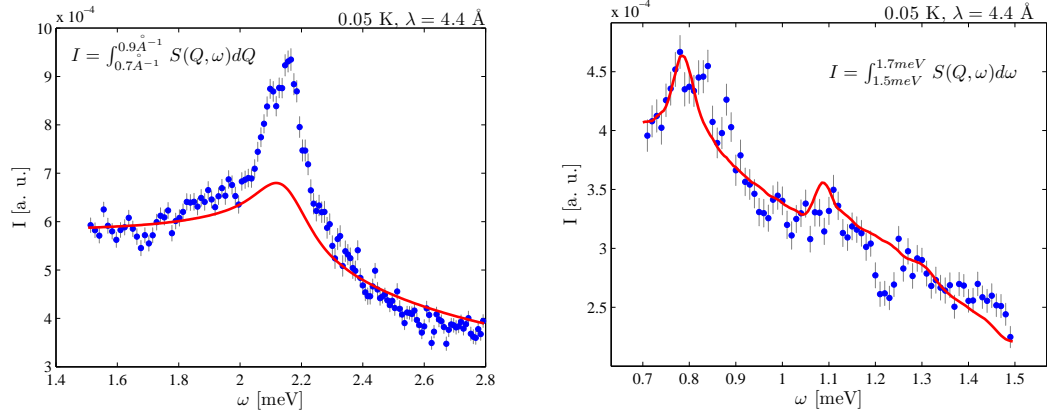
Figure 4.22: Fits of selected cuts through $S(Q,\omega)$ at 4.4 Å as described in the text. A cut through a high background region is indicated on the left, with a cleaner cut shown on the right.
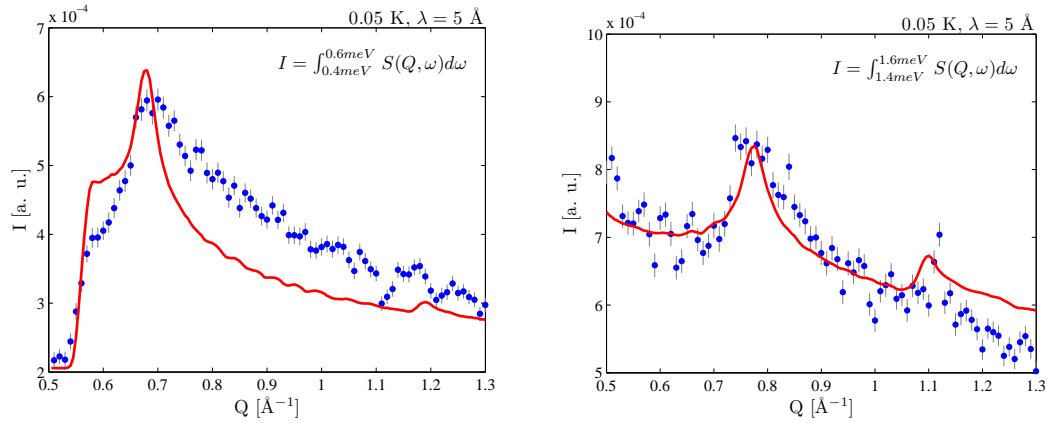

Figure 4.23: Fits of selected cuts through $S(Q,\omega)$ at 5 Å as described in the text. A typical cut through a region of low multiple scattering and background is shown on the right, whereas a multiple scattering affected cut is shown on the left.

singularities observed in the electronic density of states of low dimensional conductors.

Several ω and Q cuts of the experimental $S(Q,\omega)$ were fitted to the theoretical result scaled by an amplitude, A, which was kept constant for all the cuts. The only free parameter in each fit was thus a small, flat background, which turns out to be fairly uniform. The results of this procedure are shown in figures 4.22 and 4.23. At small ω, and at ω_p, where the scattering is comparatively strong, the intensity extends much further in Q than is the case for the theoretically predicted cross section. As a large sample was used, this is at least partially due to multiple scattering. The fact that the data are better described by theory in regions where the scattering is weaker supports this interpretations.

As discussed in Chapter 2, the critical temperature of the $1D$ Heisenberg chain model is zero. As such, a number of experimentally measureable quantities of the system are anticipated to diverge logarithmically as $T \to 0$. Using the bosonization approach, this has been shown to be the case for the $\omega = 0$ scattering function $S(Q, 0)$, which scales as $S(Q, 0) \sim (1/T)\sqrt{\ln \Lambda/T}$, where $\Lambda = 24.27$ is a constant [Kokalj and Prelovsek (2009)]. The exact details of the finite temperature scaling at $\omega > 0$ are less well established, but recent DMRG studies [Barthel *et al.* (2009)] indicate that a similar dependence should be expected for the peak amplitude along the lower bound of the spinon continuum. Returning to the 4.4 Å data, the temperature dependence of the peak feature should crudely reflect this tendency. Indeed, the peak amplitude does appear to diverge as $T \to 0$ (figure 4.19).

4.3.5   Conclusions

A new synthetic route to titanium yavapaiite, $KTi(SO_4)_2$, has been discovered and optimised to yield samples of unsurpassed quality. Fitting of the high temperature region of the magnetic susceptibility to the Curie-Weiss law indicates that the spin symmetry is Heisenberg, rather than Ising-like, as previously suggested [Bramwell *et al.* (1996)]. The entirety of the susceptibility curve is well described by the theoretical result for the $1D$ Heisenberg chain, as calculated from exact diagonalisations of chains up to 18 spins. This result can be understood to arise as a consequence of the tetragonal distortion of the TiO_6 octahedra, which selects d_{xy} as the active orbital. Hence, the only effective superexchange pathway is along the b direction, with couplings along a arising only at higher order. The distortion also accounts for the large and symmetric moment observed in the magnetic susceptibility.

Elastic neutron scattering data support the orbital ordering hypothesis by indicating that the a and c lattice parameters strongly contract as T is reduced, with b remaining constant. The inelastic neutron scattering spectra are well described by an exact $S(Q, \omega)$ derived for the QHC using the Bethe ansatz, despite prominent background features, powder averaging, and multiple scattering. Furthermore, these measurements hint at coherence between the chains based on the position of the antiferromagnetic zone centre, which is only consistent with a collinear antiferromagnetic ordering vector $\mathbf{q} = (0, 1/2)$. Such behaviour has been predicted from a renormalisation group analysis of a perturbing interchain interaction within the WZNW conformal field theory [Starykh and Balents (2007)].

One particular areas of interest for future work is to determine to what extent the

spectrum is affected by the presence of the interchain interaction, J'.

Chapter 5

$S = 1/2$ Kagome Antiferromagnets: Volborthite and Herbertsmithite

$$\boxed{D = 2, \; z = 4, \; S = 1/2, \; \text{frustrated}}$$

The $S = 1/2$ Heisenberg model on the kagome lattice is one of the most extreme combinations of the ingredients of quantum magnetism, namely low dimensionality, low connectivity, and frustration, and hence also one of the strongest candidates for displaying quantum ground states. This chapter will discuss the mystery of the ground state of the quantum kagome model, and how experiments on two systems, volborthite and herbertsmithite, have attempted to solve it. While they ultimately fail to do so, much novel physics is nonetheless uncovered.

5.1   The Classical Kagome Antiferromagnet

Kagome, a basket weaving pattern named after the Japanese kanji for "eye" and "basket", describes a two-dimensional Archimedean lattice of corner sharing triangles, as shown in figure 5.1 [Syozi (1951)].

When the vertices of the kagome lattice are populated with classical spins, the ground state is macroscopically degenerate (see Chapter 2). This classical degeneracy is demonstrated by the fact that Hamiltonian may be rewritten entirely in terms of a local constraint:
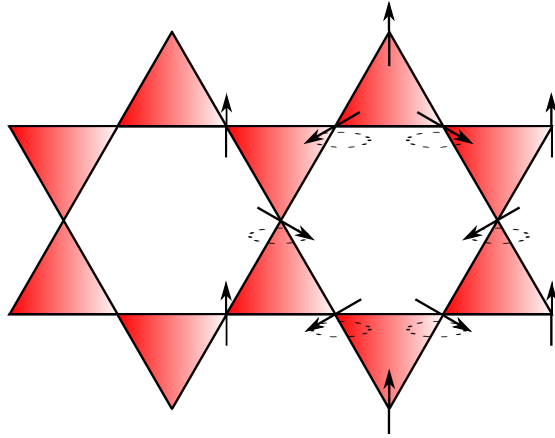
Figure 5.1: The kagome lattice. When populated with classical Heisenberg spins, the geometry of the lattice leads to macroscopic degeneracy. Order by disorder mechanisms select the ground states with the highest density of soft modes, one of which is shown on the right, where the spins are arranged in a so called staggered chirality of $\sqrt{3} \times \sqrt{3}$ order.

$$\mathcal{H} = \sum_{\langle i,j \rangle} \vec{S}_i \cdot \vec{S}_i = \frac{J}{2} \sum_{\triangle} |\vec{L}|^2 + c \tag{5.1}$$

where the sum runs over all triangles, and $\vec{L}$ is the total spin on a triangular plaquette $\vec{L} = \vec{S}_1 + \vec{S}_2 + \vec{S}_3$. A ground state is thus any of an infinite number of configurations where $\vec{L} = 0$ is locally satisfied. Thermal fluctuations select coplanar states from the ground state manifold, but the degree of freedom associated with the chirality on each triangle remains. As a result of this, the ground state is still extensively degenerate. Higher order spin wave theory and classical Monte Carlo (CMC) however indicate that the degeneracy is at least partly broken, and that correlations tend towards a pattern of staggered chiralities on adjacent triangles known as $\mathbf{q} = \sqrt{3} \times \sqrt{3}$ order. The $\mathbf{q} = \sqrt{3} \times \sqrt{3}$ pattern is favoured due to the especially high density of soft modes in this state. These manifest themselves as free rotations of spins within a hexagon about the axis of the spins bounding the hexagon.

In light of these results, it may come as somewhat of a surprise that most realisations of the classical kagome antiferromagnet (CKHAF) order in a 120° pattern with uniform chirality, the so-called $\mathbf{q} = 0$ order (see figure 5.2). How can this experimental fact be reconciled with the theoretical predictions? Of course, moving from theory to experimental realisation, a number of additional terms enter the Hamiltonian as perturbations. By lifting the macroscopic degeneracy of the ground state, these usually result in magnetically ordered ground states. Two examples of perturbations which result in long range order are DM interactions and next nearest neighbour couplings:

applying an infinitesimally small D_z, the CKHAF classically orders in the $\mathbf{q} = 0$ order at finite temperature [Elhajal *et al.* (2002)]. Antiferromagnetic next nearest neighbour couplings, on the other hand, restore $\mathbf{q} = \sqrt{3} \times \sqrt{3}$ order [Harris *et al.* (1992)].

5.2 The $S = 1/2$ (Quantum) Kagome Antiferromagnet

What happens to the ground state of the Heisenberg kagome antiferromagnet when the spin length is reduced from $S = \infty$ to $S = 1/2$? Will quantum fluctuations select static order, as was the case for the triangular lattice in a magnetic field? The answer, at least within linear spin wave theory, is no. For any ordered ground state on the kagome lattice, LSWT yields a completely flat band at $\omega = 0$, which ends up destroying the classical order parameter. As for what replaces the classical ground state, the theoretical consensus appears to be converging towards a 36-sublattice valence bond crystal (VBC). This section will discuss the properties of this state as well as some of its experimental signatures, in addition to highlighting what happens when perturbations such as anisotropies (single ion or Dzyaloshinskii-Moriya (DM)), presence of vacancies on the lattice, or reduction of lattice symmetry are included into the Heisenberg Hamiltonian. The influence of these perturbations will prove crucial to understanding the experimental results presented in coming sections.

5.2.1 Ground State and Excitations

The quantum kagome Heisenberg antiferromagnet (QKHAF) first rose to prominence in the late 1980's, when both linear spin wave theory and large-N (Schwinger boson) mean field theory were found to imply a breakdown of classical order for small spin [Sachdev (1992)]. Later, it was indicated that order from disorder effects at higher order in spin wave theory select $\mathbf{q} = \sqrt{3} \times \sqrt{3}$ long range order. This prediction was refuted soon after through an analysis of the low energy spectra of clusters up to 36 spins [Waldtmann *et al.* (1998)],[Zeng and Elser (1995)]. No easily identifiable quasi-degenererate joint states (see Chapter 2) are present in the spectrum, and furthermore, the gap between the lowest states in the $S = 0$ and $S = 1$ sectors contains an exponentially large number of singlets, scaling with system size as $\sim 1.15^N$, a feature not seen in classical antiferromagnets (figure 5.3). In addition, the spin-spin, quadrupolar, octupolar, and dimer-dimer correlations all fall off extremely rapidly, only extending as far as next-nearest neighbours [Chalker and Eastmond (1992)].

Another important piece of evidence which can be extracted from the numerical data
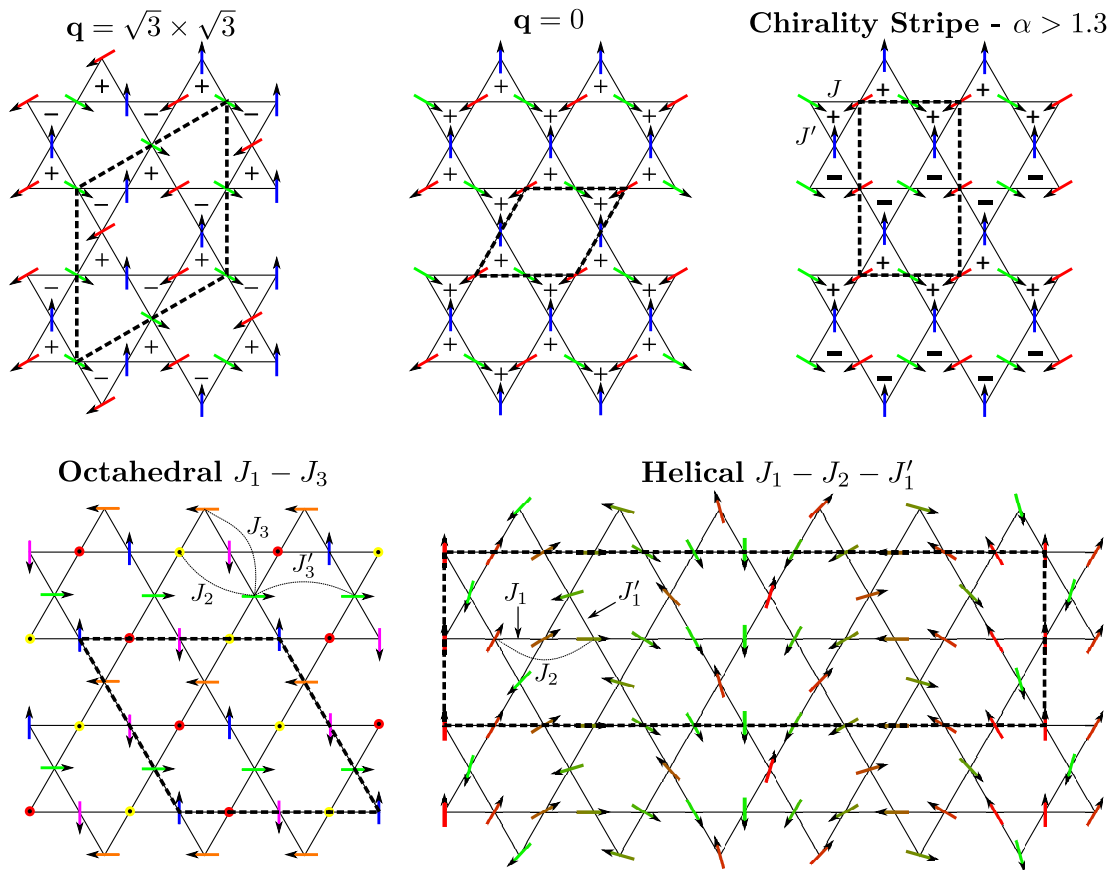
Figure 5.2: Some classically ordered patterns on the kagome lattice. (top left and centre) The $\mathbf{q} = \sqrt{3} \times \sqrt{3}$ and $\mathbf{q} = 0$ orders proposed for the pure kagome lattice. The latter of these is favoured in the case of finite Dzyaloshinskii-Moriya or single ion anisotropies. (top right) The chirality stripe (CS) state suggested for the spatially anisotropic kagome lattice, with $\alpha = J_1'/J_1 > 1.3$. (bottom left) Octahedral order induced by a further neighbour interaction $J_3 \sim J_1$. (bottom right) Helical order proposed for $J_1 - J_1' - J_2$ model, where J_2 and J_1' are antiferromagnetic, and J_1 is ferromagnetic.
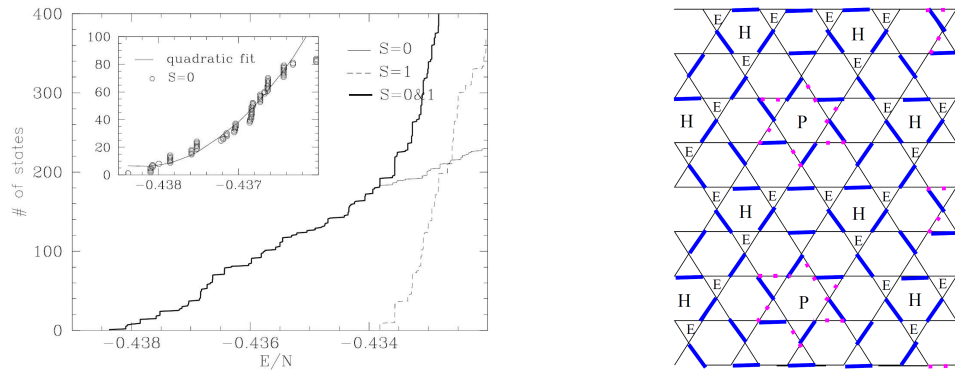
Figure 5.3: (left) The singlet and triplet density of states as calculated from exact diagonalisation. The gap between the lowest singlet and lowest triplet is filled with a high density of singlet states, 244 in the case of the $N = 36$. Adapted from Waldtmann *et. al.* (right) The 36-site VBC state originially proposed by Zeng and Elser. P marks pinwheel configurations and D defect triangles, that is, triangles which lack a valence bond.

concerns the spin gap, $\Delta = E_{mag}(S = 1) - E_{min}(S = 0)$, between the lowest $S = 1$ excitation and the lowest lying $S = 0$ state. In an ordered antiferromagnet, Δ vanishes as $\sim 1/N^2$, revealing the appearance of the Goldstone mode as $N \to \infty$. A $1/N^2$ extrapolation of Δ shows that this is not the case for the QKHAF, however – a small gap of $\sim 0.05J$ remains in the thermodynamic limit. While controversial for several years due to its small size, the presence of a gap has been verified more recently by DMRG calculations, which specify its value to be $\Delta = 0.055J \pm 0.005$ [Jiang *et al.* (2008)].

As the spin correlations are extremely short ranged and the ground state gapped, it is natural to turn to a nearest neighbour dimer state (whether a fluctuating RVB or static VBC) as a possible ground state for the QKHAF. This possibility was first proposed as early as 1991 by Marston and Zeng [Marston and Zeng (1991)] and developed by Zeng and Elser [Zeng and Elser (1995)] within the quantum dimer model. The ground state of this model is expressed as as a product of nearest neighbour dimers, $|D\rangle = \prod_{i,j} [ij]$, where $[ij]$ is a nearest neighbour dimer.

Treating the hopping of these objects in the same way as the hopping of electrons in the Hubbard model, all singlet coverings of the lattice are found to be degenerate up to 2nd order in t. At this level, the configurations which contain a maximal number of so-called pinwheels are selected by the fluctuations [Singh and Huse (2007)]. This favours the 36-sublattice VBC ground state shown in figure 5.3. The energy of this configuration is $-0.438377J$, consistent with that extrapolated from ED results.

The spin-1 excitations associated with breaking a local singlet in the VBC are gapped
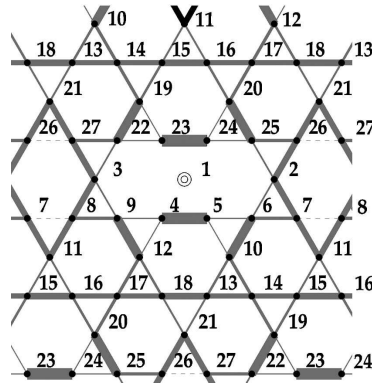
Figure 5.4: Enhancement of local singlet correlations in the vicinity of a defect, from exact diagonalisation studies by Dommange *et. al.*. The thicknesses of the bonds are proportional to the pair correlation function $\langle S_i S_j \rangle$.

pairs of spinons called kink-antikink pairs [Hao and Tchernyshyov (2009)]. The antikinks remain localized and are gapless, whilst kinks are mobile and have a gap of $0.218J$. Another kind of spin-1 excitation arises at yet lower energies from exciting defect triangles, that is, triangles which lack a singlet bond, which may be considered a bound pair of antikinks. The gap corresponding to such an excitation is $0.06J$, corresponding to the singlet-triplet gap observed in the ED results. The low ω ($< J/2$) structure factor, $S(Q)$, of antikink excitations was shown by Hao *et. al.* [Hao and Tchernyshyov (2009)] to follow the nearest neighbour antiferromagnetic structure factor, $[1 - \sin(Qr_{nn})/(Qr_{nn})]$, where r_{nn} is the nearest neighbour distance.

5.2.2   Defects, Anisotropies and Dzyaloshinkii-Moriya Interactions

Going from a simple theoretical model to experimental realisation usually also entails inclusion of terms beyond the simple bilinear exchange term in the Heisenberg Hamiltonian. These terms may include single ion anisotropies, further neighbour interactions, as well as the DM interaction. In addition, vacancies may be introduced. As it turns out, these interactions have a crucial effect on the ground state of the QKHAF:

- **Dzyaloshinksii-Moriya** - As was the case for its classical analogue, DM interactions induce long range order in the QKHAF. Whereas in the classical model, an infinitesimally small D_z is sufficient to generate $\mathbf{q} = 0$ order, in the quantum case, order only occurs for $|D|_c > 0.1$ [Cepas *et al.* (2008)]. The ordered and disordered ground states are separated by a quantum phase transition. The magnitude of the critical value D_c hints at a small spin gap protecting the ground state.

- **Vacancies** - Inevitably, a real crystalline material will contain defects. The

easiest type of defect to treat theoretically is a point defect, such as a vacancy. Dommange *et. al.* [Dommange *et al.* (2003)] considered small clusters of 27 spins, with one or two vacancies distributed among them. The most dramatic effect of introducing a vacancy is a strong enhancement of the nearest neighbour correlation function $\langle S_i S_j \rangle$ in the immediate vicinity of the vacancy (figure 5.4). This effect may be understood to arise due to a local relief of frustration.

- **Lattice Anisotropy** - A large amount of work has also been carried out on the spatially anisotropic kagome lattice antiferromagnet, particularly in the context of the material volborthite, which will be the subject of the next section. This model is described by the Hamiltonian:

$$\mathbf{H} = J_1 \sum_{[i,j]} \mathbf{S}_i \cdot \mathbf{S}_j + J_1' \sum_{\langle i,k \rangle} \mathbf{S}_i \cdot \mathbf{S}_j \qquad (5.2)$$

where the former sum runs over spins lying along one axis, whilst the latter couples spins on the chains with spins in between 5.2.

Classically, this model has a rather rich phase diagram: starting from the limit $J_1' >> J_1$, corresponding to a square lattice decorated with an additional spin on each bond, the ground state is ferrimagnetic, with 2 spins up for each spin down. At the point $\alpha = J_1'/J_1 = 2$, the system crosses over into a spiral regime, where the ground state becomes degenerate, with the local constraint to satisfy being that the nearest neighbour spins along the unique direction are at angle, θ, with respect to each other, determined by $\theta = \arccos J_1'/2J_1$. This state persists through the $\alpha = 1$ point, which regenerates the isotropic CKHAF, and beyond. At large α, the lattice eventually separates into decoupled chains.

The quantum mechanical calculation for the AKAF has been attempted by several different approaches: large-N Schwinger boson mean field theory [Yavors'kii *et al.* (2007)], spin wave theory, chirality mean field theory, and exact diagonalisations [Wang *et al.* (2007)]. The consensus from these is that for $1 < \alpha < 1.3$ and $\alpha \neq 1$, quantum fluctuations stabilise the $\sqrt{3} \times \sqrt{3}$ state, whilst for $\alpha > 1.3$, an entirely new order arises: the so-called chirality stripe order [Wang *et al.* (2007)]. In this ground state (see figure 5.2), the chiralities form stripes along the J_1 direction, with the chirality alternating along the J_1' direction. The excitations spectrum goes from being gapless over the entire Brillouin zone, to only being soft along a single direction. The unique behaviour of the QKHAF is only recovered at the isotropic point, $\alpha = 1$.
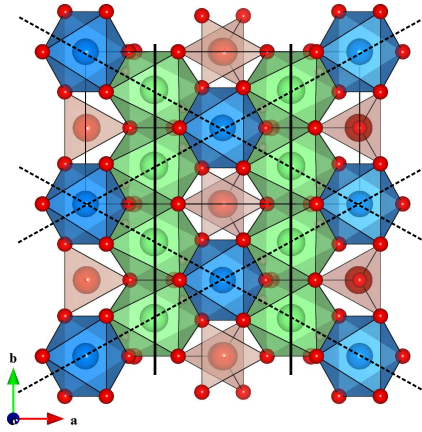
Figure 5.5: The distorted kagome planes in volborthite. Green octahedra indicate Cu(1), and blue Cu(2). The top VO_4 tetrahedron of the pyrovanadate column (V_2O_7) is shown in red. J_1 and J_1' are indicated by, respectively, solid and dotted lines, and correspond to Cu-Cu distances of 2.93 Åand 3.03 Å.
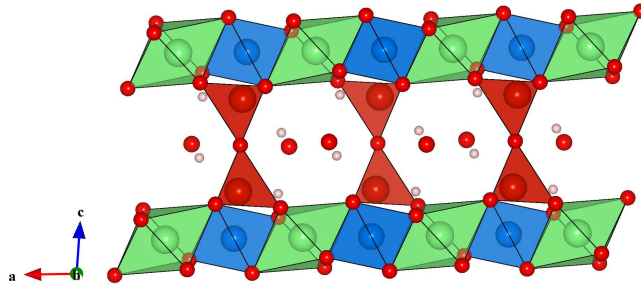

Figure 5.6: The stacking of the kagome planes along the c-axis. The interplane distance is approximately 7.2 Å.

5.3 Volborthite

5.3.1 Structure

Among the first materials identified as a candidate for realising the KHAFM was volborthite, $Cu_3V_2O_7(OH)_2 \cdot 2H_2O$, a rare mineral originating in the Ural mountains [Lafontaine *et al.* (1990)]. It crystallises in the monoclinic $C2/m$ spacegroup, with lattice parameters $a = 10.61$ Å, $b = 5.86$ Å, $c = 7.21$ Å, and $\beta = 94.9°$. The space group lacks the threefold axis required to generate a perfect kagome lattice, and indeed, the triangular building blocks which make up the kagome plane are isosceles, with one short and two long edges (figure 5.6). Due to the distortion, there are also two crystallographically distinct Cu sites: the first, Cu(1), resides in a strongly axially distorted octahedron ($r_{ax} = 2.37$ Å, $r_{eq} = 2.04$ Å) and makes up the bases of the triangles. Cu(2)
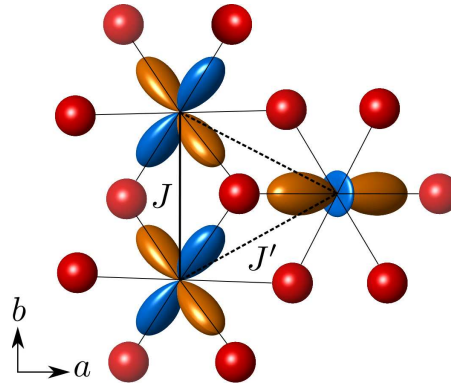
Figure 5.7: The magnetically relevant orbitals in volborthite. The singly occupied orbital on the axially distorted Cu(1) site is the $d_{x^2-y^2}$ orbital, whereas d_{z^2} is selected by the tetragonal distortion on the Cu(2) site. Superexchange proceeds via the oxygen $2p$ orbitals (not shown), as well as the $2p$ orbitals of the central μ_3-O. The structural motif along the b axis resembles that of several $J_1 - J_2$ chain materials, where J_1 is typically ferromagnetic and J_2 antiferromagnetic.

is coordinated in a tetragonally distorted octahedron ($r_{ax} = 1.91$ Å, $r_{eq} = 2.16$ Å) and populates the apices of the triangles. The local geometry at the two Cu sites points to orbital ordering, with the unpaired electrons on the Cu(1) and Cu(2) sites, respectively residing in the d_{z^2} and the $d_{x^2-y^2}$ orbitals (figure 5.7). Magnetic exchange proceeds through two different pathways: Cu(1) is linked to Cu(2) via a single μ_3-OH bridge. The Cu-O-Cu bond angle is 105°, and the Cu-Cu distance is 3.03 Å. The other pathway connects two Cu(1) sites along the b axis. For this interaction, a μ_3-OH group and a μ_2-O participate in bridging the two Cu ions. The Cu-O-Cu angles are 91° and 100°, respectively, and the Cu-Cu distance is 2.93 Å. Henceforth, the Cu(1)-Cu(1) interaction will be called J_1 and the Cu(1)-Cu(2) interaction J_1'.

The structural motif along the b direction, consisting of edge sharing chains of axially distorted octahedra, particularly resembles the CuO$_4$ edge sharing motif seen in a number of one dimensional frustrated magnets, such as CuGeO$_3$ [Hase *et al.* (1993)] and LiCu$_2$O$_2$ [Masuda *et al.* (2005)]. In both materials, the $d_{x^2-y^2}$ orbitals carry the spin, and the nearest neighbour Cu-O-Cu angle is close to 90°. The consequence of this arrangement is that the nearest neighbour interaction is typically weak and ferromagnetic, whilst the next nearest neighbour interaction is stronger and antiferromagnetic. This interaction, which we will call J_2, will prove important in the case of volborthite, as we shall see later.
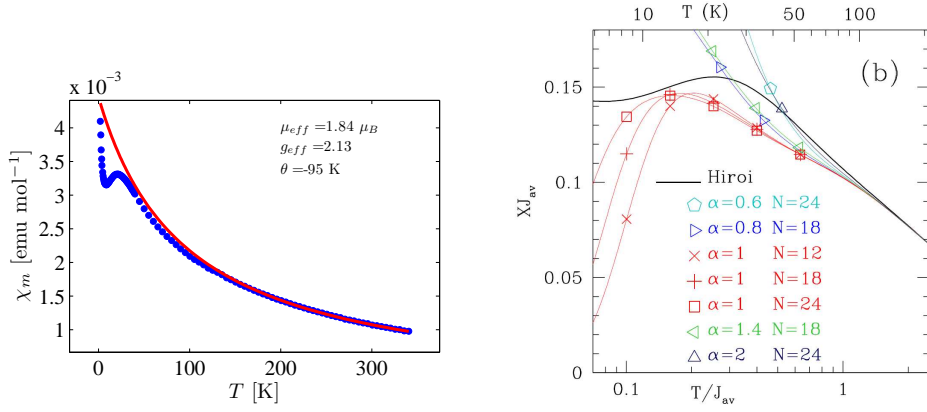
Figure 5.8: (left) The magnetic susceptibility of volborthite measured at 100 Oe. The Curie-Weiss fit to the data is shown in red, with parameters as indicated in the top right corner. These are approximately consistent with the literature values, $\mu_{eff} = 1.83 \ \mu_B$ and $\theta = -115$ K – the discrepancy in θ is a consequence of the fitting ranges used. The upturn at low temperature is a Curie tail associated with the presence of approximately 1% (with respect to the total sample mass) of paramagnetic defects. (right) A comparison of the experimental susceptibility data (black line) with the results of exact diagonalisations on finite clusters of size $N = 18, 24$. $J_{av} = (J_1 + 2J_1')/3$. The best agreement between experiment and theory is achieved for $\alpha = 1$ (red lines) [Sindzingre (2007)].

5.3.2 Experimental Background

Magnetic susceptibility measurements on volborthite reveal no features indicating long range magnetic order down to 1.8 K (figure 5.8). There is however a broad maximum centered at around $\chi_{max} = 20$ K, which implies short range correlations. At low temperature, a Curie tail is observed due to a small $[\mathcal{O}(1\%)]$ population of paramagnetic defects. A fit to the Curie-Weiss law $\chi = C/(T - \theta)$, in the region $250 - 300$ K $(> \sim 3\theta)$ yields a μ_{eff} of $1.83\mu_B$, corresponding to a $g_{eff} = 2.12$, typical of Cu^{2+}. The Weiss constant, $\theta = -95$ K, indicates dominant antiferromagnetic couplings. In earlier studies by Hiroi *et. al.* [Hiroi *et al.* (2001)] a fit of the HTSE for the isotropic kagome lattice to the magnetic susceptibility yields $J_{av} = (J_1 + 2J_1')/3 = 84$ K, crudely consistent with θ.

The simplest realistic model Hamiltonian which can be formulated to describe the magnetism of volborthite is the anistropic kagome antiferromagnet (AKAF), where only J_1 and J_1' are considered relevant:

$$\mathcal{H} = J_1 \sum_{\langle i,j \rangle} \mathbf{S}_i \cdot \mathbf{S}_j + J_1' \sum \mathbf{S}_i \cdot \mathbf{S}_j \tag{5.3}$$
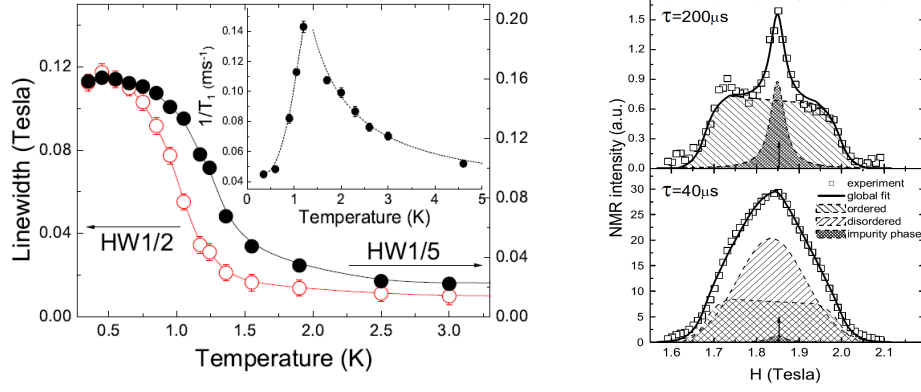
Figure 5.9: (left) The half widths of the NMR spectrum measured at $1/2$ and $1/5$ of the maximum peak height. The inset shows the T-dependence of the spin lattice relaxation rate, $1/T_1$. (right) The NMR spectrum measured for two delay times $\tau = 40\ \mu$s and $200\ \mu$s at $T = 0.35$ K. The locally ordered component appears as a square feature in the former spectrum. Both figures adapted from Bert. *et. al.* [Bert *et al.* (2005)].

Both J_1 and J_1' have historically been assumed to be antiferromagnetic. Attempts to fit the entirety of the χ versus T curve to exact diagonalisation results for the above Hamiltonian fail to provide an accurate description of data, although $\alpha = 1$ gives the best agreement between theory and experiment (figure 5.8) [Sindzingre (2007)]. Likewise, numerical results poorly reproduce the specific heat – a double peaked structure is predicted, but only one peak is observed experimentally. It is thus clear that the Hamiltonian is more complicated than first assumed. Indeed, determining its parameters remains one of the main challenges in unravelling the mystery of the ground state of volborthite.

Further experimental studies using ^{51}V NMR and μSR at temperatures down to 0.35 K reveal a slowing down of the fluctuations around $T^* \sim 1$ K [Bert *et al.* (2005)],[Bert *et al.* (2004)] (figure 5.9). The time-integrated NMR lineshape measured below this temperature is complex, containing several contributions, which can be partly resolved by applying a pulse sequence of the form $\pi/2 - \tau - \pi/2$, where τ is a delay on the order of μs (figure 5.9). The quickly relaxing component, which is probed by a delay time $\tau = 40\ \mu$s, is dominated by a square signal, implying local order on the NMR timescale. From the magnitude of the local field generated by the 6 Cu ions surrounding the ^{51}V site, this order is speculatively assigned as being of the $\sqrt{3} \times \sqrt{3}$ type. The slower component, isolated using a longer $\tau = 200\ \mu$s, effectively reflects a disordered local environment. The approximate ratios of these two contibutions are $40\% : 60\%$, meaning that the bulk of the sample remains disordered to the lowest temperatures.
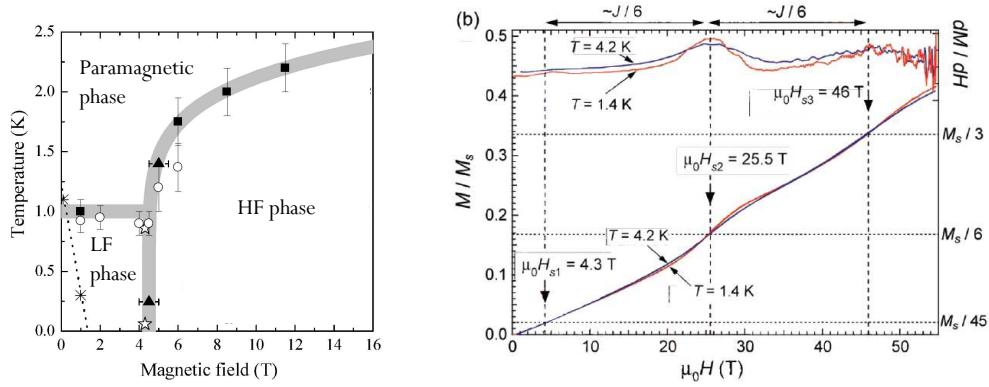
Figure 5.10: (left) H-T phase diagram of volborthite. The full squares and triangles represent the onset of freezing as detemined from line broadening, whilst the circles show the position of the peak in $1/T_1$. The stars indicate the onset of hysteresis in the magnetic susceptibility associated with a small impurity phase. Figure adapted from Yoshida *et. al.* [Yoshida *et al.* (2009b)]. (right) M vs H isotherms for volborthite measured up to 55 T at 1.4 K and 4.2 K. dM/dH shows clear kinks at at $H_{s1} = 4.3$ T, $H_{s2} = 25.5$ T, and $H_{s2} = 46.0$ T below T^*. The magnetizations corresponding to these fields are approximately 1/45, 1/6, and 1/3, respectively. Figure adapted from Yoshida *et. al.* [Yoshida *et al.* (2009a)].

Extending the low T ^{51}V NMR measurements to higher applied fields reveals a phase transition between different local orders at approximately $H_c = 4.5$ T (figure 5.10) [Yoshida *et al.* (2009b)]. The lineshape at $H < 4.5$ T is anomalous, suggesting a complex order, whilst above H_c it becomes more conventional. No assignment of either order is made however. High field magnetization results echo these results, revealing a small step in the magnetization at $H_{s1} = 4.3$ T $\sim H_c$, and a further two such steps at $H_{s2} = 25.5$ T and $H_{s3} = 46.0$ T (figure 5.10) [Yoshida *et al.* (2009a)]. The magnetizations corresponding to the latter two are rather close to 1/6 and 1/3, respectively, and suggest the possibility of several magnetization plateaux.

Despite potentially providing the ultimate insight into the structure and dynamics of voborthite, no neutron scattering studies have been reported thus far.

5.3.3 xyz Polarised Diffuse Neutron Scattering

Looking more closely at the formula of volborthite, the reason why neutron scattering experiments have not been attempted becomes clear: the presence of V ($\sigma_{inc} = 5.08$ barns) and H ($\sigma_{inc} = 80.26$ barns) means that any experiment on this compound is likely to suffer from a large incoherent background. In order to partially circumvent
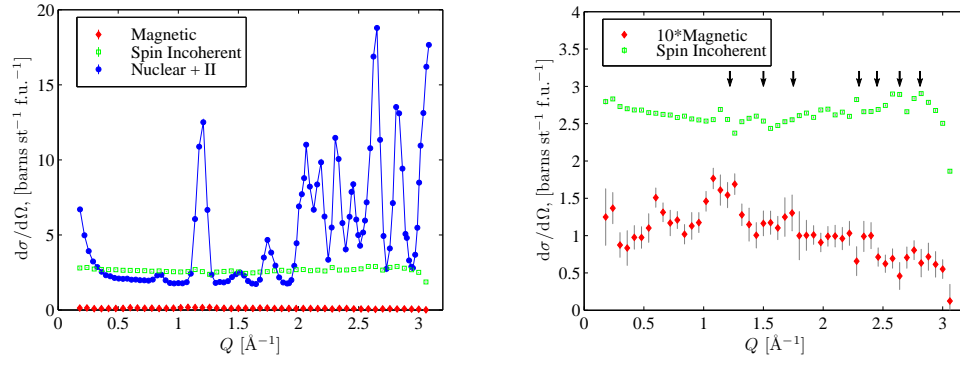
Figure 5.11: (left) The nuclear and isotope incoherent (blue), spin incoherent (green), and magnetic cross sections (red) for a powder sample of volborthite, measured at 5 K. The magnetic signal corresponds to about 1% of the nuclear and incoherent cross sections combined. (right) The spin incoherent cross section and magnetic cross section multiplied by 10. Positions of nuclear Bragg peaks are marked with black arrows, and coincide with regions in which the spin incoherent cross section deviates from flatness. It is expected this also has some effect on the magnetic cross section, especially at $Q > 1.7$ Å^{-1}.

this problem, it is necessary to substitute as much of the hydrogen in the sample as possible for deuterium. Details on how this was achieved are given in Appendix A.

In the case of magnetically disordered materials like volborthite, a particularly useful technique to probe $\langle S_i S_j \rangle$ is xyz polarised neutron scattering. The underlying principles of this method were briefly introduced in Chapter 3. Experiments on volborthite were performed on the D7 instrument at the ILL facility: 35.7g of deuterated volborthite powder were loaded into a Cu can, which was mounted on the end of a dilution refrigerator, allowing access to temperatures down to 50 mK. Spectra were measured at $\lambda = 3.1$Å^{-1} ($E_i = 8.5$ meV), yielding an integrated energy window of $-\infty < \omega < 7.2$ meV. Flipping ratio, background, and detector efficiency corrections were performed using quartz, cadmium, and vanadium, respectively. Spin flip and non spin flip cross sections were measured for three orthogonal polarisations of the beam at temperatures of between 300 mK, 5 K, 10 K, 15 K, and 200 K. The nuclear and isotope incoherent $[(d\sigma/d\omega)_{nuc+II}]$, spin incoherent $[(d\sigma/d\omega)_{SI}]$, and magnetic $[(d\sigma/d\omega)_{mag}]$ cross sections were separated using xyz polarisation analysis. The three cross sections are shown in figure 5.11 for the 5 K dataset.

Despite the high deuteration level of the sample, estimated to be $> 98\%$ from the spin incoherent cross section, the nuclear/isotope incoherent and spin incoherent cross sections dominate the rather small magnetic cross section. In fact, the sum of the average magnitudes of the former two dwarfs the latter by nearly two orders of magnitude.
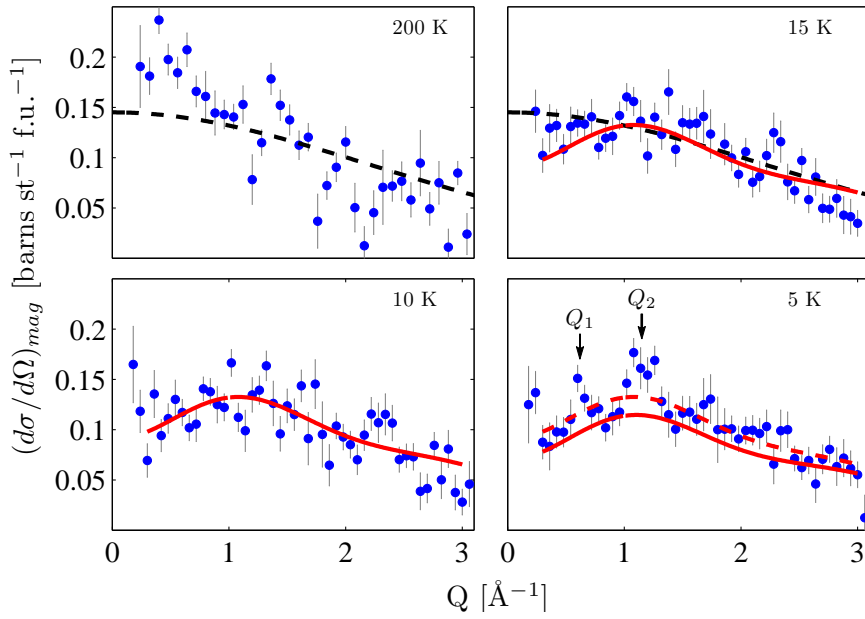
Figure 5.12: The magnetic cross section of volborthite at 200 K, 15 K, 10 K, and 5 K. At high T, the effect of correlations are already visible — the magnetic cross section does not obey the Cu^{2+} $f^2(Q)$ (dotted black line). At 15 K and 10 K, there is a buildup of correlations leading to a peak around $Q = 1.1$ Å^{-1}, also observed as a broad maximum in $S(Q, \omega)$ (figure 5.14). This is well described by a liquid-like structure factor (red line) superimposed on a paramagnetic background. At 5 K, some spectral weight moves from this feature into two sharp peaks at $Q_1 = 0.65(3)$Å^{-1} and $Q_2 = 1.15(5)$Å^{-1}.

This has several implications: when isolating the magnetic cross section via the spin flip route, the large error bars on the spin incoherent cross section reduce the statistical quality of the resulting magnetic data. Secondly, any uncertainty in the flipping ratio correction means that non spin flip scattering can "bleed" into the spin flip channel. Assuming an error in the flipping ratio of only 0.1%, nuclear Bragg peaks will appear in the spin flip scattering with a greater intensity than the magnetic scattering. Such errors may also be observed in small deviations from flatness in the spin incoherent scattering (figure 5.11). As this issue particularly affects the data at $Q > 1.7$ Å^{-1}, the behaviour of the spectrum at lower Q will be emphasised during the analysis.

The magnetic cross sections at 5 K, 10 K, 15 K, and 200 K are shown in figure 5.12. At 200 K $\sim 2\theta$, $(d\sigma/d\Omega)_{mag}$ only crudely obeys the Cu^{2+} form factor, $f(Q)^2$, indicating that some correlations may be present even at this temperature. In addition, the integrated magnetic scattering corresponds to only 40(3)% of the value expected from the neutron scattering sum rule $\int S(Q)_{mag}dQ \sim S(S+1)$, implying that much of the magnetic scattering lies outside the Q and ω window of the experiment. Indeed, magnetic
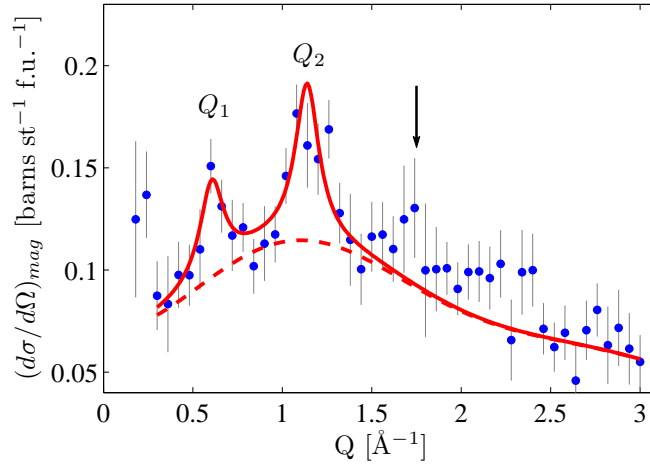
Figure 5.13: The 5 K magnetic cross section with fit (red line) as described in the text. The diffuse background is shown by the dotted line. The black arrow indicates the position of the 1.7 Å^{-1} feature.

correlations would be expected to distribute spectral weight up to the spin wave zone boundary energy, which corresponds to $2J$ for a bipartite antiferromagnet with $z = 4$, and $4J$ for a ferromagnet. Both of these energies are greater than the experimental $\omega_{max} = 8.2$ meV $\sim J$. Nonetheless, due to the large value of the shortfall, it may not be excluded that a proportion may be due to oversubtraction in the polarisation analysis.

As T is reduced to 15 K, the to 10 K, the spectral weight at low Q moves into a broad feature centered at $Q \sim 1.1$ Å^{-1}, consistent with the presence of short range correlations. This feature is well described by a structure factor of the form:

$$Af(Q)^2 \left[1 - \frac{\sin{(Qr)}}{(Qr)} \right] + Bf(Q)^2 \tag{5.4}$$

where the first term describes short range antiferromagnetic corrlelations at a distance $r = 3.5(2)$ Å^{-1}, approximately the Cu-Cu nearest neighbour distance ~ 3 Å. The second term corresponds to effectively uncorrelated spins. The amplitudes A and B are found to be 0.050(5) and 0.090(5), respectively, and may correspond to contributions from the two different Cu sites. The broad feature is also observed in the inelastic spectrum, as will be seen later in this chapter.

At $T = 5$ K, some of the spectral weight shifts into two additional sharper features at $Q_1 = 0.65(3)$Å^{-1} and $Q_2 = 1.15(5)$Å^{-1}, consistent with short range magnetic order. It is difficult to determine whether these correspond to $2D$ or $3D$ correlations, as the peaks are weak, and the background poorly characterised. There is also a feature at 1.7 Å^{-1} which is disregarded in the upcoming analysis, as it occurs in the position of

a nuclear Bragg peak. Fitting the Q_1 and Q_2 peaks to a Lorentzian convoluted with instrumental resolution yields a correlation length $\zeta = 1/\Delta Q = 12(4)$ Å, where ΔQ is the FWHM of the Lorentzian. This corresponds to ~ 4 nearest neighbour Cu-Cu distances.

The temperature at which the Q_1 and Q_2 peaks appear is considerably higher than the $T^* = 1$ K found from NMR. This is most likely an effect of the different timescales which neutron scattering, NMR, and μSR respectively probe. While neutrons are sensitive to correlations on the picosecond (10^{-12}s) timescale, μSR and NMR are only able to detect spins fluctuating more slowly than approximately ns or μs. Thus, neutron can follow the buildup of correlations to much higher temperatures than resonance techniques.

5.3.4   Inelastic Time of Flight Neutron Scattering

To investigate the excitations of the low temperature phase, thus hoping to gain insight into the nature of the ground state, inelastic neutron scattering studies were carried out on the IN4 instrument at ILL. A 10 g part of the sample that was used for the D7 experiment was loaded in a Cu can, then mounted on a dilution refrigerator. Spectra were collected at $T = 0.05$, 0.5, 5, 50 K using an incident energy $E_i = 17.2$ meV, giving an elastic Q range 0.65 Å$^{-1} < Q < 4.95$ Å^{-1}. One further spectrum was collected at 1.7 K using the MARI instrument at ISIS ($E_i = 15$ meV, 0.45 Å$^{-1} < Q < 4.95$ Å^{-1} at $\omega = 0$ meV). Data from these experiments are summarised in figure 5.14.

The 50 K ($\sim J_{avg}/2$) scattering function $S(Q, \omega)$ shows only a broad quasielastic response centered at $Q = 1.1 - 1.4$ Å^{-1}, characteristic of a correlated paramagnet – this feature was also observed in the energy integrated data at $T < 15$ K. Fitting with a near neighbour $S(Q)$ yields a characteristic lengthscale $r = 3.5(2)$ Å$\sim r_{nn}$, also consistent with previous findings (figure 5.15(a)). Acoustic phonons are observed dispersing from nuclear Bragg peak positions at $Q > 2$ Å^{-1} and intense phonon scattering is found above 7 meV, making extraction of the magnetic signal at these energies difficult. When T is lowered to 5 K (the temperature at which the Q_1 and Q_2 features are seen in the energy integrated data), the low Q quasielastic intensity has largely moved into two features: an intense broad flat band, centered at $\omega_0 = 5$ meV, and a vertical bar of scattering at $Q = 1.1$ Å^{-1}, which coincides with the Q_2 peak in the D7 data. Both features intensify and sharpen as temperature is reduced towards 0.05 K, and a second vertical bar of scattering appears around $Q = 0.7$ Å^{-1} at 1.7 K, approximately corresponding to the Q_1 feature in the energy integrated data.

Several cuts through the main features observed in the spectra are shown in figure
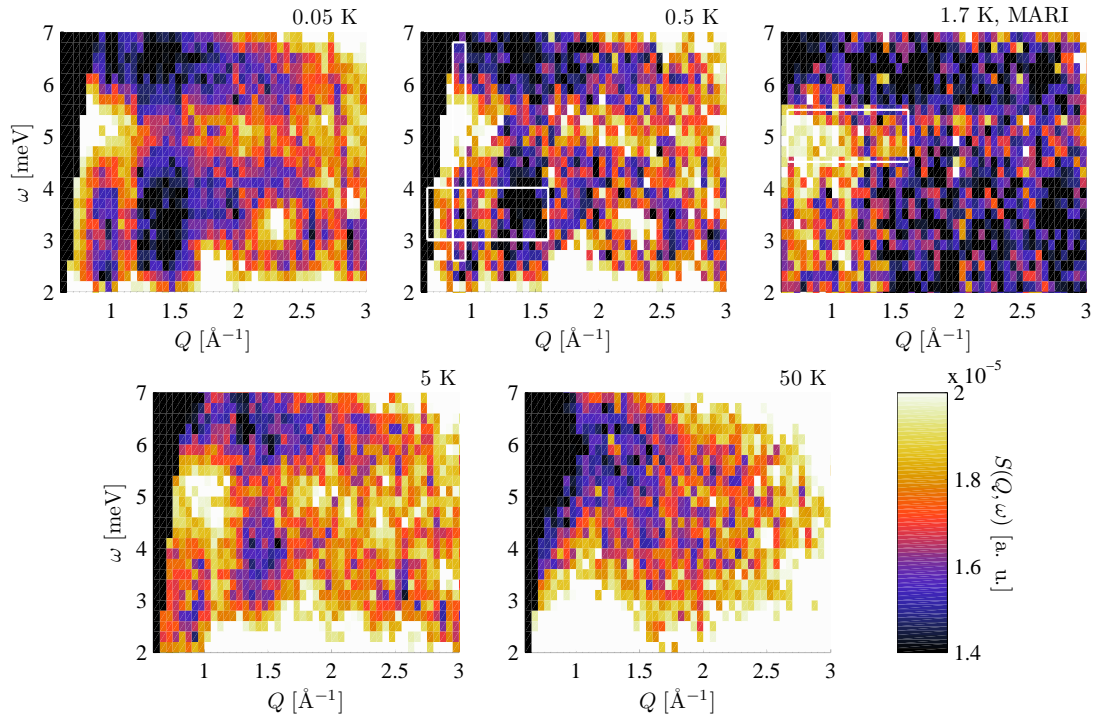
Figure 5.14: Inelastic time of flight spectra for volborthite collected on the IN4 and MARI (top right) instruments. The white rectangles indicate regions of integration for the cuts. At high T, the magnetic part of the spectrum is dominated by a broad quasielastic feature.

5.15. All the features observed (flat band and vertical bars) were fitted resolution convoluted Lorentzians. Starting with the ω dependence of the flat mode integrated between $Q = 0.8$ Å^{-1} and $Q = 0.95$ Å^{-1}, a considerable narrowing of the linewidth is observed upon cooling from 5 K to 0.05 K, implying an increase in the excitation lifetime. Likewise, the Q dependence of the two vertical bars, integrated between 2 and 3 meV, shows a narrowing, corresponding to a growing dynamical correlation length. Both of these quantities appear to saturate below T^*, though only two datapoints are available in this temperature range (figure 5.15(d)), consistent with the system approaching, then passing through a phase transition. The relative intensities of the Q_1 and Q_2 bars also change as the sample is cooled, with Q_1 becoming the more prominent of the two as T is lowered. Due to the long wavelength of this excitation, it is more sensitive to the correlation length than the Q_2 mode, possibly explaining this behaviour. As such, the jump in the intensity of Q_1 at T^* may be interpreted as a sign of a jump in the correlation length, consistent with a phase transition.
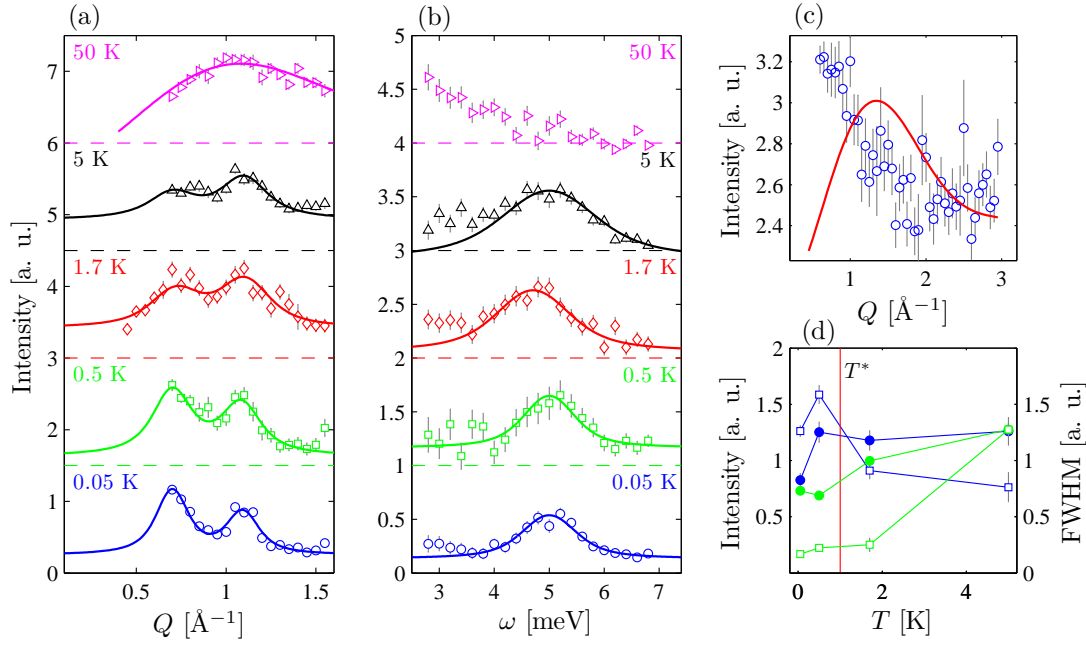
Figure 5.15: Temperature dependence of selected cuts through the inelastic data. Fits to resolution convoluted Lorentzians are shown by solid lines. For the 50 K dataset, the fit is instead made for a powder averaged, liquid like $S(Q)$. Baselines of the spectra are represented by a dotted line. (a) Cuts of the Q-dependence of the vertical bars as temperature is lowered. (b) Cuts of the ω-dependence of the flat mode. (c) Q-dependence of the flat mode from MARI at 1.7 K. The solid line shows the powder averaged structure factor anticipated for a singlet-triplet excitation. (d) The temperature dependence of the ω-linewidth of the flat band (open green squares), the Q-width of the vertical bars (closed green circles), and the intensities of the Q_1 and Q_2 bars of scattering (closed blue circles and open blue squares), respectively.

5.3.5 The Quest for a Microscopic Model

It is obvious that neither the excitation spectrum nor the low-T diffuse scattering match the predicted spectra for the VBC ground state expected for the pure KHAFM. Likewise, the flat band cannot be explained by local excitations from singlets pinned by vacancies [Dommange *et al.* (2003)]. Although the energy scale $\mathcal{O}(J_{avg})$ seems consistent, the Q-dependence, expected to follow that of a singlet-triplet excitation, is different (figure 5.15(c)). Instead, the data appear to point towards semi-classical order, as also implied by NMR measurements. It is however difficult to identify whether it is long or short range, mainly due to the absence of $(d\sigma/d\Omega)_{mag}$ data at $T < T^*$, and indeed also the nature of spatial correlations. As such, candidate models must be compared with all available data, both from resonance experiments and neutron

scattering, before a positive identification can be made.

The Hamiltonian which has so far been assumed for volborthite is the AKAF with α close to unity. The correlations in the classical analogue of this model are expected to be predominantly of the $\sqrt{3} \times \sqrt{3}$ type, and, indeed, this is the state suggested to describe the local order observed in NMR experiments [Bert *et al.* (2005)]. Do the static and dynamic properties of this state match our neutron results, however?

The elastic (static) structure factor, $S(\tau, \omega = 0)$, is written:

$$S(\tau, \omega = 0) = \langle S^z \rangle f(\tau) \sum_{\mathbf{d}} \sigma_{\mathbf{d}} e^{i\tau \cdot \mathbf{d}}$$

(5.5)

where τ is a magnetic Bragg vector and the sum runs over all the atoms in the unit cell. Powder averging this, the quantity which results, $S(Q, \omega = 0)$, roughly approximates the instantaneous scattering function, $S(Q) \sim (d\sigma/d\Omega)_{mag}$. Figure 5.16 shows that agreement between calculation and experiment for the $\mathbf{q} = \sqrt{3} \times \sqrt{3}$ state is rather poor. Likewise, the experimentally determined dynamical structure factor can not be satisfactorily described by a $\mathbf{q} = \sqrt{3} \times \sqrt{3}$ ordering pattern – the spin wave spectrum for such an ordering would be expected to result in a Goldstone mode at $Q = 1.4$ Å, as well as a flat band of scattering at $\omega_0 = 0$. Thus, it is necessary to look theoretically further afield to explain the observed scattering, as well as the other experimental observations:

- **QKHAF with DM interactions**: As established already, adding a Dzyaloshinskii-Moriya term of magnitude $D > D_c = 0.1J$ to the QKHAF results in $\mathbf{q} = 0$ order. The finite DM interactions also result in the spin wave spectrum becoming gapped, with the flat mode lifted to an energy $\omega_0 = S\sqrt{6\sqrt{3}JD_z + 18D_z^2}$ proportional to the strength of the dominant out of plane D_z interaction [Elhajal *et al.* (2002)]. A DM interaction can thus provide a mechanism for both the short range ordering and finite ω of the flat band, although a relatively strong $D_z = 0.11J$ must be invoked. Allowing for this interaction, the experimental inelastic scattering at 5 K can be rather accurately reproduced by Monte-Carlo simulations of the CKHAF (figure 5.16) [Robert *et al.* (2008)] – both the flat mode and the bar of scattering at Q_2 are captured. $\mathbf{q} = 0$ short range order however fails to explain both the Q_1 bar of scattering observed both in the energy integrated and inelastic data at $T \leq 5$ K, and is also at odds with the NMR result, which implies a finite local field at the V site.
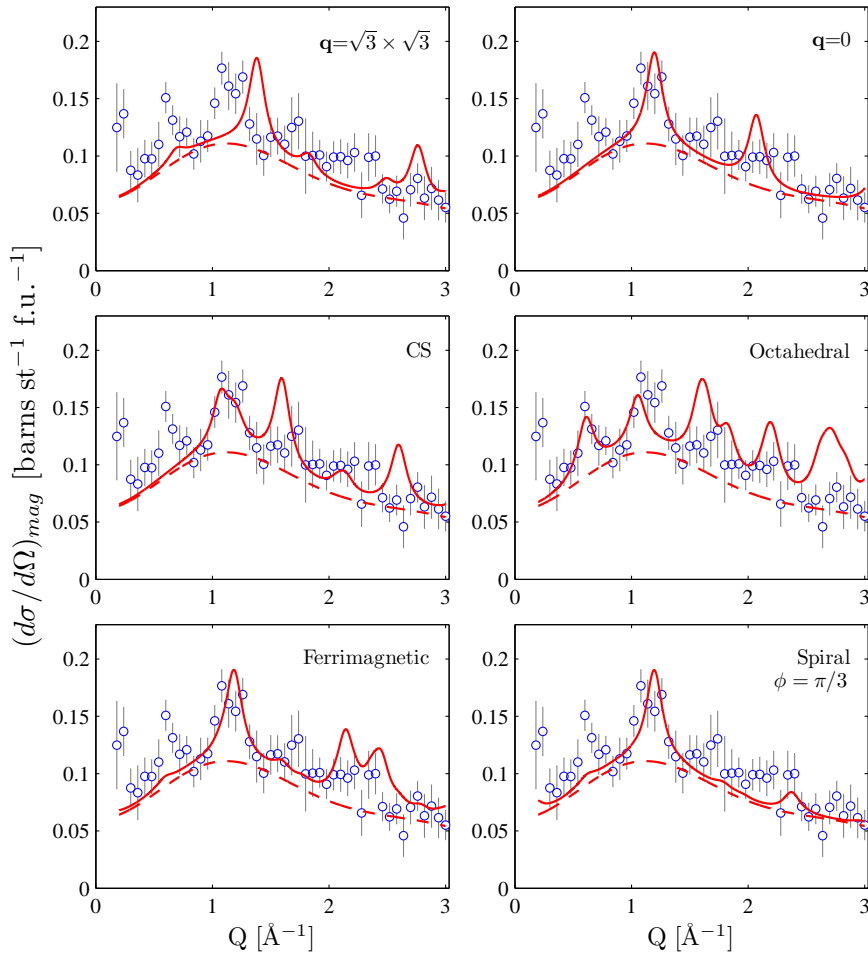
(a) The elastic (static) structure factor, $S(Q, \omega = 0)$, for a number of proposed orders for volborthite (see figure 5.2).
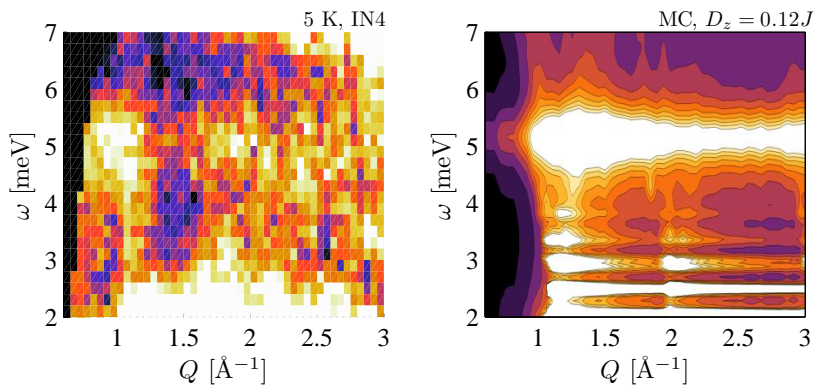
(b) (left) The 5 K $S(Q, \omega)$ measured on IN4. (right) The powder averaged $S(Q, \omega)$ from a classical MC calculation for the CKHAF with an out of plane DM interaction $D_z = 0.11J$ [Robert *et al.* (2008)]. Both the flat band at $\omega = 5$ meV and vertical bar at $Q \sim 1.1$ Å^{-1} are reproduced by the theory. Figure courtesy of Benjamin Canals and Julien Robert.

Figure 5.16

- **CKHAF with further neighbour couplings**: Messio [Messio (2010)] has recently suggested a further-neighbour interaction induced octahedral state as a possible source of the Q_1 and Q_2 features observed in diffuse and inelastic scattering experiments. The state is so called because it describes a 6-sublattice order, with the spins on each sublattice pointing towards the apices of an octahedron (figure 5.2). The requirement to favour the octahedral state is a large antiferromagnetic J_3', corresponding to interactions across the kagome hexagons, as well as small next nearest neighbour couplings J_2 and J_3 (figure 5.2).

  Within the octahedral state, it is possible to locally rearrange spins along lines in the lattice at no energy cost. Combining this with either a single ion or DM anisotropy, it may be possible account for the experimentally observed flat mode. The $B_{loc} = 0$ at the V site fails to explain the NMR results, however, and the balance of exchanges called for appear inconsistent with the orbital arrangement in volborthite.

- **The Janson-Rosner Model**: Janson *et. al.* [Janson *et al.* (2010)] have recently carried out *ab-initio* studies on volborthite using the L(S)DA+U method. The material is found to exhibit orbital order, as implied by its structure, in which the lone electrons on the Cu(1) and Cu(2) sites populate the $d_{x^2-y^2}$ and d_{z^2} orbitals, respectively. Mapping the calculated hopping integrals, t, onto a Heisenberg model ($J = 4t^2/U$), and keeping the most relevant terms, the Hamiltonian is written as follows:

$$\mathcal{H} = J_1 \sum_{<i,j>} \mathbf{S}_i \cdot \mathbf{S}_j + J_2 \sum_{<<i,j>>} \mathbf{S}_i \cdot \mathbf{S}_j + J_1' \sum_{<i,j>} \mathbf{S}_i \cdot \mathbf{S}_j \qquad (5.6)$$

where J_1 and J_2 are, respectively, the nearest and next nearest neighbour exchanges along the Cu(1) chains, and J_1' is the interaction coupling the Cu(1) and Cu(2) sites. J_1 is expected to be ferromagnetic, while J_2 and J_1' are both antiferromagnetic. Returning to the crystal structure of volborthite, the pattern of exchanges extracted from the *ab-initio* calculation is not entirely surprising, considering the bonding motif along the b direction. As pointed out earlier, the bond angles between nearest neighbouring Cu(1) are close to 90°, which according to the Goodenough-Kanamori rules favours ferromagnetism, whereas the next nearest neighbouring Cu(1) bonds have Cu-O-O-Cu angles of close to 180°, implying antiferromagnetism.

The classical analogue of the above Hamiltonian has a rather simple phase diagram, with two phases: the first is a ferrimagnetic phase with all spins up along
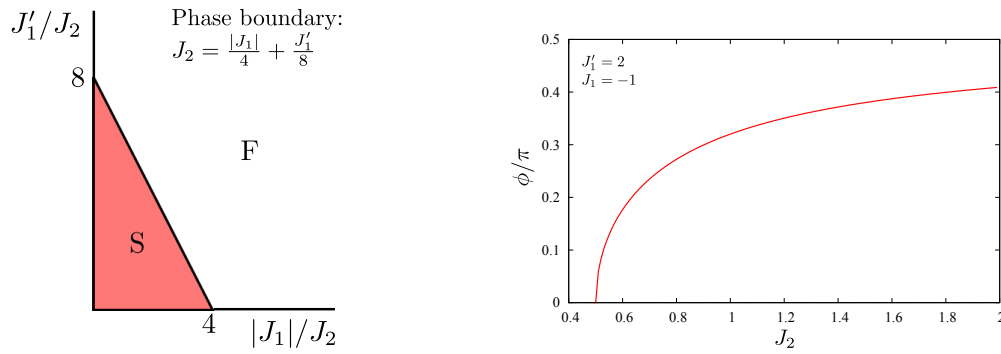
Figure 5.17: (left) The phase diagram of the $J_1 - J_1' - J_2$ model proposed for volborthite. S and F indicate spiral and ferrimagnetic states, respectively. (right) The dependence on J_2 of the pitch angle ϕ of the spiral state assuming $J_1 = -1$ and $J_1' = 2$. Volborthite is thought to have $J_2 \sim 1$, and thus $\phi \sim \pi/6$.

the $J_1 - J_1'$ chains and all spins down on the interchain sites, favoured when $J_2 < |J_1|/4 + J_1'/8$ (figure 5.2). The second is a spiral along the $J_1 - J_1'$ direction, with the pitch being the angle which minimises the following expression [Furukawa (2010)]:

$$E_{class} = \frac{NS^2}{3}\left[-2J_1'\cos\left(\phi/2\right) + J_1\cos\left(\phi\right) + 2J_2\cos\left(2\phi\right)\right] \tag{5.7}$$

Assuming J_1 is twice as small as J_1', as implied by the results of the *ab-initio* calculations, the dependence of the pitch angle on the third coupling, J_2, is shown in figure 5.17. This coupling was estimated to be approximately $0.6J_1$ in the aforementioned study, resulting in a pitch angle $\phi = \pi/6$. The classical ground state for this ϕ is illustrated in the bottom right of 5.2.

The fit of the calculated $S(Q, \omega = 0)$ for the spiral state to the experimentally measured $(d\sigma/d\Omega)_{mag}$ is shown in figure 5.16. While the Q_2 feature is reproduced in the calculation, agreement is poor otherwise. It is also difficult to reconcile the spiral state with NMR results – the local field, B_{loc}, at the V site for $\phi = \pi/3$ is only $1\mu_B$, too small by a factor of three compared to the B_{loc} found in [Bert *et al.* (2005)]. It remains to be seen whether such a state can generate the experimentally observed $S(Q, \omega)$.

5.4　Conclusion

Despite the considerable body of experimental data now available on volborthite, its ground state still remains somewhat mysterious. In the main, this is due to the lack of

a suitable candidate Hamiltonian to describe the system, although the Janson-Rosner model is an important step forward in this respect.

Although they provide insufficient information to completely clarify the issue of the ground state, experiments thus far carried out do set out a rather stringent list of requirements for any future candidates:

- **NMR, μSR**: The local field at the V site must correspond approximately to 3 μ_B. This is achievable within the Janson-Rosner model assuming a pitch angle α close to $\pi/2$, but at the expense of the structure factor matching diffuse scattering data. Within the pure kagome model, neither the $\mathbf{q} = 0$ or $\mathbf{q} = \sqrt{3} \times \sqrt{3}$ are able to explain both the NMR and diffuse scattering data. Finally, the octahedral model yields zero field at the V site, apparently discounting it as well.

- **Instantaneous Structure Factor**: Despite the poor statistical quality of the polarised diffuse scattering data, the proposed short range order should still produce peaks at both Q_1 and Q_2.

- **Excitation Spectrum**: The ground state, whether by the presence of a local mode in the ground state or via zone boundary effects of powder averaging, should be able to produce the flat mode observed in the inelastic neutron spectra.

- **Magnetization Steps**: The final test which a potential ground state of volborthite must be able to pass is to give steps in the magnetization curve, which contains several steps at nearly rational values of M/M_s.

5.5 Herbertsmithite

5.5.1 Herbertsmithite: The First Perfect $S = 1/2$ Kagome Material?

The (re)discovery of herbertsmithite, $Cu_3Zn(OH)_6Cl_2$, in 2005 brought to light the (ostensibly) first perfect realisation of the QKHAF [Braithwaite *et al.* (2004)],[Shores *et al.* (2005)]. The crystal structure is $R\bar{3}m$ symmetry, yielding perfect planes of CuO_6 octahedra arranged to form a kagome lattice, well separated by planes of nonmagnetic Zn (figure 5.18). Fits of the magnetic susceptibility to HTSE results indicated a J of approximately 190 K, yet no order down to 1.8 K. Nonetheless, the form of the susceptibility curve is not as anticipated for the QKHAF, with a large, Curie-like increase at low temperature (figure 5.19).

The initial paper on herbertsmithite was followed by a flurry of activity, both experimental and theoretical. Some of the experimental techniques which were applied
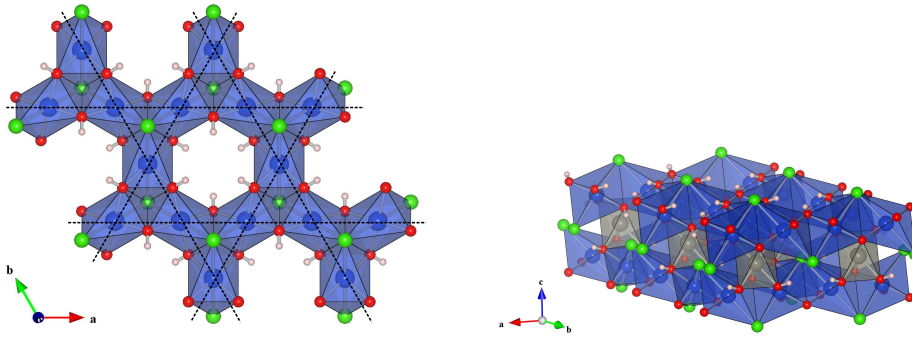
Figure 5.18: (left) The crystal structure of herbertsmithite viewed along the c-axis, showing the perfect kagome planes of CuO_6 octahedra (blue). The distances between nearest neighbour Cu atoms is 3.41 Å. (right) The stacking of the kagome planes. Two triangles on adjacent planes are linked via the grey interplane Zn site. This site is weakly coupled to the lattices.

include magnetic susceptibility (to 50 mK), specific heat, neutron diffraction [de Vries *et al.* (2008)], neutron spectroscopy [Helton *et al.* (2007)], NMR [Olariu *et al.* (2008)], and μSR. None of these probes were able to find any trace of long range order, despite the large value of J. Low temperature specific heat and neutron diffraction studies indicate that the $T \to 0$ upturn in χ is due to a small concentration ($\sim 6\%$) of free spins [de Vries *et al.* (2008)] (figure 5.19). These arise due to partial ($\sim 18\%$) occupation of the weakly coupled out of plane Zn^{2+} site by Cu^{2+} – as a consequence of this so-called anti-site mixing, the planes are also depleted by around 6%.

In light of the high defect concentration, it is difficult to see herbertsmithite as a lattice at all: at around 6% depletion, nearly every David's star making up the kagome lattice is missing a spin (figure 5.20). As noted in the introduction of this chapter, one effect of including a vacancy is to strongly enhance nearest neighbour correlations in its vicinity. In addition to the defects, ESR measurements by Zorko *et. al.* [Zorko *et al.* (2008)] have shown that the Dzyaloshinskii-Moriya interactions in herbertsmithite are also non-negligible. D_z was found to be the dominant component of $\mathbf{D}$, with a magnitude of $15(1)$ K$= 0.08J < D_c$, while D_{xy} was estimated to be $2(5)$ K$=0.01J$.

Bringing these two perturbations together, theoretical work on the kagome antiferromagnet with both defects and DM interactions was carried out using ED [Rousochatzakis *et al.* (2009)]. At $D < D_c$, the model is expected to show both dimerisation, due the presence of defects, as well as some restoration of some local moment, as a result of the finite DM interactions. In addition, the local susceptibility, as measured by NMR, is expected to be split in two components: the first is associated with nuclei close to defects, whilst the other results from more distant nuclei. Their relative intensities are
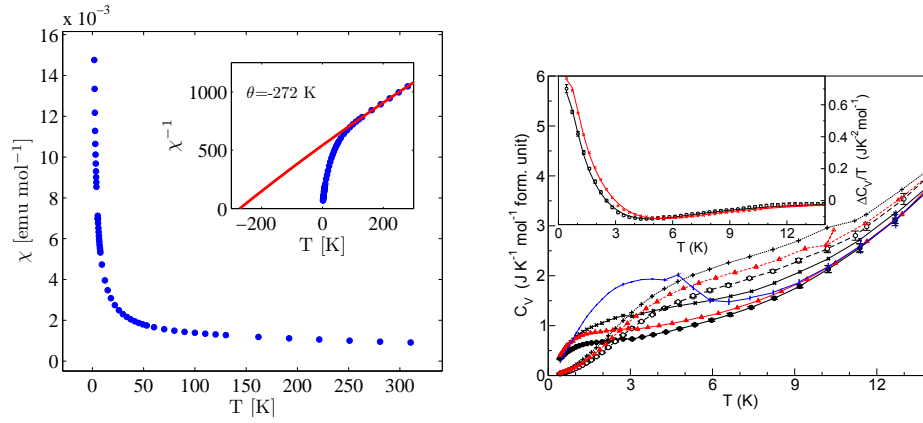
Figure 5.19: (left) The magnetic susceptibility of a representative sample of herbertsmithite measured from 1.8 K to 340 K at 100 Oe. (inset) The inverse susceptibility with Curie-Weiss fit (red line). (right) The specific heat for various compositions of herbertsmithite measured at temperatures down to 0.3 K at magnetic fields, $H = 0$ T and 9 T. The open and closed circles refer to the samples investigated in this study ($x = 1$), whilst the other curves are associated with Cu-rich ($x < 1$) and Cu-depleted ($x > 1$) samples. The low-T tail shown in the inset is interpreted as a Schottky anomaly corresponding to weakly coupled doublets.

expected to be around $1 : 5$. All of these features are observed in the T-dependence of the local susceptibility, χ_{loc}, as extracted from ^{18}O NMR experiments [Olariu *et al.* (2008)].

Now that the behaviour of the planes have been summarised, what happens to the interplane defect spins? These are only weakly coupled to the kagome planes, and thus the temperature scale at which they are expected to manifest themselves physically is low. Indeed, μSR and low temperature magnetization results imply a slowing down of these at around 1 K [Mendels *et al.* (2007)], [Bert *et al.* (2007)]. Little is known beyond this, however.

5.5.2 Diffuse and Inelastic Neutron Scattering

To elucidate the nature of the spin correlations in herbertsmithite, an xyz polarised diffuse scattering was performed on the D7 instrument at the Institut Laue Langevin. 20 g of highly deuterated ($\sim 98\%$), synthesised by Mark de Vries using the literature method [Shores *et al.* (2005)], were loaded into a Cu can which was then mounted at the end of a dilution refrigerator. Spectra were measured at temperatures of 0.1 K, 4 K, 10 K, and 60 K, though as with the aforementioned experiment, the lowest tem-
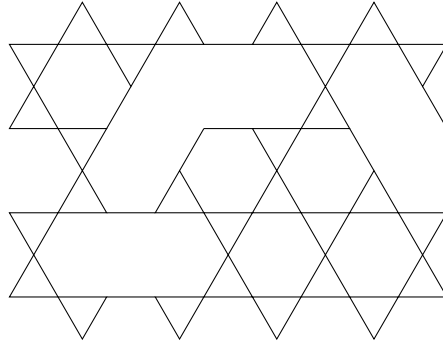
Figure 5.20: A 64 site lattice with 4 defects, corresponding to a defect population of 6.25%, approximately the same as an average sample of herbertsmithite.
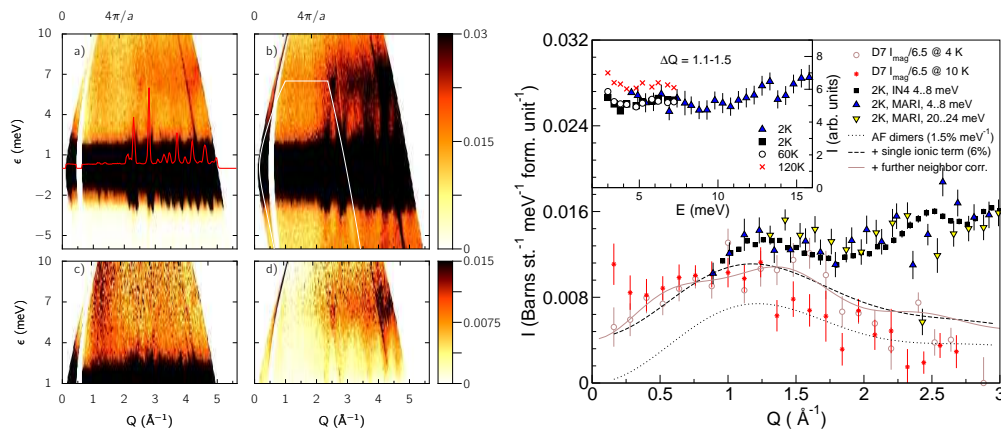

Figure 5.21: (top left) Inelastic spectra measured at $T = 2$ K and 120 K. (bottom left) The magnetic contribution to $I(Q, \omega)$ at 2 K extracted as described in the text. The main magnetic feature is the vertical bar of scattering at $Q = 1.3$ Å^{-1}. (right) Selected Q-cuts through spectra measured on the IN4 and MARI intstruments. For nearly all energy ranges, $S(Q)$ obeys the nearest neighbour antiferromagnetic structure factor (dotted line). Figures courtesy of Mark de Vries.

perature data had to be discarded due to oversubtraction in the polarisation analysis. The spectrum at low temperature looks rather similar to those observed for volborthite in the temperature range $10 - 15$ K – the main feature is a broad maximum at approximately 1.3 Å^{-1}, which is well approximated by the nearest neighbour antiferromagnetic structure factor (5.4).

The excitation spectrum of herbertsmithite was measured on the IN4 instrument at the ILL using the same sample as the diffuse scattering experiment. Spectra were collected at temperatures between 2 K and 120 K using an incident energy $E_i = 17$ meV. At $T = 120$ K $\sim 2J/3$ (figure 5.21), the spectrum consists of a broad phonon band at around 7 meV, several acoustic phonon modes dispersing from nuclear Bragg peak

positions at $Q > 2$ Å, and finally, a weak vertical bar of scattering at $Q = 1.3$ Å^{-1}, the same position as the maximum seen in $(d\sigma/d\Omega)_{mag}$. This bar of apparently magnetic scattering extends from the tail of the incoherent quasi-elastic scattering at ~ 2 meV, to the maximum ω measured, 10 meV. It cannot correspond to the excitations of the 36-sublattice VBC, as this is only expected to yield scattering at $T \sim 0.1J$ [Singh (2010)]. Furthermore it does not change appreciably in either intensity or sharpness as T is decreased to 2 K.

As the magnetic scattering appears independent of T, the magnetic component can be separated from the phonon background by assuming a Bose factor temperature dependence for the intensity of the latter. The T-dependence of the total intensity for each pixel in the spectrum, I_{tot}, can thus be fitted to the following expression:

$$I_{tot}(Q, \omega; T) = I_{mag}(Q, \omega) + \frac{\pi}{1 - e^{-\omega/k_B T}} \chi_p''(Q, \omega) \tag{5.8}$$

where χ_p'' is the dynamical susceptibility of the phonons.

The $I_{mag}(Q, \omega)$ which results from subtracting the phonon component from I_{tot} is shown in figure 5.21: The vertical bar at $Q = 1.3$ Å^{-1} is, as expected, greatly enhanced versus the background. Cuts of its Q-dependence integrated over several ranges in ω reveal that it is well described by a nearest neighbour antiferromagnetic structure factor at all ω, in agreement with the energy integrated $(d\sigma/d\Omega)_{mag}$. What then is the origin of this column of scattering?

The ground state and dynamics of the $S = 1/2$ Heisenberg model on the depleted kagome lattice have recently been studied by Singh using a dimer series expansion approach. At a high concentrations of defects, the 36-sublattice VBC breaks down, and is replaced by a valence bond glass (VBG) state, where the singlets are frozen in a pattern determined by the location of the defects [Singh (2010)]. The excitations of this state are gapped rearrangements of dimer bonds on networks of corner sharing triangles. Such processes result in an $S(Q, \omega)$ which features a continuum of scattering in ω with the Q-dependence of the nearest neighbour antiferromagnetic structure factor (see figure 5.22), in qualitative agreement with experiment. The temperature at which the system crosses over into the singlet ground state again reflects the defect concentration – spins which lie close in space to a defect, where the enhancement of $\langle S_i S_j \rangle$ is large, will dimerise at $T \sim J$, while the crossover temperature of more remote spins will be broadly distributed over $0.1J < T < J$. Given the high concentration of defect spins in herbertsmithite, it is expected that most spins are within a few nearest neighbour distances of a defect, hence the near lack of T-dependence in $I_{mag}(Q, \omega)$.
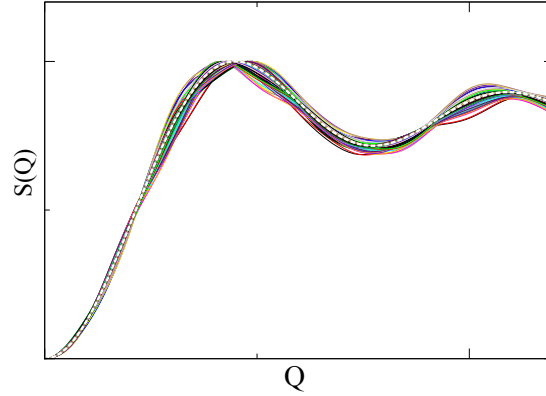
Figure 5.22: The structure factor, $S(Q)$, at various values of ω, scaled to the nearest neighbour antiferromagnetic structure factor (shown as a dashed white line). Adapted from Singh [Singh (2010)].

5.5.3   Low Energy Inelastic Neutron Scatteing: Probing the Defect Physics of Herbertsmithite

Having established that the inelastic spectrum at large $\omega > 2$ meV can be described as resulting from formation of a VBG state on the kagome planes, it remains to be seen what happens to the defect spins at $T < T_f = 1$ K, the slowing down temperature observed in μSR. To this end, neutron scattering was carried out on the IN5 cold neutron triple axis spectrometer at the ILL. Spectra were measured at a wavelength of 7 Å(elastic Q-range: 0.27 Å^{-1} $< Q <$ 1.45 Å^{-1}, ω-range: $\omega_{max} = 1$ meV$> \omega > -\infty$), and at two temperatures, 1.7 K and 10 K. At the lower temperature, measurements were performed in both zero field, as well as in applied fields of $H = 1.5$ T, 2.5 T. A background spectrum taken at 5 K was subtracted to yield the plots of $S(Q,\omega)$ shown in figure 5.23.

At 10 K$>> T_f$, $I(Q,\omega)$ is rather featureless, showing only a Lorentzian tail characteristic of a correlated paramagnet. It is difficult to confirm the presence (or absence) of the continuum of scattering seen at $Q = 1.3$ Å^{-1} in the higher E_i data, mainly because it falls on the edge of the (Q,ω) window of the experiment. At $T = 0.05$ K$< T_f$, the spectrum reveals a broad feature centered at approximately $\omega = 0.2$ meV. This energy agrees well with the zero field splitting of the interplane spins, $\Delta E = 1.7$ K~ 0.15 meV, as predicted from fits of the Schottky anomaly in C_p [de Vries *et al.* (2008)]. As such, the observed feature may be tentatively assigned to excitations of these weakly coupled Cu^{2+} ions. The Q-integrated energy dependence of the feature is found to be rather
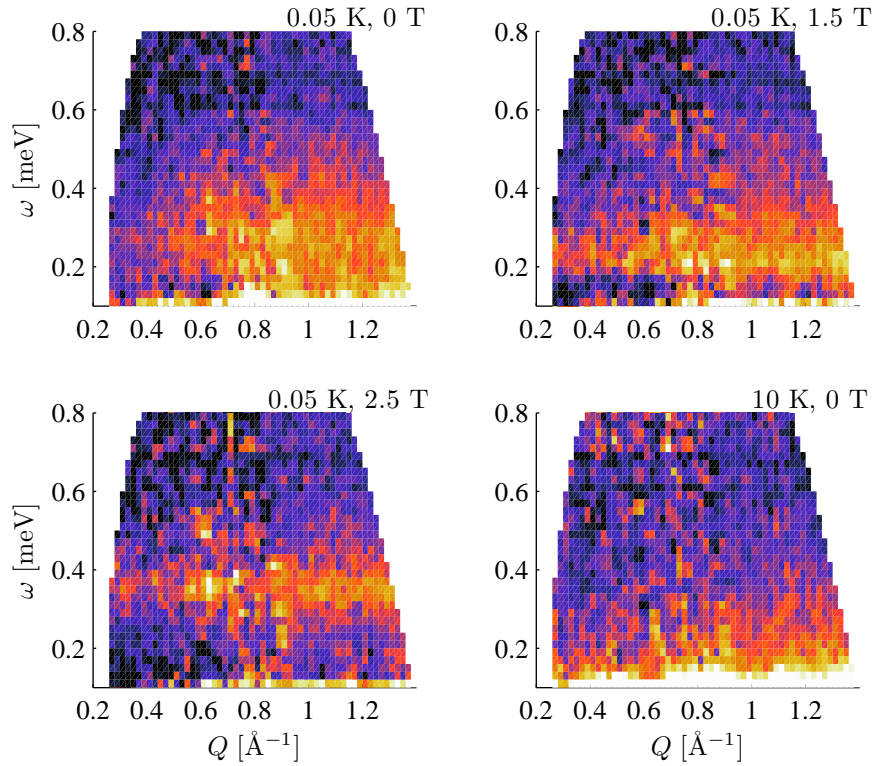
Figure 5.23: Background subtracted inelastic neutron scattering spectra for herbertsmithite collected on the IN5 spectrometer. The high temperature (10 K), and three base temperature spectra in different fields (0 T, 1.5 T, 2.5 T) are shown.

broad, reflecting both the Gaussian distribution of local environments indicated by the aforemention fits, as well as the finite lifetime of the excitations.

One question which logically follows from the assigned origin of the feature is; what do the interplane spins interact with? The Q-dependence of the feature integrated in the range $\omega = 0.2 < \omega < 0.4$ meV (figure 5.24) shows a broad peak at $Q = 1.1$ Å^{-1}. This is, yet again, well fit to a liquid-like stucture factor of the form $S(Q) \sim 1 - \sin{(Qr)}/(Qr)$, with $r = 4.0$ Å. It is difficult to match this distance to any specific Cu-Cu distance in the structure of herbertsmithite, though it is clearly much shorter than that between two interplane spins, $r_{int} = 6.1$ Å. Thus, the coupling which leads to the zero field splitting must be between an interplane spin and some object on the planes – two possible candidates are defect spins, or small, Dzyaloshinskii-Moriya induced moments.

When a magnetic field of $H = 1.5$ T is applied, the spectrum changes drastically, with much of the spectral weight at $\omega < 0.2$ meV shifted up in energy and distributed over all Q. The latter effect can be observed in the flattening of the Q-dependence of the scattering integrated over the same region as before, as well as the reduced intensity of the broad feature. At $H = 2.5$ T, the feature becomes almost entirely flat in Q,
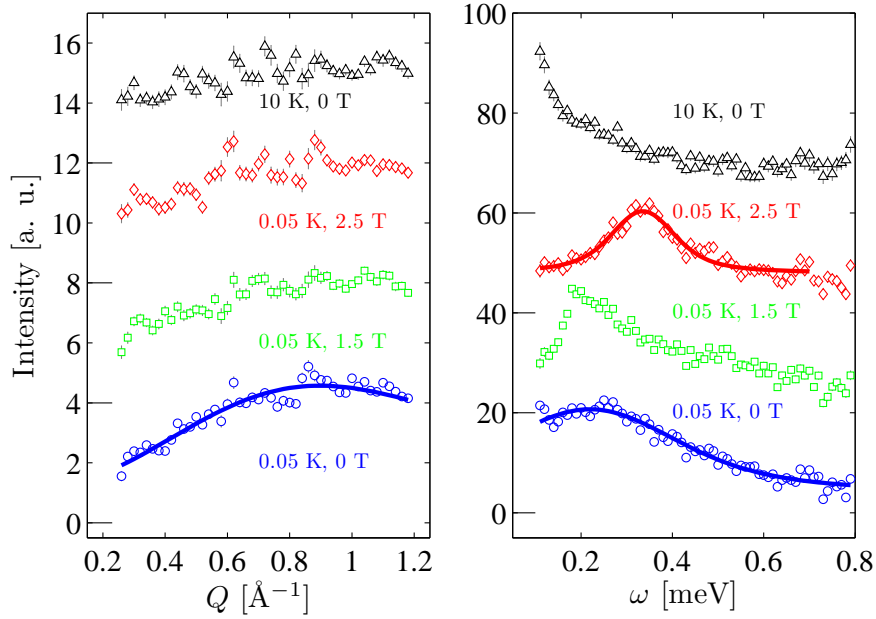
Figure 5.24: Cuts showing (left) the Q-dependence and (right) ω dependence of the broad feature observed in $S(Q, \omega)$ at various T and H. In the left panel, the solid line represents a fit to a short range antiferromagnetic structure factor. The large tickmarks on the y-axis represent the baseline of the spectra. The fits indicated by solid lines on the right are Lorentzians – the FWHM at $H = 0$ is 4 times that at $H = 2.5$ T.

and is considerably narrower in ω versus the $H = 0$ spectrum. Also, the position of the peak is shifted from 0.2 meV to 0.35 meV, which corresponds approximately to the Zeeman splitting $\Delta = 2g\mu_B SH = 0.34$ meV for $g = 2.2$. Such behaviour is consistent with a zero field split doublet system, in which the small internal field, B_{loc}, is gradually reoriented as an external field, H, is applied. Eventually, when H exceeds B_{loc} (i.e. when the zero field gap disappears), the splitting between up and down states is primarily due to H.

5.6 Why Volborthite and Herbertsmithite Both Fail As Realisations of the KHAFM

As was touched upon in Chapter 2, quantum ground states which emerge from the Heisenberg model are often sensitive to perturbing terms in the Hamiltonian. In the case of herbertsmithite, the large population of defects destroys the fragile 36-sublattice VBC, yielding a valence bond glass state instead. In volborthite, it turns out that the Hamiltonian describing the system is most likely rather distant from the nearest

neighbour Heisenberg model. As a consequence, the search for an ideal realisation of the QKHAF continues. A considerable barrier to the success of this endeavour is the omnipresence of yet another perturbation in kagome materials composed of metal octahedra: the Dzyaloshinkii-Moriya interaction. When octahedra are linked to form a kagome lattice, it is impossible to preserve bond inversion symmetry about the TM-O-TM bond, and therefore DM interactions are always allowed. In compounds where the magnitude of the DM interactions have been measured, values on the order of $0.1J$ are typically found, rather close to the theoretically predicted D_c for emergence of $\mathbf{q} = 0$ order. Thus, the challenge presented to chemists is to produce a material which not only realises the $R\bar{3}m$ symmetry of the kagome lattice, and is free of defects, but also minimises $|D|$. Clearly, there is still some distance to cover before all these goals are reached. On the other hand, volborthite and herbertsmithite, despite their imperfections, still reveal fascinating physics, and the author believes that many more interesting phenomena will be uncovered on the way to the ideal experimental QKHAF.

Chapter 6

Conclusion

This thesis has addressed several aspects of quantum magnetism, ranging from design and synthesis of new materials, to sophisticated neutron scattering experiments, to the interpretation of the results of these experiments in terms of modern condensed matter theory.

The main findings may be summarised as follows:

- **Titanium krausite, $KTi(SO_4)_2 \cdot (H_2O)$** – A new realisation of the $S = 1/2$ frustrated $(J_1 - J_2)$ Heisenberg chain model has been prepared by hydrothermal synthesis and studied by magnetic susceptibility, specific heat, low temperature ac susceptibility, and high field magnetization. These may all be interpreted in terms of a scenario where $\alpha = J_2/J_1 = 1.5$. Electronic structure calculations by Kasinathan *et. al.* support this picture, and furthermore identify the orientation of the water molecule bound to the the TiO_6 octahedron as important in determining the magnetically active orbital.

- **Titanium yavapaiite, $KTi(SO_4)_2$** – The anhydrous analogue of $KTi(SO_4)_2 \cdot (H_2O)$, $KTi(SO_4)_2$, has been synthesised by a novel hydrothermal route, resulting in samples of unprecedented purity. The magnetic susceptibility of this new sample implies that $KTi(SO_4)_2$ is, in fact, a realisation of the quantum Heisenberg chain model, rather than of the Ising triangular lattice antiferromagnet, as previously supposed [Bramwell *et al.* (1996)]. The new sample was used for low T inelastic time of flight experiments, which confirm the $1D$ nature of the system. Despite multiple scattering and powder averaging, good agreement is achieved between an exact result for $S(Q, \omega)$ of the 2-spinon continuum. The frustrating interchain interaction J' is shown to be non-negligible, however, by shifting the antiferromagnetic zone center away from the position expected for a purely $1D$ system

to the collinear antiferromagnetic structure proposed in [Starykh and Balents (2007)].

- **Volborthite, $Cu_3V_2O_7(OH)_2 \cdot 2(H_2O)$** – A highly deuterated sample of the $S = 1/2$ quasi-kagome antiferromagnet material volborthite was prepared and studied by XYZ polarised neutron scattering and inelastic time of flight neutron scattering. Whilst not entirely clearing up the mystery of the ground state, these considerably narrow down the list of possible candidates. The most promising model for explaining the experimental data is the so-called Janson-Rosner model, which features ferromagnetic-antiferromagnetic chains running along the a direction, coupled antiferromgnetically to the interchain sites.

- **Herbertsmithite, $Cu_3Zn(OH)_6Cl_2$** – When discovered in 2005, the mineral herbertsmithite was billed as the first structurally perfect realisation of the $S = 1/2$ Heisenberg kagome model. Subsequent specific heat and neutron diffraction experiments, however, showed that there is considerable mixing between the in-plane Cu^{2+} site and the interplane Zn^{2+} site. As a result, the kagome planes are depleted by 6%, and nearly 20% of the interplane sites are populated by Cu^{2+}. The effects of anti-site mixing are also reflected in our data: inelastic neutron scattering at high energy transfers shows a column of scattering at $Q = 1.3Å^{-1}$, which can be explained in the framework of a valence bond glass ground state. The low energy dynamics at $T < 1$ K are interpreted as implying that the interplane Cu^{2+} defects weakly couple to the kagome planes.

One thing all of the materials listed above have in common (beyond being quantum magnets, obviously), is that they are produced by hydrothermal synthesis. The high temperatures and pressures generated in such reactions make single crystal growth difficult, and the products are therefore usually powders [1]. The loss of spatial information which results from powder averaging presents a considerable challenge in interpreting experimental data, especially when looking for sometimes subtle quantum effects. Another feature shared by the above materials, and particularly the last two on the list, is the presence of (unavoidable) perturbing terms in the Hamiltonian. Quantum ground states are easily disturbed by such perturbations, a fact that is especially apparent in herbertsmithite. Solving these two issues are of key importance.

Beyond the material presented in the main body of this thesis, considerable efforts were also made in the area of metal-organic synthesis, in particular single crystal growth of

---

[1] Although some advances have been made in growth of herbertsmithite crystals, achieved by careful control of the temperature gradient across the reaction vessel. This has resulted in single crystals of about 1 mm^3.

$2D$ antiferromagnets such as Cu(N-pyridine oxide)$_6$(BF$_4$)$_2$[Carlin and DeJongh (1986)] and (CAP)$_2$CuCl$_4$ (where CAP is 5-chloro-2-aminopyridinium) [Coomer *et al.* (2006)]. Attempts were also made to modify the structure of the former, which resulted in the synthesis of 3 new materials.

Work from this thesis is published in the following articles:

- G. J. Nilsen, F. C. Coomer, M. A. de Vries, J. R. Stewart, P. P. Deen, A. Harrison, and H. M. Rønnow, arXiv:1001.2462, submitted to Phys. Rev. B.

- M. A. de Vries, J. R. Stewart, P. P. Deen, J. O. Piatek, G. J. Nilsen, H. M. Rønnow, and A. Harrison, Phys. Rev. Lett. **103**, 237201 (2009)

- G. J. Nilsen, H. M. Ronnow, A. M. Laeuchli, F. P. A. Fabbiani, J. Sanchez-Benitez, K. V. Kamenev, and A. Harrison, Chem. Mater. **20**, 8 (2008)

Several further publications are also in preparation on the high field and low temperature magnetic data for KTi(SO$_4$)$_2$·(H$_2$O), the excitation spectrum of KTi(SO$_4$)$_2$, and the low temperature defect physics of Cu$_3$Zn(OH)$_6$Cl$_2$.

Appendix A

Synthetic and Crystallographic Details

This appendix contains additional detail on synthetic protocol of the compounds discussed in Chapters 4 and 5, as well as details of the structure solution and refinement of $KTi(SO_4)_2 \cdot (H_2O)$.

A.1 $KTi(SO_4)_2 \cdot (H_2O)$

A.1.1   Synthesis

$KTi(SO_4)_2 \cdot (H_2O)$was prepared by first dissolving 0.965 g of K_2SO_4 (5.5 mmol, 99%, Sigma Aldrich) in approximately 21 ml of warm ($\sim 50°C$) deionised water under stirring. To this solution was added 10.5 ml (15.28 g, 40 mmol) of 45% v/w $Ti_2(SO_4)_3$ solution (40 mmol, Sigma Aldrich) and 2.1 ml of H_2SO_4 (40 mmol, 98%, Sigma Aldrich). 10 ml portions of the dark purple solution were pipetted into several 21 ml Parr instruments PTFE lined digestion bombs. The mixture was heated at 155°C for 48 hours, before being cooled to room temperature at a rate of approximately 5° per hour. Two of the bombs produced only a white powder, later identified as TiO_2. The third contained a mixture of small intergrown clusters of blue-violet crystals alongside a large amount of the same white powder. The product was collected by suction filtration, washed several times with water, and dried in a vacuum dessicator. When dry, the two phases present were separated by hand, easily accomplished due to the differing particle sizes. The final yield of the product, identified by single crystal X-ray crystallography as $KTi(SO_4)_2 \cdot (H_2O)$, was 0.11 g (1.5% with respect to Ti).

Subsequent attempts at reproducing the synthesis yielded only amorphous TiO_2 side-product. Efforts to improve the yield of $KTi(SO_4)_2 \cdot (H_2O)$ were thus mainly concentrated on preventing the oxidation of Ti^{3+} to Ti^{4+}: deoxygenating the solution, adding Ti metal, and varying the pH were all tried, but failed to to increase the yield. Changing the stoichiometry of the reagents to a ratio closer to the stoichiometry of the product also failed. Finally, the nucleation surface was varied by placing the reaction mixture in a small glass vessel designed to fit the PTFE bomb liner. This lead to to three more succesful syntheses, among nearly 144 attempts. To reliably reproduce the synthesis of $KTi(SO_4)_2 \cdot (H_2O)$ is the primary barrier standing in the way of neutron experiments, which would shed unprecedented light on the dynamics of the frustrated chain antiferromagnet.

A.1.2   Crystallographic Details

The crystal structure solution and refinement was carried out by Francesca Fabbiani. A crystal of dimensions $0.19 \times 0.15 \times 0.08$ mm^3 was selected for single-crystal diffraction. All data were collected at 150(2) K on a Bruker SMART APEX CCD diffractometer equipped with an Oxford Cryosystems low temperature ($\sim$ 80K) device. The structure was solved by direct methods and full matrix least-squares structure refinement against F^2 was performed using CRYSTALS. Non-hydrogen atoms were modeled with anisotropic displacement parameters. Hydrogen atoms were located on a difference map and their positions were refined subject to distance restraints. The coordination of water rather than hydroxyl was primarily inferred from magnetic susceptibility measurements, which confirmed the oxidation state of Ti as Ti^{3+}. Details concerning the crystal, measurement, refinement, atomic positions, displacement parameters, and bond lengths and angles are given in the following set of tables.

Crystal data	
KTi(SO$_4$)$_2$·(H$_2$O)	$\rho = 2.766$ g cm^{-3}
$M = 297.14$	Mo-k$_\alpha$ radiation, $\lambda = 0.71073$ Å
Monoclinic, $P2_1/m$	Cell parameters from 1401 reflections
Hall symbol: $-P2yb$	$\theta = 2.298° - 25.026°$
$a = 7.6593(6)$ Å	$\mu = 2.393$ mm^{-1}
$b = 5.2559(4)$ Å	$T = 150(2)$ K
$c = 9.0545(9)$ Å	Purple blocks
$\beta = 101.834(6)°$	$F(000) = 294$
$Z = 2$	$0.19 \times 0.15 \times 0.08$ mm^3

Data collection	
Bruker SMART diffractometer	701 independent reflections
Graphite monochromator	539 reflections with $I > 2\sigma(I)$
ω scans	$\theta_{max} = 2.298^{circ}$ $\theta_{min} = 25.026^{circ}$
Absorption correction: multi-scan	$R_{int} = 0.060$
SADABS (Siemens, 1996)	$h = -9 \rightarrow 9$
3379 measured reflections	$k = -6 \rightarrow 6$
	$l = -10 \rightarrow 10$

Refinement	
Refinement on F^2	2 restrains
Least-squares matrix: full	Primary atom location: direct methods
$R[F^2 > 2\sigma(F^2)] = 0.0353$	H-atom location: difference Fourier map
$wR(F^2) = 0.0978$	$w = \frac{1}{\sigma^2 F_o^2 + (0.0525P)^2 + 0.231P}$
697 reflections	where $P = \frac{F_o^2 + 2F_c^2}{3}$
78 parameters	$\Delta\rho_{max} = 1.78$, $\Delta\rho_{min} = -1.26$

Atom	x	y	z	U_{eq}	g
Ti	0.91347(16)	0.7500	0.76622(13)	0.0094	1.0000
O(1)	0.9134(7)	0.7500	0.5397(5)	0.0156	1.0000
K(1)	0.57212(19)	0.2500	0.21752(17)	0.0150	1.0000
S(1)	0.6645(2)	0.2500	0.64451(18)	0.0108	1.0000
O(11)	0.7270(4)	0.4785(6)	0.7411(3)	0.0119	1.0000
O(21)	0.7474(6)	0.2500	0.5138(5)	0.0142	1.0000
O(31)	0.4706(6)	0.2500	0.6091(5)	0.0157	1.0000
S(2)	1.1648(2)	1.2500	0.88488(17)	0.0084	1.0000
O(12)	1.1107(4)	1.0205(6)	0.7886(3)	0.0107	1.0000
O(22)	1.0626(6)	1.2500	1.0064(5)	0.0100	1.0000
O(32)	1.3548(6)	1.2500	0.9370(5)	0.0141	1.0000
H(1)	0.810(5)	0.7500	0.483(9)	0.0500	1.0000
H(2)	0.951(7)	0.901(6)	0.535(11)	0.0500	0.5000

Table A.1: Fractional atomic coordinates, isotropic displacement parameters, and occupancies for $KTi(SO_4)_2 \cdot (H_2O)$.

Atom	U_{11}	U_{22}	U_{33}	U_{23}	U_{13}	U_{12}
Ti(1)	0.0109(7)	0.0013(6)	0.0169(7)	0.0000	0.0054(5)	0.0000
O(1)	0.020(3)	0.013(3)	0.014(2)	0.0000	0.003(2)	0.0000
K(1)	0.0115(8)	0.0107(8)	0.0239(8)	0.0000	0.0062(6)	0.0000
S(1)	0.0121(9)	0.0036(8)	0.0171(9)	0.0000	0.0043(7)	0.0000
O(11)	0.0124(15)	0.0021(15)	0.0227(15)	-0.0022(11)	0.0071(12)	-0.0007(13)
O(21)	0.018(2)	0.004(2)	0.023(2)	0.0000	0.0109(18)	0.0000
O(31)	0.0119(16)	0.009(2)	0.027(3)	0.0000	0.0054(18)	0.0000
S(2)	0.0084(8)	0.0011(7)	0.0167(9)	0.0000	0.0048(7)	0.0000
O(12)	0.0124(15)	0.0026(15)	0.0188(15)	-0.0028(11)	0.0070(12)	0.0002(13)
O(22)	0.012(2)	0.002(2)	0.018(2)	0.0000	0.0067(17)	0.0000
O(32)	0.0083(16)	0.011(3)	0.024(3)	0.0000	0.0045(17)	0.0000

Table A.2: Anisotropic displacement parameters for $KTi(SO_4)_2 \cdot (H_2O)$.

Geometric parameters (Å,°)s			
Ti(1)-O(12)^a	2.054(3)	Ti(1)-O(22)^b	2.029(4)
Ti(1)-O(11)^a	1.999(3)	Ti(1)-O(1)	2.051(5)
Ti(1)-O(11)	1.999(3)	Ti(1)-O(12)	2.054(3)
O(1)-H(2)^a	0.849(10)	O(1)-H(1)	0.849(9)
O(1)-H(2)	0.849(10)	S(1)-O(11)	1.505(3)
S(1)-O(11)^a	1.505(3)	S(1)-O(21)	1.454(5)
S(1)-O(31)	1.453(5)	S(2)-O(12)	1.496(3)
S(2)-O(12)^a	1.496(3)	S(2)-O(22)	1.476(5)
S(2)-O(32)	1.434(5)		
O(12)^a-Ti(1)-O(22)^b	89.33(12)	O(12)^a-Ti(1)-O(11)^a	177.97(13)
O(22)^b-Ti(1)-O(11)^a	91.67(13)	O(12)^a-Ti(1)-O(1)	87.02(13)
O(22)^b-Ti(1)-O(1)	174.94(18)	O(11)^a-Ti(1)-O(1)	91.87(13)
O(12)^a-Ti(1)-O(11)	90.63(12)	O(22)^b-Ti(1)-O(11)	91.67(13)
O(11)^a-Ti(1)-O(11)	91.11(18)	O(1)-Ti(1)-O(11)	91.87(13)
O(12)^a-Ti(1)-O(12)	87.61(17)	O(22)^b-Ti(1)-O(12)	89.33(12)
O(11)^a-Ti(1)-O(12)	90.63(12)	O(1)-Ti(1)-O(12)	87.02(13)
O(11)-Ti(1)-O(12)	177.97(13)	H(2)^a-O(1)-Ti(1)	97(7)
H(2)^a-O(1)-H(1)	105.0(9)	Ti(1)-O(1)-H(1)	114(6)
H(2)^a-O(1)-H(2)	138(12)	Ti(1)-O(1)-H(2)	97(7)
H(1)-O(1)-H(2)	105.0(9)	O(11)^a-S(1)-O(11)	105.9(3)
O(11)^a-S(1)-O(21)	109.47(17)	O(11)-S(1)-O(21)	109.47(17)
O(11)^a-S(1)-O(31)	108.49(17)	O(11)-S(1)-O(31)	108.49(17)
O(21)-S(1)-O(31)	114.7(3)	Ti(1)-O(11)-S(1)	140.4(2)
O(12)^a-S(2)-O(12)	107.5(2)	O(12)^a-S(2)-O(22)	107.97(16)
O(12)-S(2)-O(22)	107.97(16)	O(12)^a-S(2)-O(32)	109.45(16)
O(12)-S(2)-O(32)	109.45(16)	O(22)-S(2)-O(32)	114.3(3)
Ti(1)-O(12)-S(2)	136.55(18)	Ti(1)^c-O(22)-S(2)	143.7(3)
Symmetry labels: (a) $x, -y + 1/2, z$, (b) $-x, y + 1/2, -z$, (c) $-x, -y, -z$			

Table A.3: Geometric parameters for KTi(SO$_4$)$_2$·(H$_2$O).

A.2 $KTi(SO_4)_2$

A.2.1   Synthesis

$KTi(SO_4)_2$ was prepared from the same reaction mixture as $KTi(SO_4)_2 \cdot (H_2O)$. The primary difference in the syntheses was the reaction vessel: instead of PTFE lined steel bombs, 35 ml glass pressure tubes (Ace Glass Co.) were used. After heating the reaction mixture for 48 hours at 155°C, it was cooled to room temperature at a rate of 10°C per hour. Due to the transparency of the tubes, it was possible to monitor the progress of the reaction throughout its entire duration. Formation of product was found to start after a period of approximately 18 hours, with the appearance of small, blue crystals on the walls of the tubes. White TiO_2 powder was also observed at this stage. After approximately 36 hours, it was difficult to discern any further precipitation of either phase, at least by eye, as the walls of the reaction vessel were entirely covered in material. The product was collected by suction filtration and washed several times with water, before being dried in a vacuum dessicator. The final yield of $KTi(SO_4)_2$ was found to be around 0.4 g per vessel, 7% with respect to Ti. The crystal structure was confirmed both by single crystal and powder X-ray diffraction, as well as SQUID magnetometry. The lattice parameters were found to be consistent with those stated by Bramwell *et. al.* [Bramwell *et al.* (1996)].

A.2.2   Crystallographic Details

The structure of Ti-yavapaiite was verified by performing powder X-ray diffraction at room temperature on a ground sample. A typical diffractogram with Rietveld refinement is shown in figure A.1. This was used to extract the lattice parameters quoted in the text.

A.3 $Cu_3V_2O_7(OH)_2 \cdot 2(H_2O)$

A.3.1   Synthesis of Deuterated Sample

The high level of deuteration required from neutron scattering experiments was achieved by performing the literature [Hiroi *et al.* (2001)] synthesis with modifications as follows: CuO (2.39 g, 30 mmol) was dissolved in approximately 30 ml of 1 M D_2SO_4 at ~ 60°C. A small overpressure of N_2 gas was maintained in the reaction vessel in order to avoid H/D exchange during the reaction. V_2O_5 (1.815 g, 10 mmol) was then slowly added to
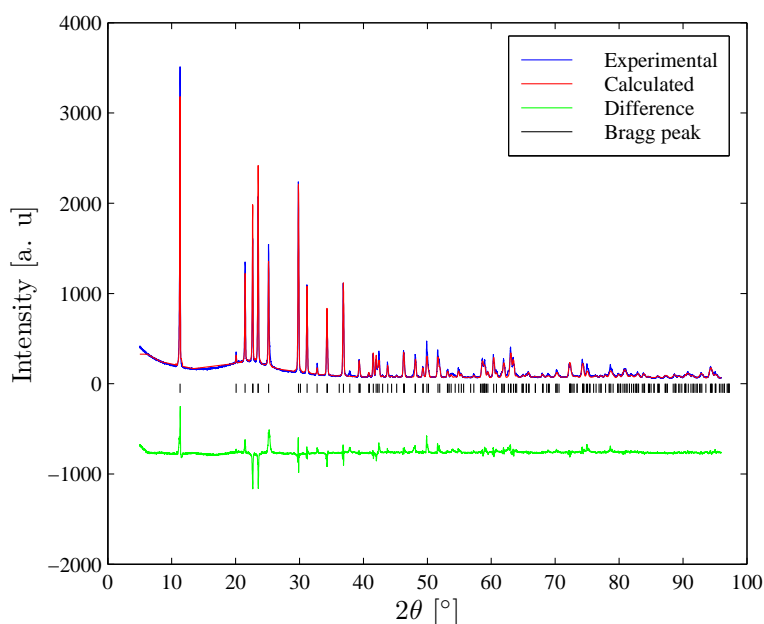
Figure A.1: The powder X-ray spectrum of $KTi(SO_4)_2$. The Rietveld refinement is shown in red.

the solution, forming a green/orange suspension. Over the course of several hours, the pH was adjusted to 5.4 by addition of approximately y ml of a 1 M solution of NaOD.

The suspension was refluxed for 3 days at 90°C, until all the V_2O_5 was consumed, leaving a light green/yellow precipitate. In order to avoid H/D exchange, the product was filtered in a nitrogen filled wet-box. Even with all precautions taken to avoid contact with air, the deuteration level of the product at this stage was found to be only $80 - 90\%$. To improve this, the powder was loaded into a teflon lined steel bomb along with D_2O, filling up approximately 80% of the volume of the container. The mixture was heated at 90°C for 24 hours, at which point the D_2O was decanted off and replaced by fresh solution. This cycle was repeated 4 times for each sample, with an estimated replacement of around 50% of the remaining H at each iteration. The final product was filtered again, and dried under vacuum at $95°C$. By repeating this process several times, a total mass of 45g of highly deuterated ($\sim 98\%$ as estimated from spin incoherent cross section in polarised neutron scattering) volborthite was produced. Its purity was checked with X-ray diffraction and SQUID magnetometry, before proceeding to neutron experiments.

Bibliography

Albuquerque, A., F. Alet, P. Corboz, P. Dayal, A. Feiguin, S. Fuchs, L. Gamper, E. Gull, S. Grtler, A. Honecker, R. Igarashi, M. Krner, *et al.*, 2007, Journal of Magnetism and Magnetic Materials **310**(2, Part 2), 1187 .

Anderson, P. W., 1959, Phys. Rev. **115**(1), 2.

Anderson, P. W., 1973, Mat. Res. Bull. **8**(2), 153.

Anderson, P. W., 2002, Physica Scripta **T102**, 10.

Barthel, T., U. Schollwoeck, and S. R. White, 2009, Phys. Rev. B **79**(24), 245101.

Bert, F., D. Bono, P. Mendels, F. Ladieu, F. Duc, J. C. Trombe, and P. Millet, 2005, Phys. Rev. Lett. **95**(8), 087203.

Bert, F., D. Bono, P. Mendels, J. C. Trombe, P. Millet, A. Amato, C. Baines, and A. Hillier, 2004, J. Phys.: Condens. Matter **16**(11, Sp. Iss. SI), S829.

Bert, F., S. Nakamae, F. Ladieu, D. L'Hote, P. Bonville, F. Duc, J. C. Trombe, and P. Mendels, 2007, Phys. Rev. B **76**(13), 132411.

Bohr, N., 1913, Philos. Mag. **26**, 1.

Braithwaite, R. S. W., K. Mereiter, W. H. Paar, and A. M. Clark, 2004, Miner. Mag. **68**(3), 527.

Bramwell, S. T., S. G. Carling, C. J. Harding, K. D. M. Harris, B. M. Kariuki, L. Nixon, and I. P. Parkin, 1996, J. Phys.: Condens. Matter **8**, L123.

Buhler, A., N. Elstner, and G. S. Uhrig, 2000, Eur. Phys. J. B **16**(3), 475.

Buhler, A., U. Low, and G. Uhrig, 2001, Phys. Rev. B **64**(2), 024428.

Carlin, R., and L. DeJongh, 1986, Chem. Rev. **86**(4), 659.

Caux, J.-S., J. Mossel, and I. P. Castillo, 2008, J. Stat. Mech. , P08006.

Cepas, O., C. M. Fong, P. W. Leung, and C. Lhuillier, 2008, Phys. Rev. B **78**(14), 140405.

Chalker, J., and J. Eastmond, 1992, Phys. Rev. B **46**(21), 14201.

Chalker, J. T., 2009, arxiv:0901.3492 .

Chubukov, A. V., and D. I. Golosov, 1991, J. Phys.: Condens. Matter **3**(1), 69.

des Cloizeaux, J., and J. J. Pearson, 1962, Phys. Rev **128**(5), 2131.

Coldea, R., D. A. Tennant, R. A. Cowley, D. F. McMorrow, B. Dorner, and Z. Tyl-
czynski, 1997, Phys. Rev. Lett. **79**(1), 151.

Coldea, R., D. A. Tennant, and Z. Tylczynski, 2003, Phys. Rev. B **68**(13), 134424.

Coomer, F. C., A. Harrison, G. S. Oakley, J. Kulda, J. R. Stewart, J. A. Stride, B. Fak,
J. W. Taylor, and D. Visser, 2006, J. Phys.: Condens. Matter **18**(39), 8847.

Corey, E. J., and X.-M. Cheng, 1995, *The Logic of Chemical Synthesis* (Wiley).

Dionne, G. F., and J. A. MacKinno, 1968, Phys. Rev. **172**(2), 325.

Dommange, S., M. Mambrini, B. Normand, and F. Mila, 2003, Phys. Rev. B **68**(22),
224416.

Einstein, A., B. Podolsky, and N. Rosen, 1935, Phys. Rev. **47**(10), 0777.

Elhajal, M., B. Canals, and C. Lacroix, 2002, Physica B **312**, 716.

Enderle, M., C. Mukherjee, B. Fak, R. K. Kremer, J. M. Broto, H. Rosner, S. L.
Drechsler, J. Richter, J. Malek, A. Prokofiev, W. Assmus, S. Pujol, *et al.*, 2005,
Europhys. Lett. **70**(2), 237.

Fazekas, P., 1999, *Lecture Notes on Electron Correlation and Magnetism* (World-
Scientific).

Feynman, R., 1960, Eng. Sci. , 22.

Fisher, D. S., 1989, Phys. Rev. B **39**(16, Part A), 11783.

Foulkes, W. M. C., L. Mitas, R. J. Needs, and G. Rajagopal, 2001, Rev. Mod. Phys
73(1), 33.

Furrer, A., J. Mesot, and T. Straessle, 2009, *Neutron Scattering in Condensed Matter
Physics* (World-Scientific).

Furukawa, S., 2010, Private communication.

Gerlach, W., and O. Stern, 1921, Z. Phys. **8**(Sp. Iss. YRS 1921/2), 110.

Graeber, E. J., B. Morosin, and A. Rosenzwe, 1965, Amer. Miner. **50**(11-1), 1929.

Gutzwiller, M. C., 1963, Phys. Rev. Lett. **10**(5), 159.

Hagiwara, M., Y. Narumi, K. Kindo, N. Maeshima, K. Okunishi, T. Sakai, and M. Taka-
hashi, 2001, Physica B **294**, 83.

Haldane, F. D. M., 1982, Phys. Rev. B **25**(7), 4925.

Hao, Z., and O. Tchernyshyov, 2009, Phys. Rev. Lett. **103**(18), 187203.

Harris, A. B., C. Kallin, and A. J. Berlinsky, 1992, Phys. Rev. B **45**(6), 2899.

Hase, M., I. Terasaki, and K. Uchinokura, 1993, Phys. Rev. Lett. **70**(23), 3651.

Helton, J. S., K. Matan, M. P. Shores, E. A. Nytko, B. M. Bartlett, Y. Yoshida,
Y. Takano, A. Suslov, Y. Qiu, J. H. Chung, D. G. Nocera, and Y. S. Lee, 2007, Phys.
Rev. Lett. **98**(10), 107204.

Hermele, M., Y. Ran, P. A. Lee, and X.-G. Wen, 2008, Phys. Rev. B **77**(22), 224413.

Hiroi, Z., M. Hanawa, N. Kobayashi, M. Nohara, H. Takagi, Y. Kato, and M. Takigawa, 2001, J. Phys. Soc. Japan **70**(11), 3377.

Holstein, T., and H. Primakoff, 1940, Phys. Rev. **58**(12), 1098.

Hubbard, J., 1963, Proc. Roy. Soc. London **276**(1364), 238.

Huse, D. A., and V. Elser, 1988, Phys. Rev. Lett. **60**(24), 2531.

Janson, O., J. Richter, P. Sindzingre, and H. Rosner, 2010, arxiv:1004.2185 .

Jerome, D., A. Mazaud, M. Ribault, and K. Bechgaard, 1980, J. Physique Lettres **41**(4), L95.

Jiang, H. C., W. Z. Y., and D. N. Sheng, 2008, Phys. Rev. Lett. **101**, 117203.

de Jongh, L. J., and A. R. Miedema, 2001, Adv. Phys. **50**(8), 947.

Kohno, M., O. A. Starykh, and L. Balents, 2007, Nature Physics **3**(11), 790.

Kokalj, J., and P. Prelovsek, 2009, Phys. Rev. B **80**(20), 205117.

Kubo, R., 1952, Phys. Rev. **87**(4), 568.

Kumar, M., S. Ramasesha, and Z. G. Soos, 2010, Phys. Rev. B **81**(5), 054413.

Lafontaine, M. A., A. Lebail, and G. Ferey, 1990, J. Solid State Chem. **85**(2), 220.

Maeshima, N., M. Hagiwara, Y. Narumi, K. Kindo, T. C. Kobayashi, and K. Okunishi, 2003, J. Phys.: Condens. Matter **15**(21), 3607.

Majumdar, C. K., and D. K. Ghosh, 1969a, J. Math. Phys. **10**(8), 1399.

Majumdar, C. K., and D. K. Ghosh, 1969b, J. Math. Phys. **10**(8), 1388.

Marston, J. B., and C. Zeng, 1991, J. App. Phys. **69**(8, Part 2B), 5962.

Masuda, T., A. Zheludev, B. Roessli, A. Bush, M. Markina, and A. Vasiliev, 2005, Phys. Rev. B **72**(1), 014405.

McCabe, J. H., 1983, Math. Comp. **41**(163), 183.

Mendels, P., F. Bert, M. A. de Vries, A. Olariu, A. Harrison, F. Duc, J. C. Trombe, J. S. Lord, A. Amato, and C. Baines, 2007, Phys. Rev. Lett. **98**(7), 077204.

Messio, L., 2010, *Modèles bidimensionnels de spins* (Université Pierre et Marie Curie).

Mila, F., 2000, Eur. J. Phys. **21**, 499.

Moon, R. M., T. Riste, and W. C. Koehler, 1969, Phys. Rev. **181**(2), 920.

Moriya, T., 1960, Phys. Rev. **120**, 91.

Mott, N. F., 1990, *Metal-Insulator Transitions* (Taylor & Francis).

Moulton, B., and M. Zaworotko, 2001, Chem. Rev. **101**(6), 1629.

Neuberger, H., and T. Ziman, 1989, Phys. Rev. B **39**(4), 2608.

Nilsen, G. J., H. M. Ronnow, A. M. Laeuchli, F. P. A. Fabbiani, J. Sanchez-Benitez, K. V. Kamenev, and A. Harrison, 2008, Chem. Mater. **20**(1), 8.

Okamoto, K., and K. Nomura, 1992, Phys. Lett. A **169**(6), 433.

Olariu, A., P. Mendels, F. Bert, F. Duc, J. C. Trombe, M. A. de Vries, and A. Harrison, 2008, Phys. Rev. Lett. **100**(8), 087202.

Porta, J. B., 1658 edition, *Natural Magick*, volume 7 (Thomas Young and Samual Speed).

Reimers, J. N., and A. J. Berlinsky, 1993, Phys. Rev. B **48**(13), 9539.

Richter, J., A. Honecker, and J. Schulenburg, 2004, *Quantum Magnetism*, volume 645 of *Lecture Notes in Physics* (Springer).

Robert, J., B. Canals, V. Simonet, and R. Ballou, 2008, Phys. Rev. Lett. **101**(11), 117207.

Rokhsar, D. S., and S. A. Kivelson, 1988, Phys. Rev. Lett. **61**, 2376.

Rousochatzakis, I., S. R. Manmana, A. M. Laeuchli, B. Normand, and F. Mila, 2009, Phys. Rev. B **79**(21), 214415.

Sachdev, S., 1992, Phys. Rev. B **45**(21), 12377.

Scharpf, O., and H. Capellman, 1993, Phys. Stat. Solidi A **135**(2), 359.

Schmidt, G. M. J., 1971, Pure Appl. Chem. **27**, 647.

Shores, M., E. Nytko, B. Bartlett, and D. Nocera, 2005, J. Am. Chem. Soc. **127**(39), 13462.

Sindzingre, P., 2007, arxiv:0707.4264 .

Singh, R. R. P., 2010, Phys. Rev. Lett. **104**(17), 177203.

Singh, R. R. P., and D. A. Huse, 2007, Phys. Rev. B **76**(18), 180407.

Somma, R. D., and A. A. Aligia, 2001, Phys. Rev. B **64**(2), 024410.

Squires, G. L., 1978, *Introduction to the Theory of Thermal Neutron Scattering* (Cambridge University Press).

Starykh, O. A., and L. Balents, 2007, Phys. Rev. Lett. **98**(7), 077205.

Stewart, J. R., P. P. Deen, K. H. Andersen, H. Schober, J. F. Barthelemy, J. M. Hillier, A. P. Murani, T. Hayes, and B. Lindenau, 2009, J. Appl. Crystallogr. **42**(Part 1), 69.

Syozi, I., 1951, Prog. Theor. Phys. **6**(3), 306.

Taniguchi, H., M. Miyashita, K. Uchiyama, K. Satoh, N. Mori, H. Okamoto, K. Miyagawa, K. Kanoda, M. Hedo, and Y. Uwatoko, 2003, J. Phys. Soc. Japan **72**(3), 468.

Tóth, T., 2010, *PhD Thesis*, Ph.D. thesis, Ecole Polytechnique Fédérale de Lausanne.

Toulouse, G., 1977, Commun. Phys. **115**, 115.

Villain, J., R. Bidaux, J. P. Carton, and R. Conte, 1980, J. Physique **41**(11), 1263.

de Vries, M. A., K. V. Kamenev, W. A. Kockelmann, J. Sanchez-Benitez, and A. Harrison, 2008, Phys. Rev. Lett. **100**(15), 157205.

Waldtmann, C., H. U. Everts, B. Bernu, C. Lhuillier, P. Sindzingre, P. Lecheminant, and L. Pierre, 1998, Eur. Phys. J. B **2**(4), 501.

Wang, F., A. Vishwanath, and Y. B. Kim, 2007, Phys. Rev. B **76**(9), 094421.

Weiss, P., 1906, Comptes Rendus **143**, 1136.

White, S. R., and I. Affleck, 1996, Phys. Rev. B **54**(14), 9862.

Wills, A. S., 1996, *A Study of Experimental Kagomé Antiferromagnets Based on the Jarosite Series* (University of Edinburgh).

Yavors'kii, T., W. Apel, and H.-U. Everts, 2007, Phys. Rev. B **76**(6), 064430.

Yildirim, T., and A. B. Harris, 2006, Phys. Rev. B **73**(21), 214446.

Yoshida, H., Y. Okamoto, T. Tayama, T. Sakakibara, M. Tokunaga, A. Matsuo, Y. Narumi, K. Kindo, M. Yoshida, M. Takigawa, and Z. Hiroi, 2009a, J. Phys. Soc. Japan **78**(4), 043704.

Yoshida, M., M. Takigawa, H. Yoshida, Y. Okamoto, and Z. Hiroi, 2009b, Phys. Rev. Lett. **103**(7), 077207.

Zeng, C., and V. Elser, 1995, Phys. Rev. B **51**(13), 8318.

Zheng, W. H., and C. J. Hamer, 1993, Phys. Rev. B **47**(13), 7961.

Zorko, A., S. Nellutla, J. van Tol, L. C. Brunel, F. Bert, F. Duc, J. C. Trombe, M. A. de Vries, A. Harrison, and P. Mendels, 2008, Phys. Rev. Lett. **101**(2), 026405.